Optofluidic Dye Lasers

Thesis by

Zhenyu Li

In Partial Fulfillment of the Requirements

for the Degree of

Doctor of Philosophy

California Institute of Technology

Pasadena, California

2007

(Defended July 17, 2007)

To my wife,

Lun

Acknowledgements

First, I would like to express my sincere gratitude to my advisor, Professor Demetri Psaltis, for his support and guidance throughout my graduate studies at Caltech. I'll be forever indebted to him for offering me the opportunity to pursue my PhD degree at the same school as my wife, not to mention it's Caltech. His contagious enthusiasm, keen intuition and objective attitude have been a constant source of inspiration. As one of his last students at Caltech, I wish him all the good luck for his new challenging position at EPFL, and hope always to have the chance to work with him in the future.

I would also like to thank Professor Axel Scherer, Zhaoyu Zhang, Teresa Emery and Yan Chen for the fruitful collaborations that led to much of the work presented here. Over the years, I have learned a lot from my collaborators at various stages of my research, in particular, Prof. Changhuei Yang of Caltech; Prof. George Barbastathis and Dr. Kehan Tian of MIT; Dr. Annmarie Eldering, Dr. Gregory Bearman and William Johnson of JPL; Dr. Harvey Kasdan of Iris Diagnostics; Dr. Wenhai Liu and Dr. Christophe Moser of Ondax.

Thanks are also due to the members of Psaltis group: Jose Mumbru, Yunping Yang, Dr. Zhiwen Liu, George Panotopoulos, Hung-Te Hsieh, Martin Centurion, Hua Long, James Adleman, Mankei Tsang, Baiyang Li, Jae-Woo Choi, George Cadena, Chia-Lung Hsieh, Dr. David Erickson, Dr. Ye Pu, Dr. Allen Pu, and Dr. Mathias Dietzel for their help in the lab and many enlightening conversations on both science and life. I would also like to thank Lucinda and Linda for handling administrative matters. Many thanks to Yayun for helping me in the lab and offering much invaluable advice outside the lab including a marvelous vegetable soup recipe for my daughter, which I haven't but still intend to feed her regularly. Many friends and colleagues have contributed to make my six years at Caltech one of the

most educational and memorable experiences of my life. While by no means an exhaustive list, I would especially like to thank: Xiaoli Feng, Vijay Gupta, Rizal Hariadi, Xin Heng, Cheng Jin, Zhipu Jin, Wei Liang, Xin Liu, Bumki Min, Eric Ostby, Troy Rockwood, Kevin Tang, Jiantao Wang, Lan Yang, Qiang Yang, Hualin Ye, Zhengrong Wang and David Wei.

I also want to thank my parents-in-law, Guobin Li and Guoqing Sun, for taking good care of my daughter so that my wife and I could concentrate on work during our last year at graduate school.

I want to thank my parents and my sister, whose unconditional love, understanding and support have carried me through the unimaginably long educational path. It was their influence that made me decide long ago I would only choose a career I like.

Finally and most importantly, to Lun, my wonderful wife. You have done more for me and this thesis than any other. Meeting you was the luckiest thing that ever happened to me. Without your love and support, none of this would have happened, and none of this would matter. I dedicate this thesis to you.

Abstract

Optofluidic dye lasers refer to a class of liquid dye lasers, usually on a microfabricated device, in which the adaptive nature of the liquid gain medium allows the dynamical control of the laser properties. Miniaturizing liquid dye lasers onto a microfluidic device not only results in compact, easy-to-maintain and safe dye laser systems, but also provides unprecedented optical performances such as precise spatial mode control, low threshold, and automatic fluidic tuning. Equally important, such on-chip liquid laser sources represent an important component for "lab-on-a-chip" systems.

This thesis studies the implementations of optofluidic dye lasers on polydimethylsiloxane (PDMS) based microfluidic devices. Replica molding soft lithography was used to fabricate monolithic PDMS devices which contain both wavelength-scale optical structures and large-sized microfluidic channels. We have demonstrated narrow linewidth single mode DFB lasers, simultaneous operation of integrated DFB laser arrays with a single pump, multiple color lasing from the same DFB cavity, continuous mechanical wavelength tuning over a 60nm range, microfluidic wavelength tuning, single mode liquid-core microring lasers using Vernier effect, liquid-cladding evanescent gain DFB lasers, and monolithic integration with PDMS microfluidic circuits. Typical laser thresholds achieved are well within the reach of commercial high power laser diodes, thus enabling the implementations of compact tunable laser sources for portable "lab-on-a-chip" devices. The impressive performances, diverse geometries and applications clearly demonstrate the power of optofluidic integration and adaptation.

Contents

List of Figures

List of Tables

Chapter 1

Introduction

This thesis presents a new class of liquid dye lasers, which we call optofluidic dye lasers. In these microfabricated laser systems, the liquid dye solution, besides providing the optical gain, plays a crucial role in determining the optical properties of the laser light such as the lasing wavelength, the spatial mode and the tunability. The emergence of optofluidic dye lasers is largely enabled by the recent advances in microfabrication and microfluidics technologies [4][5]. With micromachining and soft lithography techniques, micron-scale fluidic channels can now be routinely made in optically transparent glasses, polymers and silicone elastomer materials. This enables the fabrication of liquid core or liquid cladding integrated optical components onto the same device as the microfluidic circuits. Highly automated on-chip fluidic manipulation and large scale integration also became a reality after the development of silicone elastomer based micro mechanical valves and pumps [5][6][7].

1.1 Motivations for Building On-chip Liquid Dye Lasers

The advantages of miniaturizing liquid dye lasers onto a microfluidic device (Figure 1.1) are threefold. First, microfabricated devices can eliminate many undesirable features of the conventional bulk dye lasers which have hindered their widespread use. As is well known, conventional dye lasers have the reputation of "user unfriendly" due to their bulky and complex liquid-handling systems and hazards of toxic dyes. Microfabrication can dramatically reduce the sizes and complexity of both the optical and liquid-handling systems.

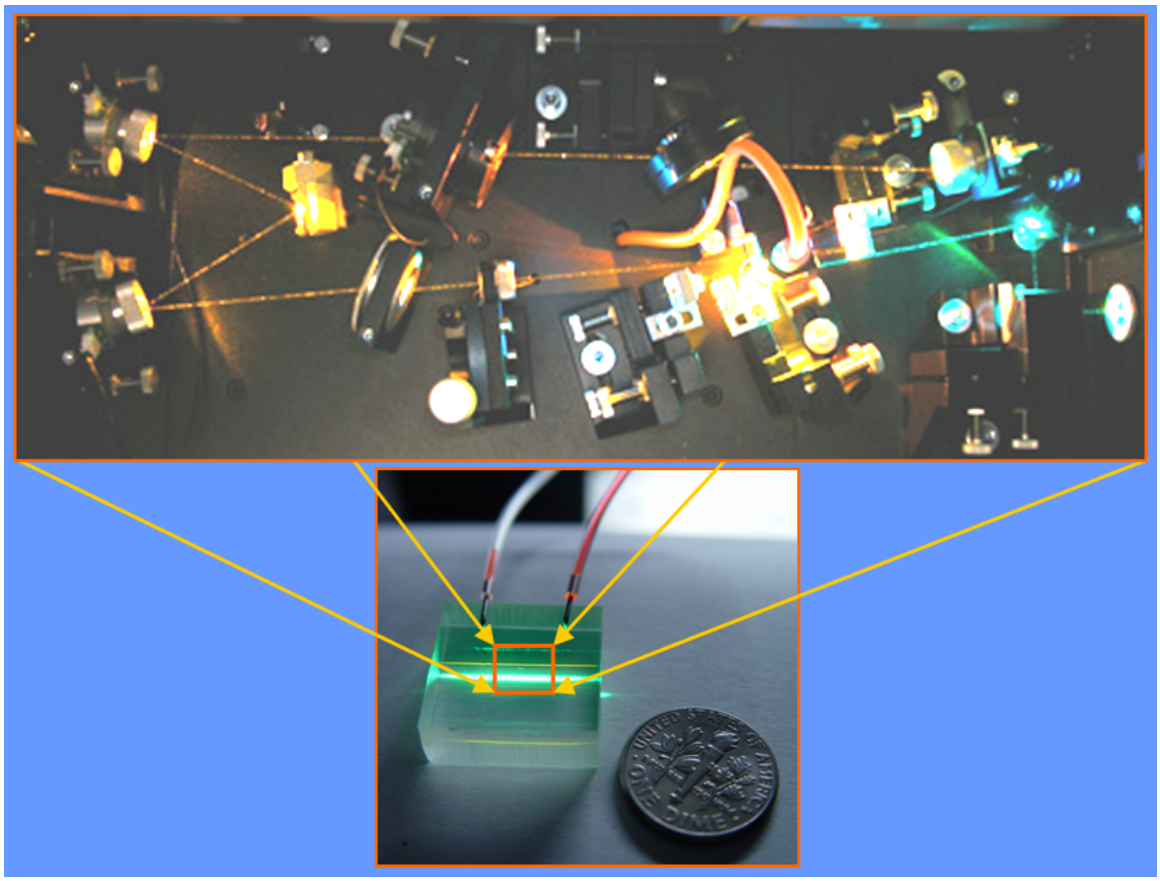

Figure 1.1: Miniaturization of liquid dye lasers on a microfluidic chip.

For example, in the dye lasers discussed in this thesis, the integrated optical components and highly automated microfluidic circuits replaced their bulk counterparts, and resulted in centimeter-sized devices as shown in Figure 1.1. In addition, the extremely small consumption of dye solutions in microfabricated devices not only reduces the cost, but, combined with the sealed structure, significantly improves the safety and ease of use of dye laser systems.

Second, the integration of microfluidics with the adaptive nature of liquid gain medium enables unique optical performances that are not obtainable within solid state materials [8]. This is where the term "optofluidic" comes from. For example, in optofluidic dye lasers, the lasing wavelength can be easily changed by mixing two different solvents to modify the refractive index of the dye solution which is part of the waveguide structure, or by simply switching from one dye molecule to another [9].

Third and probably the most important feature of optofluidic dye lasers is their ability to integrate with other optical and microfluidic functions to build complete ”lab-on-a-chip” systems. This represents an important step towards fully functional and portable devices for medical diagnostics, environmental monitoring, forensic and bioterrorism detection [10].

1.2 Thesis Organization

In this thesis, we investigate the implementations of microfabricated liquid dye lasers on poly(dimethylsiloxane) (PDMS) microfluidic devices. Chapter 2 gives the background knowledge and related work upon which this thesis is based. Three ingredients of optofluidic dye lasers: conventional dye lasers, microfluidics and optofluidics are discussed which form the guidlines for all the following chapters. This chapter also provides a comprehensive review on micron-sized liquid dye lasers before the microfluidics era. It appears they are all amenable to future microfluidic implementations and have potentially interesting applications. Several other groups' work on optofluidic dye lasers is also reviewed in Chapter 2. Chapter 3 describes a liquid-core guided-wave distributed feedback (DFB) laser structure which not only leads to single mode dye laser operation, but also forms the basis for the tunable laser work described in Chapter 4 and 5. Chapter 4 presents our efforts to build an on-chip tunable dye laser by exploiting the elastic properties of PDMS. An impressive 60nm tuning range was achieved by simply stretching the laser chip. Potentially, this tuning range can be further increased to cover the whole visible spectrum. Simultaneous operation of thirteen DFB dye lasers on a single chip was also achieved using only one external pump laser. Chapter 5 provides the detailed method to monolithically integrate DFB dye lasers with a PDMS microfluidic mixing circuit. A theoretical investigation of the optimum cavity structure for microfluidic tuning is also given. Apart from previous chapters, Chapter 6 describes a new laser structure based on liquid-core microring resonators. A coupled-ring resonator structure is shown to allow the realization of single mode microring dye lasers using Vernier effect. Chapter 7 introduces a liquid-cladding laser structure based on evanescent gain. The benefits of the liquid-cladding structure are discussed. Chapter 8 presents a dye doped solid state polymer laser using a surface emitting circular grating DFB res-

onator. This laser is particularly suitable for LED-pumped devices due to the well matched emitting area. Appendix A gives the detailed fabrication recipes used in this thesis.

Chapter 2

Background and Related Work

Three ingredients are indispensable for the development of optofluidic dye lasers: conventional liquid dye lasers, microfluidics, and optofluidic integration and adaptation. Therefore, in this chapter, we provide the background knowledge on these three topics that are important for the discussions in later chapters. Section 2.1.1 briefly reviews the general properties of liquid dye lasers including the photophysical properties of organic dye molecules, a rate equation model for dye lasers and a simple pump threshold analysis. Section 2.1.2 discusses the state of the art microfluidics and "lab-on-a-chip" technologies. Particular attention is paid to the lack of optical functions in most demonstrated "lab-on-a-chip" systems. Section 2.1.3 introduces the general idea of optofluidics and its potential impact on both adaptive optics and "lab-on-a-chip" systems. We also present the previous work related to this thesis in Section 2.2, which includes both pre-microfluidics era microscopic liquid dye lasers (Section 2.2.1) and on-chip microfluidic dye lasers demonstrated by other groups (Section 2.2.2).

2.1 Ingredients of Optofluidic Dye Lasers

2.1.1 Liquid Dye Lasers

Liquid dye lasers use a solution of organic dye molecules in a solvent, such as an alcohol or water, as the optical gain medium. The ultra-wide wavelength tuning range and the ability to generate both narrow linewidth CW output and ultra-short (<100fs) pulses

make dye lasers an ideal coherent light source for spectroscopy [11]. The unique features of dye lasers are directly linked to the molecular structures and the photophysical properties of organic dye molecules. Therefore, we will start with the discussion of the properties of laser dyes. Based on these properties, we will build a rate equation model for dye lasers and use it to study the threshold for the laser action. No attempt is made to give a comprehensive review on conventional dye lasers since a number of excellent articles ([12], [13], [14], [15], [16], [17]) and books ([11], [18]) are already available. Another very useful resource is a collection of original papers on dye lasers which has been published in the SPIE Milestone Series [19]. Textbooks on semiconductor lasers [20] and integrated optics [21][22] are also good references for the study of optofluidic dye lasers due to their similar sizes, structures and gain properties.

2.1.1.1 Photophysical Properties of Organic Dye Molecules

Laser dyes are complex organic molecules containing long chains of conjugated double bonds (i.e. alternating single and double carbon bonds, =C-C=C-). The large molecular size and the relatively free moving π-electrons in the conjugated double bonds give rise to the large dipole moments of dye molecules (or equivalently, oscillator strengths). The complex molecular structure also leads to many vibrational and rotational levels within a single electronic state. Therefore, laser dyes often have strong and wide absorption bands in the UV and visible region as shown in Figure 2.1 [23]. The emission spectra of dye molecules are Stokes-shifted to longer wavelength and form almost mirror images of the absorption bands due to the so-called Frank-Condon principle [24]. This is a rather fortunate feature because the laser emission will generally not be strongly absorbed by the dye itself. In the following, we will briefly discuss the energy levels and the transition processes involved in the laser operation, with a special focus on the effects of the dark triplet states. For more complete discussions of the photophysical and photochemical properties of laser dyes including the environmental effects, the readers are referred to the reference [11].

Figure 2.2 shows the typical energy levels of a dye molecule. S_0 and S_1 are the ground and the first excited singlet electronic states. T_1 and T_2 are the first and second excited triplet states. In a singlet state, the spin of the excited electron is anti-parallel to the spin

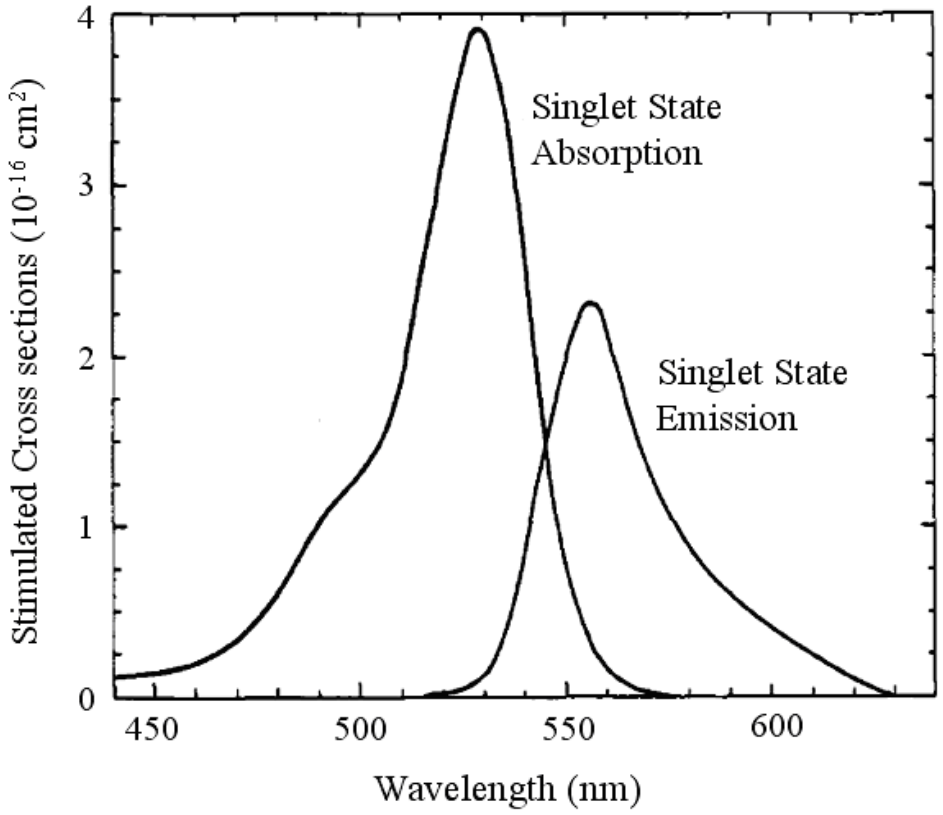

Figure 2.1: Stimulated singlet state absorption and emission cross sections for Rhodamine 6G in ethanol.

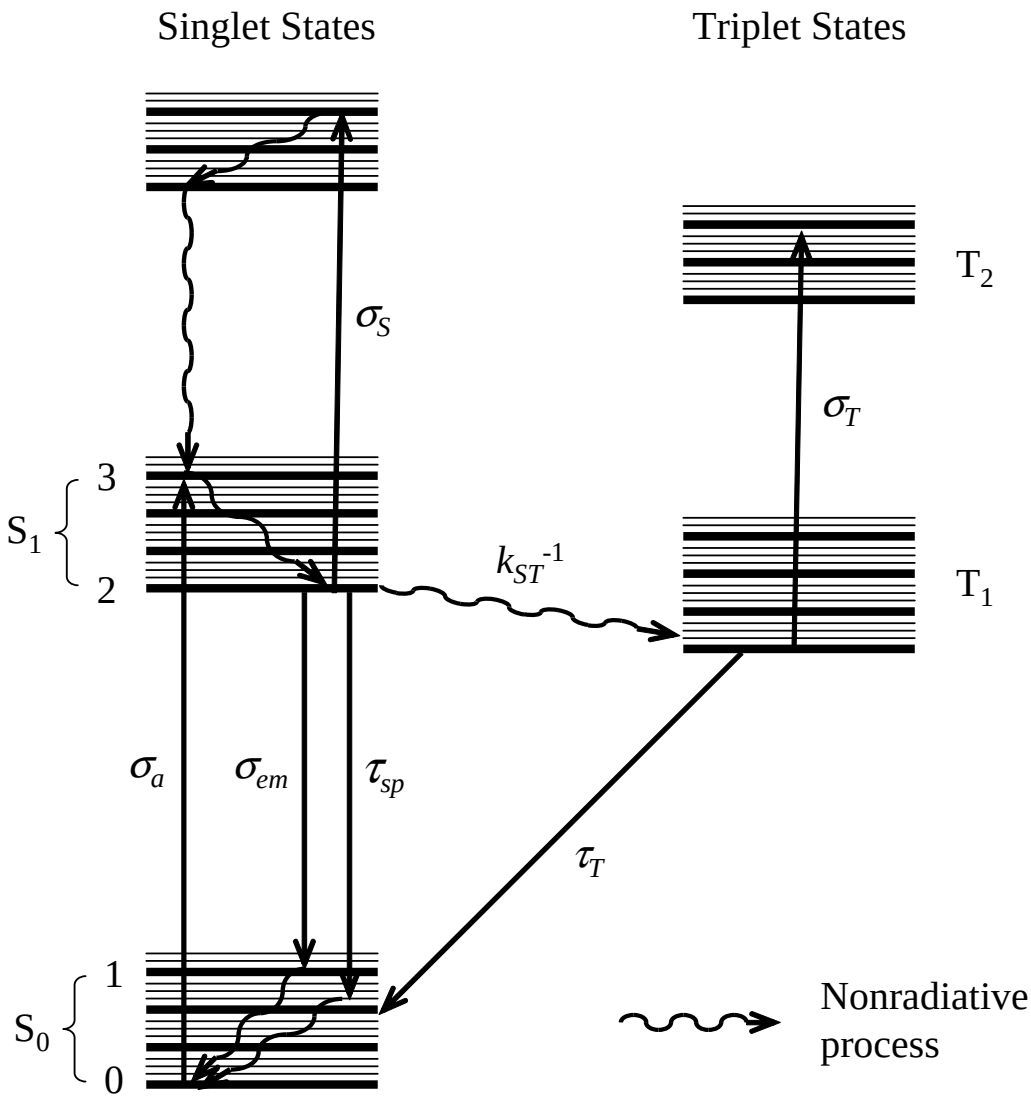

Figure 2.2: Typical energy levels of an organic dye molecule. Each transition is labeled by its corresponding cross section or lifetime.

of the remaining molecule and the total spin quantum number is S = 0, whereas in a triplet state the two spins are parallel and S = 1. Therefore singlet-singlet and triplet-triplet transitions are allowed, while singlet-triplet transitions are forbidden because of the selection rule $\Delta S = 0$. As mentioned before, each electronic state is further split into many vibrational and rotational sublevels due to the complex dye molecular structure. In addition, the effective homogenous line-broadening mechanism due to the collisions with solvent molecules further smears these sublevels into unresolved overlapping bands. The homogenous broadened spectra of dye molecules enable very efficient channeling of the pump energy into narrow band laser emissions [17].

It is important to realize that the dye laser is a classical 4-level system (if neglecting the triplet states for the moment) where the 4 energy levels are marked 0 to 3 in Figure 2.2. Under optical excitation, dye molecules are pumped from the bottom of the ground state S_0 (ground level 0) to some vibrational-rotational sublevels in the first singlet state S_1 (intermediate pump level 3). The dye molecules in level 3 quickly relax to the bottom of S_1 (upper laser level 2). This nonradiative decay process happens on the time scale of a few picoseconds or less. The energy lost in this process contributes to the heating of the solvent. From the upper laser level 2, dye molecules can undergo either *spontaneous emission* or *stimulated emission* to some vibrational-rotational sublevels in S_0 (lower laser level 1). The nonradiative decay time from the lower laser level 1 to the ground level 0 is also a few picoseconds. There are also some absorptions from the first excited singlet state S_1 to higher singlet states, but this effect is normally small and the nonradiative relaxation time from higher singlet states back to S_1 is also on the order of picosecond. Due to the extremely fast nonradiative decay processes, the populations of the lower laser level n_1 and the intermediate pump level n_3 are negligibly small. Therefore, dye lasers can reach threshold at very small population inversions, with typical upper laser level population n_2/n of only 0.01 or less [17], where n is the total dye population. However, because of the short upper-state lifetimes (a few nanoseconds, mainly due to spontaneous emission), dye lasers still need high pump intensities to reach threshold (see equation (2.7) in section 2.1.1.2).

The real situations are further complicated by the triplet state effects. The excited molecules at the upper laser level 2 undergo not only radiative transitions to S_0 but also

nonradiative *intersystem crossing* to the dark triplet state T_1. As mentioned before, this process requires a spin flip of the excited electron and thus is spin-forbidden. This is the reason that intersystem cross has a relative slow transition rate ($1/k_{ST} \sim 100$ns) and the triplet state lifetime is long ($\tau_T \sim 100$ns). The metastable triplet state has two detrimental effects on laser oscillation. First, the long lived triplet state T_1 traps the dye molecules and decreases the available population inversion. Second, the absorption from the first triplet state T_1 to the second triplet state T_2 tends to overlap with the laser emission and produces extra losses at the laser wavelength. Therefore, short pump pulses, fast circulation of dye solutions and triplet state quenchers are often used to minimize the triplet state influences in different types of dye lasers.

2.1.1.2 Rate Equations

Rate equations describe the time evolution of the energy level populations and the laser cavity mode. Although they don't account for the coherent properties of the laser light, they are very useful for the estimations of the laser threshold and output power.

For dye lasers, three rate equations are needed for describing the laser cavity mode photon flux $\phi(= I_L/h\nu_L)$, the singlet state population density n_2 and the triplet state population density n_T.

Laser cavity mode ϕ:

$$\frac{d\phi}{dt} = c[n_2\sigma_{em}(\lambda_L) - n_0\sigma_a(\lambda_L) - n_1\sigma_T(\lambda_L) - \frac{\gamma}{L}]\phi \tag{2.1}$$

where σ_i's are the stimulated transition cross sections at the laser wavelength λ_L, n_0 is the ground state population density, γ is the single pass cavity loss (equals $-ln(R_1R_2)/2 + \gamma_i$ for Fabry-Perot cavities with internal loss γ_i), L is the length of the gain region and c is the speed of light.

First excited singlet state n_2:

$$\frac{dn_2}{dt} = R_P + [n_0\sigma_a(\lambda_L) - n_2\sigma_{em}(\lambda_L)]\phi - n_1\sigma_T(\lambda_L) - n_2k_{ST} - \frac{n_2}{\tau_{sp}}] \tag{2.2}$$

where k_{ST} is the intersystem crossing rate, τ_{sp} is the spontaneous emission lifetime, and the pump rate per unit volume R_P is given by

$$R_P = \frac{n_0 \sigma_a(\lambda_P) I_P}{h\nu_P} \tag{2.3}$$

where I_P is the pump intensity, λ_P and ν_P are the pump light wavelength and frequency respectively, and h is Planck's constant.

First excited triplet state n_T:

$$\frac{dn_T}{dt} = n_2 k_{ST} - \frac{n_T}{\tau_T} \tag{2.4}$$

where τ_T is the triplet state lifetime.

Finally, the conservation of molecules requires

$$n = n_0 + n_2 + n_T \tag{2.5}$$

where n is the total concentration of dye molecules. The typical values of the photophysical parameters needed in the rate equations are listed in Table 2.1 for the most common laser dye, Rhodamine 6G [18].

Table 2.1: Typical values of the photophysical parameters for Rhodamine 6G (pump wavelength λ_P = 532nm, laser wavelength λ_L = 580nm)

Parameter	Value
Absorption cross section at the pump wavelength $\sigma_a(\lambda_P)(cm^2)$	3.8×10^{-16}
Absorption cross section at the laser wavelength $\sigma_a(\lambda_L)(cm^2)$	1×10^{-19}
Stimulated emission cross section at the laser wavelength $\sigma_{em}(\lambda_L)(cm^2)$	1.2×10^{-16}
Triplet state absorption cross section at the laser wavelength $\sigma_T(\lambda_L)(cm^2)$	1×10^{-17}
Spontaneous emission lifetime τ_{sp} (ns)	5
Intersystem crossing time $1/k_{ST}$) (ns)	100
Intersystem crossing time $1/k_{ST}$ (ns)	100†

† Vary from 10^{-7} to 10^{-3} seconds depending on the solvent and the presence or absence of the triplet quencher.

2.1.1.3 Laser Threshold

Our analysis of the pump threshold is similar to those given in [24] and [25]. A more thorough treatment can be found in [23]. In general, the laser threshold can be obtained by numerically solving the rate equations. However, as shown in the following, under certain approximations, analytic expressions can be derived to give reasonable estimates.

Pulsed Operation

In pulsed operation with pump pulse duration shorter than the intersystem crossing time $1/k_{ST}$, we can neglect the triplet state effects all together. This is because with very short pump pulses, the whole cycle of excitation and laser emission within the set of singlet states can be completed before a significant triplet state population buildup occurs. Also we assume the self absorption at the laser wavelength is small. In this case, the threshold population inversion density is determined only by the cavity loss [24]

$$n_{2th} = \frac{\gamma}{\sigma_{em}(\lambda_L)L} \tag{2.6}$$

Therefore, the threshold pump intensity needed to achieve this upper state population is

$$I_{2th} = n_{2th} h\nu_P d/\tau_{sp} = \frac{\gamma h\nu_P d}{\sigma_{em}(\lambda_L)\tau_{sp}L} \tag{2.7}$$

where d is the penetration depth of the pump light into the dye solution, given by $1/n_0\sigma_a(\lambda_P)$. For simplicity we don't consider the spatial dependence of the pump rate and the specific pumping geometry. The readers can find the more accurate treatments in most laser textbooks [24][26].

Continuous Wave (CW) Operation

In CW operation, the triplet state population n_T at equilibrium (steady state) can be obtained from equation (2.4),

$$n_T = n_2 k_{ST} \tau_T \tag{2.8}$$

The threshold gain equals the total loss and, from equation (2.1), is given by

$$g_{th} = n_2\sigma_{em} = n_0\sigma_a + n_T\sigma_T + \gamma/L \tag{2.9}$$

where all the cross sections are evaluated at the laser wavelength. With the help of the population conservation relation (2.5), we get the threshold population inversion

$$n_{2th} = \frac{n\sigma_a + \gamma/L}{\sigma_{em} + \sigma_a(1 + k_{ST}\tau_T) - \sigma_T k_{ST}\tau_T} \tag{2.10}$$

In all practical CW dye lasers, the excited dye molecules are quickly removed from the excitation region and a triplet state quencher is often added to the solution. These two methods effectively reduce the triplet state lifetime by several orders of magnitude. Again for many efficient laser dyes, the self absorption is negligibly small. Consequently, we can set $k_{ST}\tau_T \sim 0$ and $\sigma_a \sim 0$ in equation (2.10), which reduces it to the same expression as equation (2.6). Therefore, we can use expression (2.7) to roughly estimate the pump threshold for both pulsed and CW dye lasers. For typical values $\sigma_{em} = 1 \times 10^{-16} cm^2, \tau_{sp} = 5ns, d = 1mm, L = 10mm, \gamma = 0.01, \nu_P = 5.6 \times 10^{14}$Hz (530nm), the calculated threshold pump intensity is approximately $740W/cm^2$, the corresponding population inversion n_2 is about $1 \times 10^{16} cm^{-3}$ and the threshold gain coefficient is about $1cm^{-1}$. In practical systems, the threshold intensity is usually much higher, about $50kW/cm^2$, due to the triplet state effects, self absorption, thermal distortions and higher cavity losses.

2.1.2 Microfluidics and Lab-on-a-chip Systems

The rapid development of microfluidics in the past 15 years has created a powerful toolbox for manipulating liquids at the nanoliter scale or below [27]. Arguably, the most important goal for microfluidics is to achieve complete "lab-on-a-chip" systems, in which optical functions are often indispensable [28][29]. For example, let's take a look at an important instrument for biology: the fluorescence based Sanger DNA sequencer. This machine enabled the biologists of the Human Genome Project to complete the first draft of the genome sequence of our own species in 2003. The fact we can now read our own

(a)

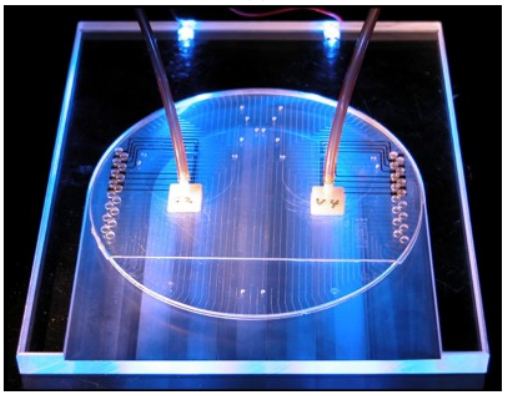

(b)

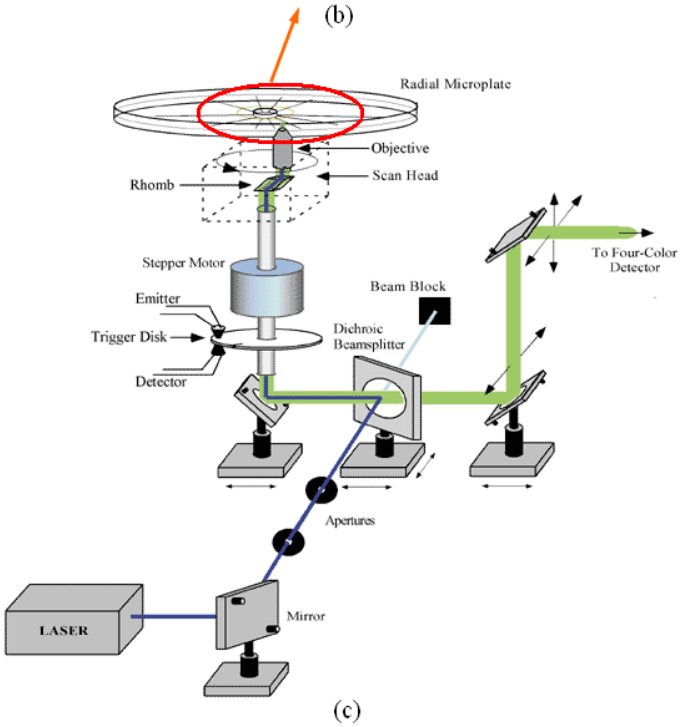

(c)

Figure 2.3: Conventional fluoresence based Sanger DNA sequencer and the "lab-on-a-chip" version. (a) Applied Biosystems 3760xl DNA Analyzer. (b) A microfabricated bio-processor integrating all three Sanger sequencing steps. (c) The bulk optical setup for fluorescence excitation and detection used together with the microfabricated device shown in (b).

instruction books has profound impacts on biology and medicine [30][31]. However the real power of DNA sequencing comes from comparative genomics and personalized genomics by comparing genomes across species and individual genome sequences, which requires much faster and cheaper sequencing techniques than the current ones. Imagine if we can sequence and compare 100 individual genomes at a low cost and in a short period, we will have much better chances of finding out the molecular origins of many diseases such as cancers, Alzheimer's disease and autism. Today's DNA sequencers (for example, the ABI 3730xl DNA Analyzer, Figure 2.3-(a)) cost half a million dollars each and are way too slow for this purpose. One way to achieve low cost and high throughput is through miniaturization. Over the past few years, Richard Mathies' group at UC Berkeley has made remarkable progress along this direction. In one of their recent demonstrations as shown in Figure 2.3-(b), a nanoliter-scale bioprocessor integrating all three Sanger sequencing steps: thermal cycling, sample purificaiton and capillary electropherisis, was fabricated on a glass/PDMS hybrid device [32]. The same group has also demonstrated high throughput operation with a 96-line array electrophoresis device on a single glass substrate [33]. However, the nice looking microfabricated devices are not the whole picture. The complete setup, as shown in Figure 2.3-(c), still occupies a table and includes a visible laser source, relay optics and filters, four photomultiplier tubes, data acquisition electronics and a computer. In fact, this represents a major problem for almost all the demonstrated "lab-on-a-chip" systems so far. Much effort is still needed to achieve the seamless integration of optical and electronic functions with microfluidics on the same device. "Lab-on-a-chip" systems must become compact stand-alone and easy-to-use devices before nonexperts such as biologists, chemists, clinicians and police officers can use them.

2.1.3 Optofluidic Integration and Adaptation

Recently, the power of microfluidic manipulation has been also recognized for building adaptive optical systems [8]. Liquids have many unique features that cannot be found in solid materials such as the ability to change optical properties by mixing or switching between different liquids, the ability to introduce other optical materials such as fluorescent

dyes, quantum dots and dielectric/metallic nanoparticles, and the ease of forming optically smooth interfaces by surface tension. Combining microfluidics and liquid optical materials, optofluidics offers a new way of implementing integrated optical systems, which is intrinsically adaptive and reconfigurable. One important example of such systems is the optofluidic dye lasers, in which the adaptive nature of the liquid gain medium and the combination with microfluidic liquid handing can enable unprecedented optical performances and high degree of system integration. Comprehensive discussions of the recent emergence of optofluidics and classifications of optofluidic devices can be found in [8] and [34].

2.2 Related Work

2.2.1 Pre-Microfludics Era Microscopic Liquid Dye Lasers

The small dimensions of the optofluidic dye lasers are generally achieved using microfabrication techniques. However, there existed micron-sized liquid dye lasers long before the advent of microfluidics which also satisfy our definition of optofluidic dye lasers, such as microdroplet dye lasers [35], microcapillary dye lasers [36], and evanescent gain microsphere [2] and fiber lasers [37] immersed in dye solutions. These pre-microfluidics era micron-scale dye lasers are also amenable to microfluidic implementations and have potentially interesting applications.

The reason that liquid dye lasers can be made with micron-scale dimensions long before microfluidics is that, unlike solid state lasers for which microfabrication or special processing techniques are needed to define the miniaturized optical structures, the flexibility of liquid gain medium allows the formation of micron-scale optical cavities in several straightforward ways without using any microfabrication, such as microdroplet formation, microcapillary filling and immersion of small solid transparent optical structures in dye solutions. Here we divide the pre-microfluidics era optofluidic dye lasers into two categories: *microcavity dye lasers* and *waveguide dye lasers*, in which the microcavity dye lasers are further divided into three subcategories based on the cavity type: *microdroplets*, *evanescent gain* microcavities and *Fabry-Perot* type microcavities. We give representative examples in

each category and discuss their possible implementations using microfluidics technology.

2.2.1.1 Microcavity Dye Lasers

Optical microcavities are resonant structures that confine light in small volumes. A major application of microcavities is to build compact and efficient laser sources. Liquid dye solutions are among the first material systems used to study the laser action and other optical processes in microcavities [38][39]. First, we will discuss dye laser actions in surface tension induced microdroplet cavities.

Microdroplet Dye Lasers Microdroplets, with their near atomically smooth surfaces and small sizes, offer an ideal optical cavity for making low threshold and compact dye lasers. In such microspherical cavities, light is confined by continuous total internal reflections at the liquid-air interface, and forms the so called whispering gallery modes (WGMs). Dye lasing has been demonstrated in free falling droplets [35][1], pendant droplets [40] and levitated droplets [41][42]. Although the observation of dye lasing in droplets dates back to the 1970s [40], the first reported microdroplet dye laser in the literature was by Chang's group [35]. In this work, dye solution droplets were generated by a vibrating orifice, in which a cylindrical liquid jet passing through the orifice is induced to break up into equal-sized droplets by a mechanical vibration of the orifice with the proper frequency and amplitude [35][43]. The main experimental results for 60μm diameter ethanol droplets containing Rhodamine 6G are shown in Figure 2.4. The droplets were pumped by 10ns laser pulses at 532nm. Lasing occurs only in the longer wavelength side of the emission spectrum due to the high self absorption at shorter wavelengths (Figure 2.4, right panel). The laser emission is confined near the surfaces of the droplets which is characteristic for WGMs (Figure 2.4 b). Pump threshold of ~35W/cm^2, which was three orders of magnitude lower than those of bulk dye lasers, was achieved [35]. The cavity Q factor of such droplets can be as high as 10^8 for low dye concentrations ($< 10^{-5}\mu$M) [44]. The characteristics of such droplet dye lasers were comprehensively studied and reviewed [45][46][47][38].

Besides the laser applications, microdroplets have also been used to study cavity induced spontaneous emission modification [48][49][50], single molecule fluorescence[51]

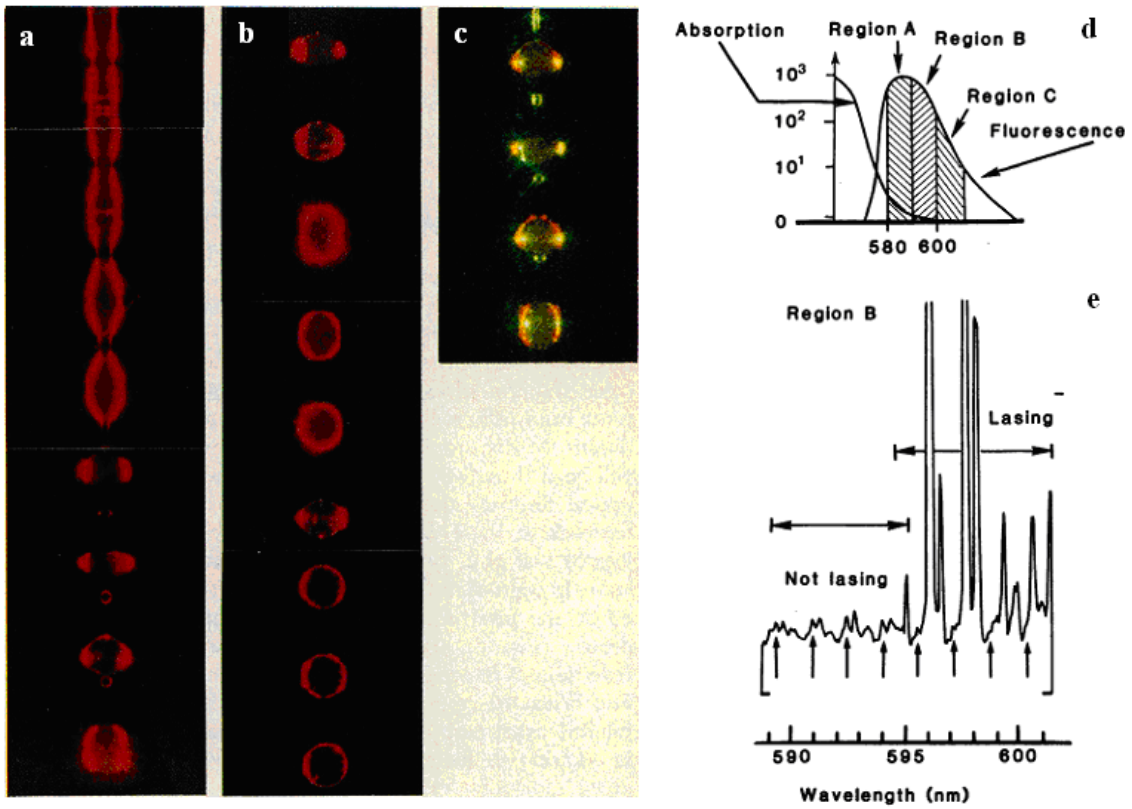

Figure 2.4: Microdroplet dye laser. (Left) Photographs of laser emission from the droplet stream. a. The upper portion of the stream (close to the orifice) showing the breaking of the dye solution and the development of highly distorted droplets. b. The lower portion of the stream showing the transition from oscillating spheroids to monodisperesed spherical droplets. c. A photograph of combined laser emission(red) and elastic scattering(green). (Right) d. Schematic representation of the absorption and emission spectra of Rhodamine 6G in ethanol. e. The emission spectrum of the 60μm diameter droplets for region B. Reprinted from [1].

[52] [53], and many nonlinear optical effects such as stimulated Raman scattering, multi-order Stokes emission and stimulated Brillouin scattering ([38], chapters 5, 6, 7, and references therein).

Although microdroplet cavities hold great potentials for laser applications, biochemical sensing, single molecule studies, nonlinear optics and cavity quantum electrodynamics (cQED), the complexity and inconvenience of the setup, and the short evaporative lifetimes of the droplets have limited them mainly in a few research laboratories. Interestingly, several recently demonstrated on-chip microdroplet generators may change the situation [54][55]. With such devices, mono-dispersed droplets over a wide range of sizes (1-500μm) can be automatically generated in a microfluidic channel at very high speed. Furthermore, the sizes and shapes of individual droplets and the distances between droplets can be accurately controlled by changing the liquid flow rate and the dimensions of the microfluidic channels. This will enable more systematic ways to study new phenomena such as the chaotic behaviors and the directional emissions in nonspherical droplets [56][57] and the coupling effects among many droplet cavities which are difficult, if not impossible, to study with conventional bulk droplet generators. Also, as mentioned above, this can provide an on-chip platform for biochemical sensing, single molecule studies, liquid based nonlinear optics and quantum optics. Finally, the ultrahigh Q's and the small mode volumes make these cavities promising candidates for LED pumped on-chip laser sources [58][59].

Evanescent Gain Microcavity Dye Lasers When the evanescent tail of an optical wave is immersed in a gain medium, it can extract energy and lead to optical amplification. Several groups have demonstrated microcavity liquid dye lasers based on such evanescent wave coupled gain, typically by immersing a WGM resonator such as a microsphere or a microcylinder into a dye solution. Fujiwara and Sasaki demonstrated laser action using silica microspheres dispersed in an aqueous solution of Rhodamine B [60]. They used the fundamental pulses of a Q-switched Nd:YAG laser at 1064nm to optically trap a single microsphere, and the second harmonic pulses at 532nm to pump the surrounding dye molecules. The combination of optical trapping and laser spectroscopy allowed the authors to freely manipulate individual lasing microspheres in three dimensions and measure

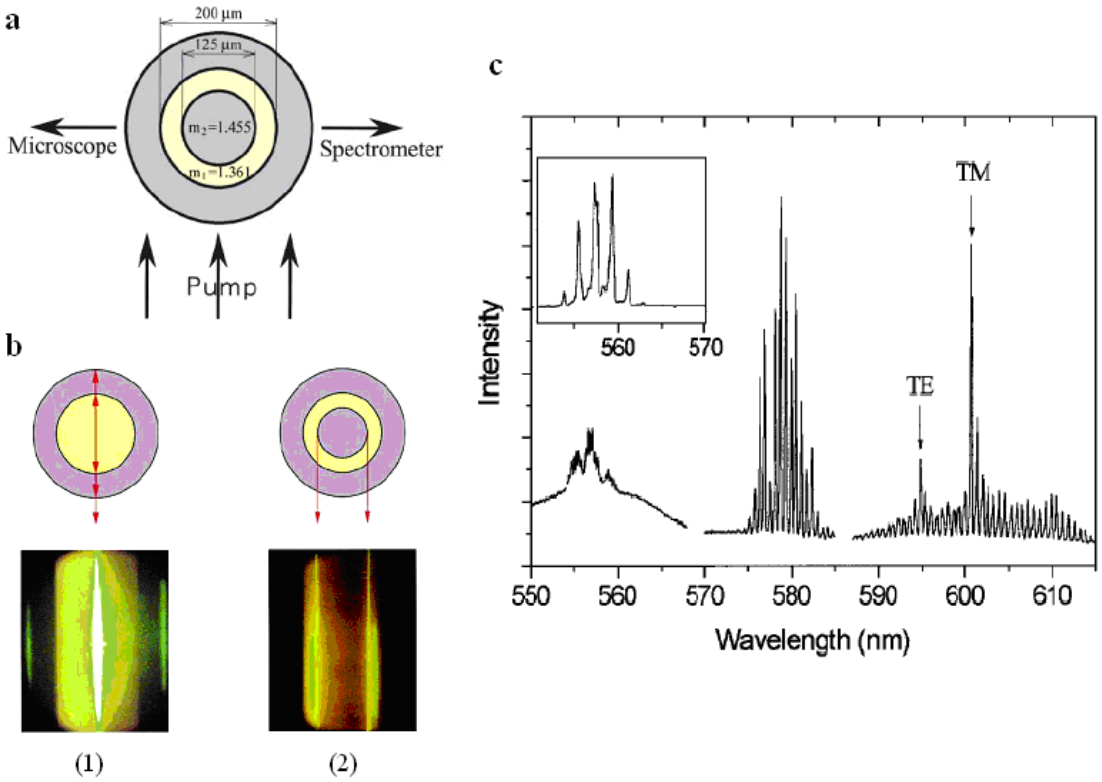

Figure 2.5: a. Cylindrical evanescent gain microcavity dye laser. b. Schematics and microscope images of (1) radial mode lasing and (2) WGM lasing. c. Typical spectra of WGM lasing with the central optical fiber inserted. Inset: typical single shot spectra from the radial mode lasing without the central fiber. Reprinted from [2].

the lasing spectra. The lasing threshold was determined to be 7mW (30ns pulses, 10kHz repetition rate) for a 28μm diameter microsphere in a 10mM Rhodamine B solution. The measured spectra agreed well with the Mie scattering theory prediction. Figure 2.5 shows another evanescent gain dye laser with an ultrahigh Q cylindrical microcavity, which is formed by a fused silica optical fiber located in a capillary tube filled with a low index 2mM Rhodamine 6G solution [2]. Without the center cylindrical cavity, the system showed conventional Fabry-Perot type lasing due to the front and back interfaces (Figure 2.5, b-(1)). However, when an optical fiber (the cylindrical microcavity) of 125μm diameter was inserted into the same capillary, WGM laser oscillation was achieved with a low-threshold pump energy of ~200μJ (Figure 2.5, b-(2), c). The Q factors of these microcavities was inferred from a four-level laser model to be 3×10^7 for the TM modes of radial order $l = 2$.

Even higher Q of 10^9 was achieved when a silica microsphere was used and the dye concentration was lowered to 0.05mM [61][62]. Later, this structure was used to demonstrate laser oscillation with colloidal semiconductor CdSe/ZnS quantum rods as the gain medium [63]. Microring waveguide mode dye lasers were also demonstrated using the structure shown in Figure 2.5 b-(1), in which the high index capillary wall forms the microring cavity [64].

All these demonstrated evanescent gain microcavity dye lasers are based on isolated optical components such as chemically synthesized microspheres, melting induced silica microspheres, optical fibers or capillary tubes. However there is no reason that such lasers can not be made on a microfabricated device integrated with microfluidic liquid handling. In fact, the evanescent gain structure is quite favorable for rapid gain medium replenishment and sensing applications [65]. This formed a strong motivation for our work on evanescent gain optofluidic dye lasers discussed in Chapter 7 .

Fabry-Perot Type Microcavity Dye Lasers Another way to build an optical microcavity is to shrink the mirror spacing of a Fabry-Perot resonator. When the mirror spacing is sufficiently small, the free spectral range (FSR) of the cavity becomes larger than the emission bandwidth, and leads to single longitudinal mode operation. The first optical microcavity experiments used dye molecules between high reflectivity dielectric Bragg reflectors in the Fabry-Perot configuration [66][67]. The main purpose of such experiments was to study the spontaneous emission modification through the Purcell effect (Purcell 1946). For example, Figure 2.6 shows the emission behavior of a dielectric mirror based Fabry-Perot microcavity dye laser [68][3]. The cavity length was accurately defined by Ti spacers deposited on one of the mirrors. The space between the mirrors was filled with dye solution by the capillary forces. When the mirror spacing is half the wavelength ($d = \lambda/2$), the fraction of spontaneous emission coupled into the cavity mode (β) becomes large compared to that of a conventional macroscopic laser. This not only increases the spontaneous emission rate but also makes it highly directional. In principle, the traditional laser threshold can disappear when approaches one, leading to the so called thresholdless laser oscillation [69][66][3]. The factor of ~0.2 was achieved in this experiment for the $d = \lambda/2$ cavity. As shown in the output vs. input curves (Figure 2.6 b), the laser threshold became quite fuzzy for the

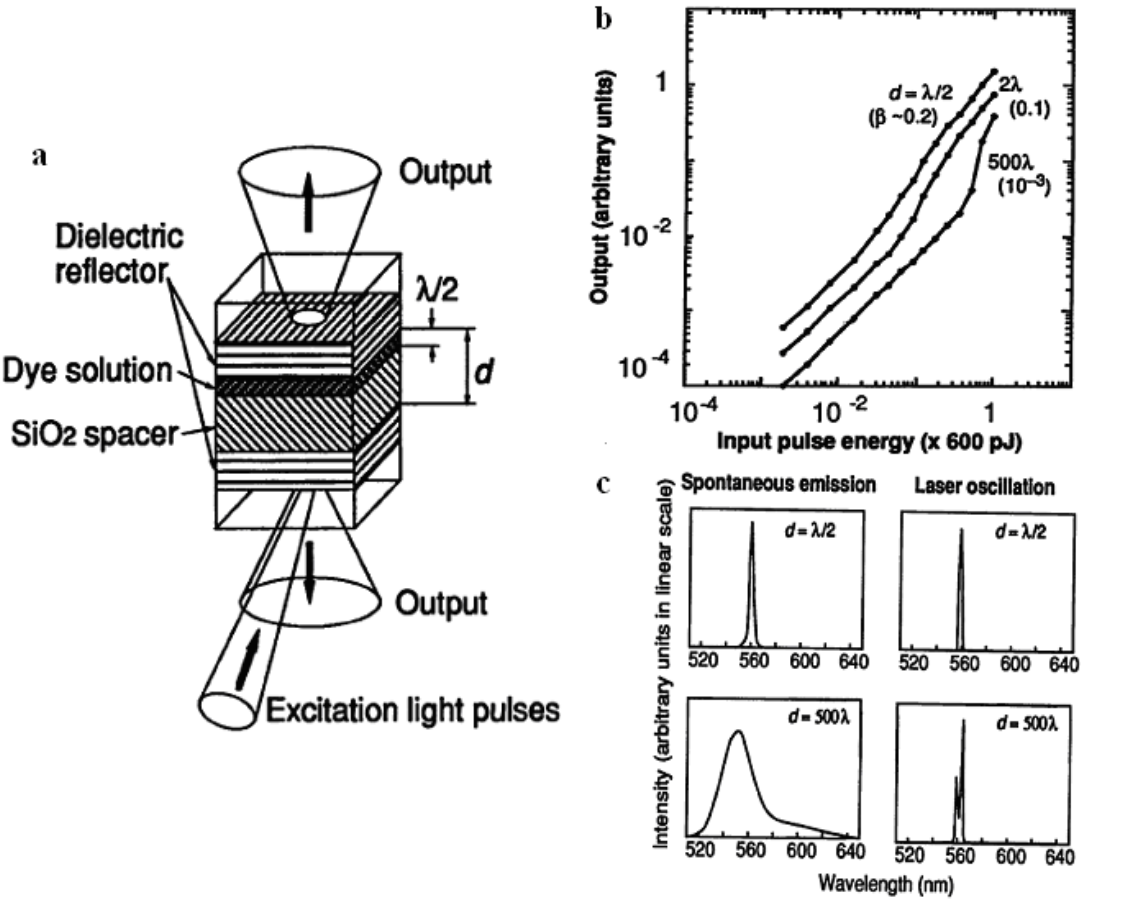

Figure 2.6: a. Schematic of a Fabry-Perot microcavity dye laser. b. Light output vs. input curves. For short cavity lasers, the laser threshold became fuzzy while a clear threshold appeared for the d = 500 cavity. c. Spontaneous and laser emission spectra. For the d = /2 cavity, the two spectra were very similar. However for the d = 500 cavity, a dramatic spectral narrowing occurred above threshold. Reprinted from [3].

short cavities, while for the long cavity it was clear. Also the spectra of the spontaneous emission and the laser action were very similar for the short cavity laser, while for the long cavity, the spectra changed dramatically above the threshold (Figure 2.6 c). Microcavities have many attractive features besides the ultralow laser threshold, such as the ultrafast response time, nonclassical photon statistics and the ability to generate well defined triggered single photons [3][39]. Therefore their implementation on a dynamical optofluidic device should be of great interest for both fundamental studies and technical applications. As we will show in the following chapters, the recent demonstrations of on-chip optofluidic dye lasers represent a big step closer towards an on-chip tunable microcavity dye laser system for studying the fundamental light-matter interactions.

2.2.1.2 Waveguide Dye Lasers

Similar to microcavity dye lasers, liquid core or liquid cladding waveguide dye lasers can be made with capillary tubes and optical fibers. Ippen and coworkers built liquid-core waveguide dye lasers by filling small diameter (~10μm) glass capillary tubes (n=1.48) with high refractive index dye solutions in benzylalcohol (n =1.53) [36]. The authors used this structure to study the photobleaching lifetimes of various laser dyes under CW laser pump. They found that Rhodamine 6G molecules in ethanol solution, when pumped at intensities required for laser action (~100kW/cm^2), have a usable lifetime of only 40ms. This work established that the short photobleaching lifetimes of most dye molecules strongly limit the usefulness of any nonflowing dye laser structures. Later, a thin film waveguide dye laser, in which the dye solution lying external to the waveguide core was excited via evanescent fields, was built to circumvent this problem because the bleached dye molecules can now be replenished by diffusion or liquid flow across the waveguide surface [70]. Zeidler built, to our knowledge, the first integrated optical waveguide dye laser by evaporating dielectric channel structures on a glass substrate and bonding a second glass plate on top [71]. A 5mm long liquid core waveguide with a cross section of 10μm by 300μm was made. The waveguide core was filled with the dye solution of Rhodamine B dissolved in benzylalcohol by capillary forces. The dye solution was then pumped by 30ns Nd:YAG laser pulses at 532nm and the laser oscillation was achieved with only the reflections from the dye solution/air interfaces at the two ends of the waveguide. Recently, with the invention of photonic crystal fibers and microstructured fibers [72], waveguide dye lasers can be made with even smaller core dimensions and longer interaction lengths, which provides a convenient platform for sensing and spectroscopy applications [73]. When a tapered optical fiber is immersed in a low refractive index dye solution and a pump laser beam is launched into the taper, an evanescent gain waveguide dye laser is achieved [37][74]. The use of a tapered fiber waveguide allows simple and efficient coupling of the pump beam, as well as the collection of the laser output. The small size of the taper also gives rise to a large modal gain coefficient due to the large evanescent tail inside the gain medium, and meanwhile ensures single transverse mode operation. Periasamy and Bor used a similar evanescent

gain structure with large diameter (50 μm) uncladded quartz fibers [75]. However, instead of using longitudinal pumping, they used the interference pattern of two pulsed N2 laser beams at 337.1nm to transversely pump the dye solution and achieved gain modulated distributed feedback (DFB) lasing. The laser wavelength can be tuned by changing the angle between the two interfering beams. A small signal gain of 430 (gain coefficient ~3cm^{-1}) at 600nm has been measured in a 2cm long fiber surrounded by an excited Rhodamine 6G solution [76]. Now with the well developed microfluidics technology, it is straightforward to build on-chip waveguide dye lasers by replacing the optical fibers or capillaries with the integrated optical waveguides [77][78].

2.2.2 Other Groups' Work on Optofluidic Dye Lasers

The first on-chip liquid dye laser based on modern microfluidics technology was demonstrated by Kristensen's group in 2003 [79]. A surface emitting Fabry-Perot cavity with metallic mirrors was fabricated on a SU8 and Pyrex glass hybrid chip by standard microfabrication techniques. A dye solution of 10mM Rhodamine 6G in ethanol was pumped through the 10 m deep and 1 mm wide microfluidic channel between the mirrors at a flow rate of 10 μl/min with a syringe pump. The optical path length between the mirrors was ~20μm. The pump light are 5ns frequency doubled Nd:YAG laser pulses at 532nm with a repetition rate of 10Hz. Laser emission at 570nm with a FWHM linewidth of 5.7nm was achieved at the pump level of 368mW/cm^2. The laser threshold was estimated to be 34mW/cm^2. Vezenov et al. fabricated an edge emitting dye laser in poly(dimethylsiloxane) (PDMS) using soft lithography [77]. The laser cavity was based on a liquid-liquid (L^2) waveguide [80]. Gold mirrors deposited at the ends of the waveguide form a Fabry-Perot cavity. The L^2 waveguide allowed the dynamical control of the waveguide and cavity properties by adjusting the index contrast between the core and cladding liquids. By mixing methanol and DMSO, peak lasing wavelength was tuned from 617nm to 634nm. A free space ring cavity based microfluidic dye laser was fabricated in a photoechable glass, Foturan, by femtosecond laser microprocessing [81]. The 3D microprocessing permitted the fabrication of devices with multi-layered structures. An array of two lasers operated simul-

taneously under one pump light was demonstrated.

The early demonstrations of on-chip optofluidic dye lasers showed rather wide emission linewidths due to multiple mode operation and low cavity qualities. Such wide band emission is hard to distinguish from the amplified spontaneous emission (ASE). Later, more efficient cavities were achieved using Bragg gratings, which enabled narrow linewidth single frequency output. Balslev and Kristensen demonstrated a single-mode dye laser based on a multimode waveguide structure and a ~130th Bragg grating [82]. Approximately single spatial mode operation was observed due to the high losses of higher order spatial modes in the antiguiding segments.

Shortly after the demonstration of the first optofluidic dye laser, tunable output was obtained by index and concentration tuning [83][84][85]. By using a mixture of two dye molecules in a single solvent, dual-color output was achieve with an optical fiber based Fabry-Perot cavity microfluidic dye laser [86]. Two gold coated cleaved optical fibers were placed in the PDMS channel to form a short Fabry-Perot cavity (140 μm cavity length). Collinear yellow (559nm) and red lasing (597nm) was obtained when a mixture of Rhodamine 6G and Surforhodamine 101 in ethanol was pumped by pulsed 532nm laser light.

The integration with other "lab-on-a-chip" components to build complete systems is a major motivation for building optofluidic dye lasers. However, very few demonstrations along this line have appeared so far. Galas et al. have demonstrated the integration of PDMS based soft microfluidics with optofluidic dye lasers to tune the laser wavelength [84]. Such integration can also be used to build sensing and spectrometer devices. A device capable of performing sensitive intracavity absorption measurements on nanoliter samples was built [87]. Concentrations of methylene blue as low as 10^{-6} mol/l were detected. Balslev et al. demonstrated a more sophisticated "lab-on-a-chip" system, which contained a liquid dye laser, optical waveguides, a microfluidic mixer, a sample cuvette and photodiodes [88]. The dye laser light at 576nm was directly coupled into five waveguides that delivered the light to five different locations along a fluidic channel (cuvette) for absorbance measurements. The transmitted light was collected at the other side of the cuvette, again by waveguides, and finally detected by the photodiodes. Electrical read-out was accomplished by integrated metal connectors. To demonstrate the concerted operation

of the integrated components, the authors performed an absorbance measurement on two different concentrations of xylenol orange dye. The photodiode signal showed two different values for concentrations of 0.06mM and 0.12mM. Despite the high level integration, this device was still not a stand alone system due to the off chip optical pump and the pressure source for driving the liquid flow.

Chapter 3

Single Mode Optofluidic Distributed Feedback (DFB) Dye Lasers

Several groups have demonstrated on-chip liquid dye lasers using different materials and laser cavity geometries[79][77][84]. Such lasers allow the integration of coherent light sources with other microfluidic and optical functionalities, and are of great interest for making fully functional 'lab-on-a-chip' systems. However, the lack of both transverse mode and longitudinal mode selection in these demonstrations led to multiple mode operation and wide emission linewidths (~5nm) that are hard to distinguish from amplified spontaneous emission (ASE). Until recently, the true single mode operation has been not available in such devices. In this chapter we present a single mode optofluidic dye laser using a phase shifted 15th order distributed feedback (DFB) structure embedded in a single transverse mode liquid-core waveguide fabricated on a monolithic PDMS device[78]. DFB cavities combined with 3D optical waveguides are very efficient structures for making stable single frequency lasers . Their implementation on a microfluidic chip can greatly improve the performances of microfabricated liquid dye lasers.

3.1 Distributed Feedback (DFB) Lasers

Distributed Feedback (DFB) lasers use Bragg gratings, periodic changes in the refractive index or gain, as the optical feedback element. Although their most successful application is in the single frequency semiconductor lasers for telecommunications[89], the first DFB laser was actually a dye laser demonstrated by Kogelnik and Shank in 1971 at

Bell Lab[90]. The DFB structure is very efficient for making stable single frequency lasers due to the strong Bragg condition determined by the periodic structure. Also the DFB structure is particularly suitable for the planar microfabrication techniques. Now with the development in soft lithography, very similar structures to that of a guided-wave DFB semiconductor laser can be built on a PDMS microfluidic chip with liquid dye solutions as the gain medium. In this section, we will describe the basic theory and simulation tools for understanding and designing the DFB structrues. Special structures used in this thesis such as the phase-shifted DFBs and higher order DFBs are discussed.

3.1.1 Theory and Simulations of DFB Structures

For an optical wave propagating in a DFB structure, strong reflectivity occurs when the Bragg condition is satisfied:

$$m\lambda_m = 2n_{\text{eff}}\Lambda \tag{3.1}$$

where λ_m is the mth order Bragg wavelength, n_{eff} is the effective index of the guided mode and Λ is the grating period. This condition can be easily obtained by considering the phases of the consecutive reflections from the periodic unit cells. At the Bragg wavelength, the reflections from the unit cells add up in phase, giving rise to the frequency dependent high reflectivity (stop band). For laser applications, the detailed frequency response of the resonant structure is needed to determine the lasing wavelength. There are several standard approaches for calculating the reflection and transmission spectra of a DFB Structure. The most popular one is the coupled-mode theory, in which the coupling between the two counter-propagating modes in the structure are described by two coupled first order differential equations[91][92]. The coupling strength is expressed as a coupling coefficient determined by the waveguide structure and the grating profile. Although this method is fast and the analytical solution can be found for the uniform grating case, the evaluation of the coupling coefficients and the application of this method to arbitrary grating structures are not straightforward. In this thesis, we use another approach called Rouard's method[93], which essentially treats each grating half-period like a homogenous dielectric layer in a

thin-film stack. This approach needs more computational time because the number of layers scales with the number of grating periods. However, with the ever increasing computational power, the spectra of moderately long DFB structures used in this thesis (typical number of layers is 10000) can be easily obtained with a desktop PC in less than a minute. Also this method can be used to simulate arbitrary grating profiles such as chirped gratings, phase-shifted gratings and superstructure (sampled) gratings.

In Rouard's method, the three dimensional waveguide DFB structure is simplified to a one dimensional problem consisting of periodic dielectric slabs as shown in Figure 3.1-(c). The refractive index of each slab is given by the effective index of the waveguide mode at the corresponding location in the original DFB structure. The waveguide modes are thus represented by the two counter-propagating plane waves a_i and b_i traveling perpendicular to the slabs. One thing to point out is that in this case we do not need to treat the TE and TM polarizations differently since they are now indistinguishable. The effect of passing through a dielectric interface or traveling over a distance in a uniform medium can be represented by a *transmission matrix* (T-matrix) which relates the two waves a_1 and b_1 at the input to the waves a_2 and b_2 at the output.

$$\begin{bmatrix} a_1 \\ b_1 \end{bmatrix} = \mathrm{T} \begin{bmatrix} a_2 \\ b_2 \end{bmatrix} \tag{3.2}$$

For a dielectric interface between two materials with refractive indices n_1 and n_2, the T-matrix can be found by using the Maxwell's equations and matching the boundary conditions at the interface[20], and it can be written as

$$\mathrm{T} = \frac{1}{t} \begin{bmatrix} 1 & r \\ r & 1 \end{bmatrix} \tag{3.3}$$

where r and t are the Fresnel coefficients given by [94],

$$r = \frac{n_1 - n_2}{n_1 + n_2} \tag{3.4}$$

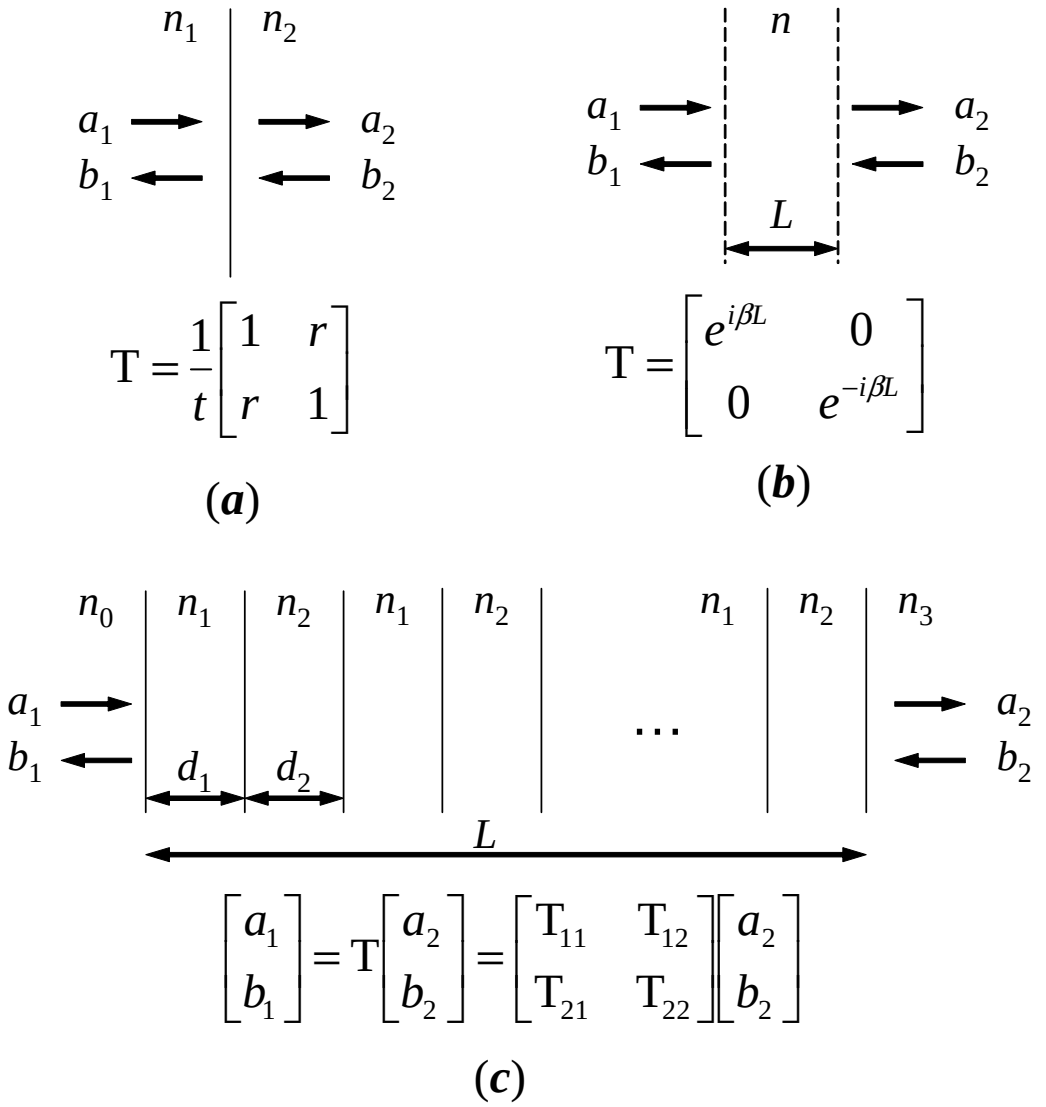

Figure 3.1: Transmission matrices in Rouard's method for simulating the spectra of a DFB structure. (a). Dielectric interface. (b). Propagation over a distance with no discontinuities. (c). Bragg grating.

and

$$t = \frac{2n_1}{n_1 + n_2} \tag{3.5}$$

The T-matrix for propagating a distance L in a uniform medium with index n is given by

$$\mathrm{T} = \begin{bmatrix} e^{i\beta L} & 0 \\ 0 & e^{-i\beta L} \end{bmatrix} \tag{3.6}$$

where $\beta = 2\pi n/\lambda$ is the the propagation constant and λ is the wavelength. Clearly, the one dimensional DFB structure shown in Figure3.1-(c) can be decomposed into dielectric interfaces and uniform dielectric slabs, and its overall T-matrix can be calculated by multipling the T-matrices for each elements in the proper order. Once the overall T-matrix is available, the amplitude reflection and transmission coefficients are given by (setting $a_1 = 1$ and $b_2 = 0$)

$$r = \frac{\mathrm{T}_{21}}{\mathrm{T}_{11}} \tag{3.7}$$

and

$$t = \frac{1}{\mathrm{T}_{11}} \tag{3.8}$$

Then the power reflectance R and transmittance T are simply

$$R = |r|^2 = \left|\frac{\mathrm{T}_{21}}{\mathrm{T}_{11}}\right|^2 \tag{3.9}$$

and

$$\begin{aligned} T &= \frac{n_3}{n_0}|t|^2 = \frac{n_3}{n_0}\left|\frac{1}{\mathrm{T}_{11}}\right|^2 && (3.10) \\ &= 1 - R \quad \text{(for lossless structures)} && (3.11) \end{aligned}$$

Figure 3.2 shows an example simulated transmittance spectrum for a DFB structure with

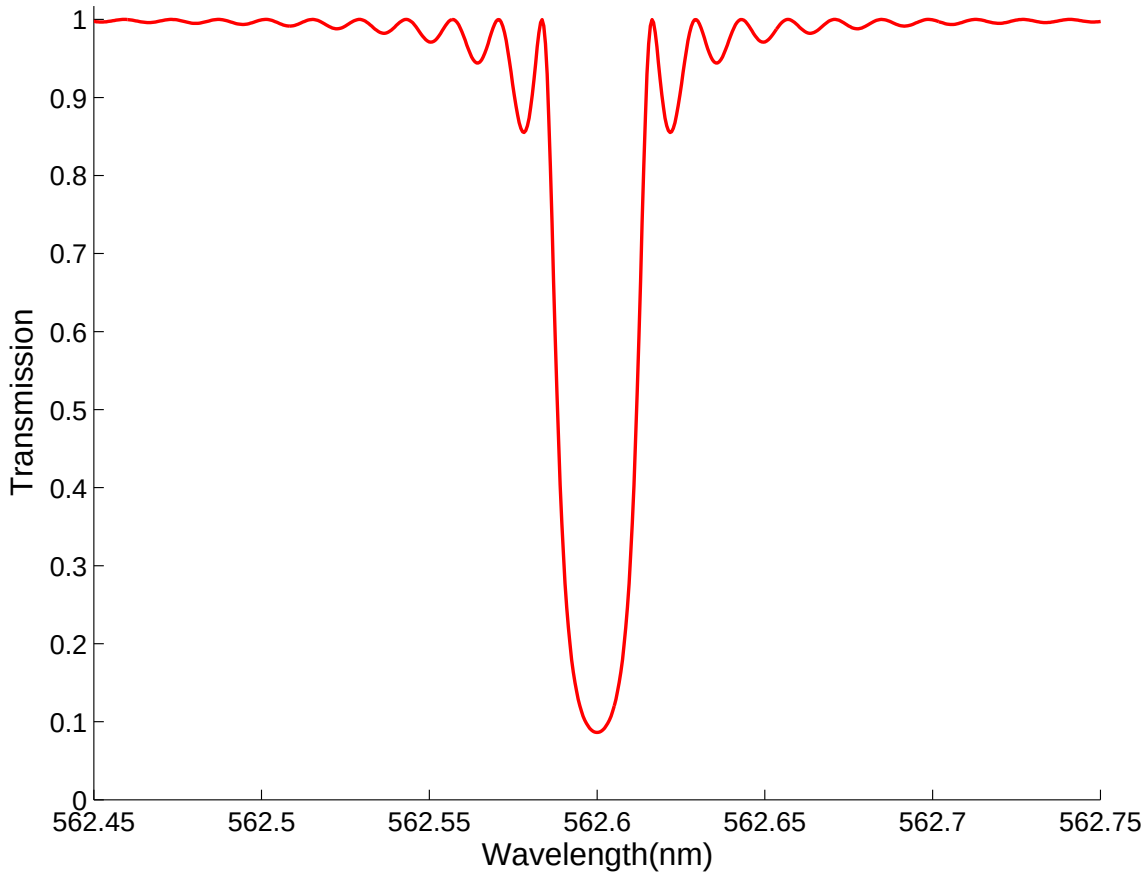

Figure 3.2: Simulated transmittance spectrum for a DFB structure with parameters: $n_0 = n_3 = 1.406$, $n_1 = 1.407$, $n_2 = 1.406$, $d_1 = d_2 = 1.5\mu$m, and the grating length $L = 8$mm.

the parameters: $n_0 = n_3 = 1.406$, $n_1 = 1.407$, $n_2 = 1.406$, $d_1 = d_2 = 1.5\mu$m, and the grating length $L = 8$mm.

3.1.2 $\lambda/4$-shifted DFB Lasers

As can be seen in Figure 3.2, a uniform DFB with a index grating is antiresonant at the Bragg wavelength, meaning lasing cannot occur at this wavelength. One way to understand this is to take the central half-period as the cavity and the gratings to the left and right as the mirrors. Because the cavity is a $\lambda/4$ long at the Bragg wavelength, light propagating in the cavity will be exactly π out of phase after one round trip. Therefore the Bragg wavelength cannot be a transmission resonance which requires the round trip phase change be an integral multiple of 2π. In fact a uniform index grating has two degenerate resonances

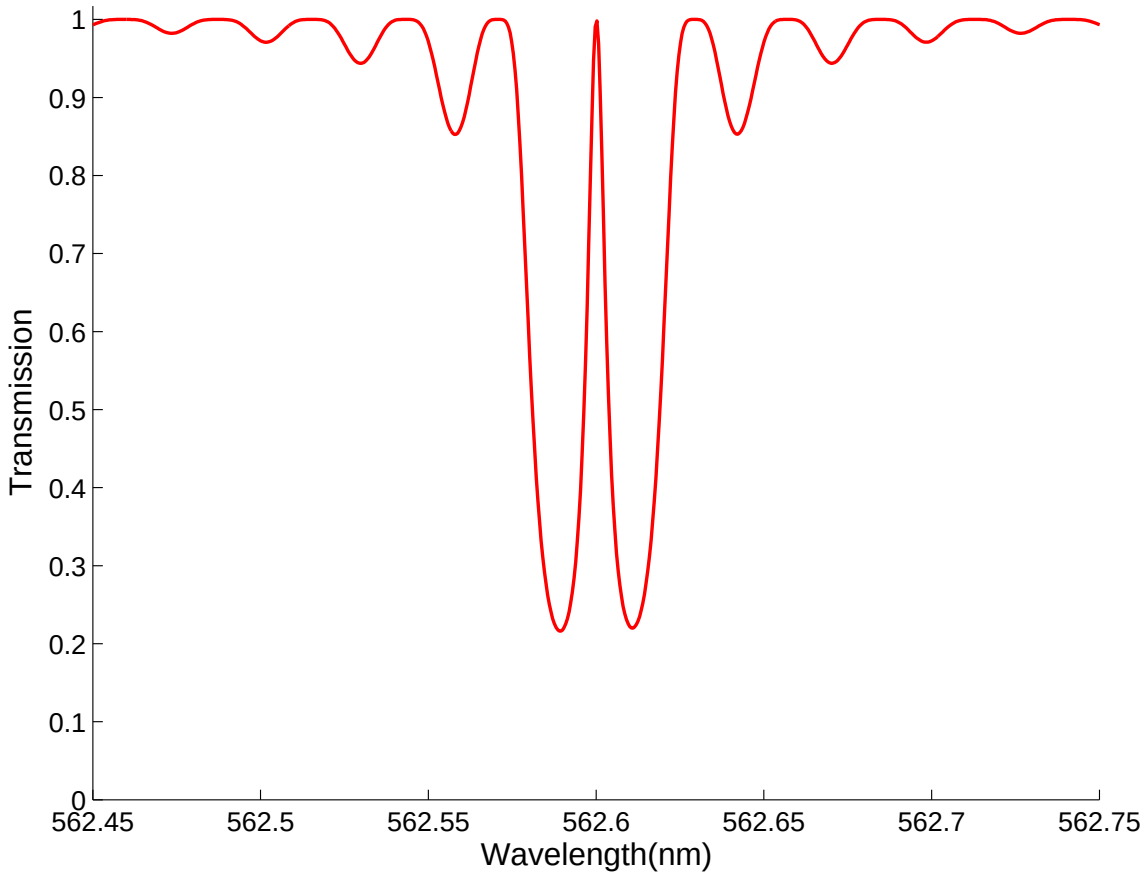

Figure 3.3: Simulated transmittance spectrum for a $\lambda/4$-shifted DFB structure with the same parameters as those in Figure 3.2 except that the central slab has been increased to twice its original length $d_{defect} = 3\mu$m to form a defect. The central defect gives rise to a transmission resonance inside the bandgap.

located at the two sides of the stop band. In practice, a uniform DFB laser with a index grating can oscillate in either one of the two modes depending on the random phases of the end facet reflections[92]. To ensure single longitudinal mode operation, a $\lambda/4$ phase shift can be introduced at the center of the grating (i.e. to increase the center half-period to twice its original length). Figure 3.3 shows the simulated transmittance spectrum for a $\lambda/4$-shifted DFB structure with the other parameters the same as those used in Figure 3.2. In this case only a single resonance is located at the Bragg wavelength and the degeneracy is removed. There are some shortcomings of this structure including the spatial hole burning effects, difficulty in fabrication and the need for very low facet reflectivities[95]. Therefore other structures such as gain-coupled gratings[92] are also used to obtain single frequency

operation.

3.1.3 Higher Order DFB Structures

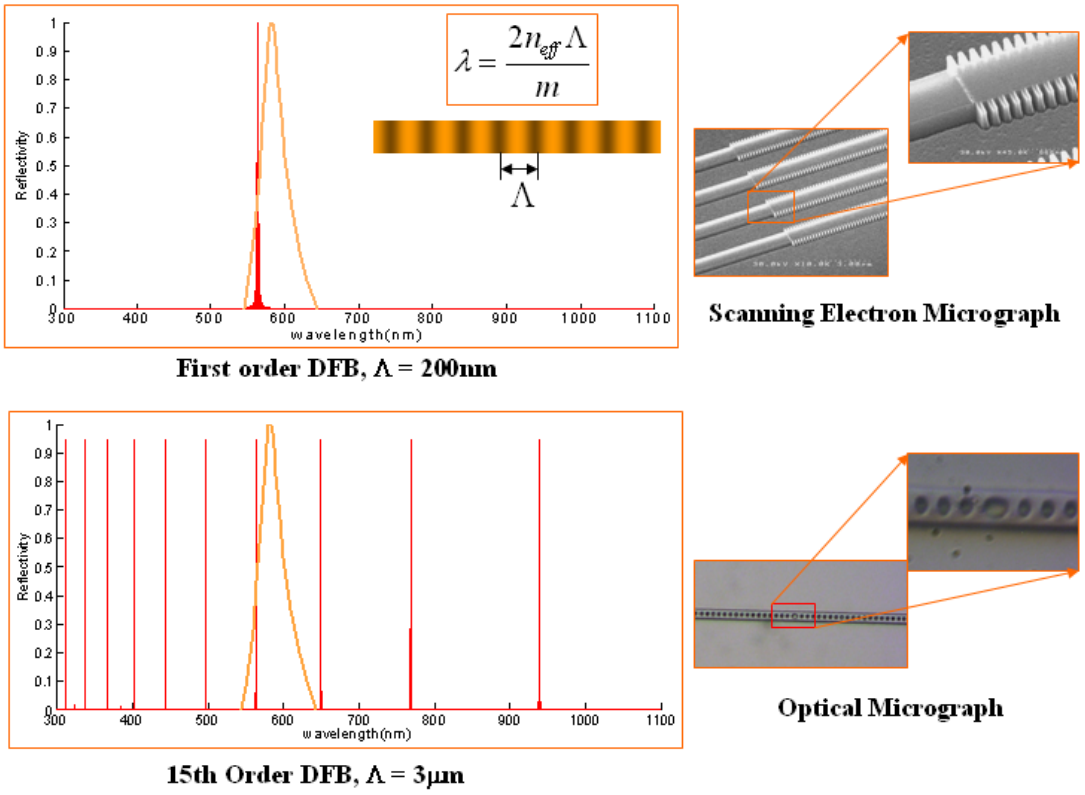

Figure 3.4: Comparison of a first order DFB and a higher order DFB structure.

In most practical DFB lasers, first order gratings are used to achieve low threshold, high efficiency and compact devices. However, in the work of this thesis, we used mainly higher order gratings with order numbers from 5 to 15. Our choice of higher order DFBs is mainly due to fabrication considerations. For first order DFBs operating in the visible range (more specifically, 550nm to 650nm because of the dyes used in this work), the grating periods are on the order of 200nm. Such small feature sizes can only be achieved with advanced fabrication techniques such as E-Beam Lithography, EUV and X-ray lithography. Another problem comes from PDMS, the soft elastomer material we used. Microfluidic channels in PDMS with 100nm dimensions are much easier to collapse than channels with larger

dimensions (say 2μm to 100μm), especially after the O_2 plasma treatment. Detailed discussions on the fabrication issues can be found in the Section 3.3. The smallest structures in PDMS we have achieved so far have the following dimensions: channel width 900nm, channel height 250nm, and grating period 1μm. On the other hand, we can easily fabricate higher order DFB structures with 1-2μm feature sizes using conventional photolithography.

One interesting property of higher order DFBs is that if we choose the grating periods appropriately, a single cavity can support multiple resonances across the whole visible spectrum. This can be seen from the reflectivity spectra shown in Figure 3.4. For the first order DFB cavity, there is only one resonance from 400nm to 700nm, while there are four resonances in this region for the 15th order DFB cavity with a grating period of 3μm. Meanwhile, the free spectral range (FSR) for the 15th order DFB is still large enough so that there is only one resonance within the gain spectrum of a dye molecule (for example, the curve shown in the figure is the Rhodamine 6G gain spectrum). This feature can be used to achieve multiple color lasing from the same cavity by switching between different dye molecules, as long as a suitable pump light can be found for each dye.

However, compared with the first order DFB structure, higher order DFB cavities are less efficient in terms of light confinement because the coupling coefficient is inversely proportional to the order of the Bragg grating [96]. This can be compensated, to some degree, by increasing the cavity length to provide strong enough feedback. Also, in higher order DFBs, there exist extra out-of-plane radiation losses due to lower order scattering processes. This fact has been exploited to make surface emitting DFB lasers [97].

3.2 Laser Cavity Design

The schematic diagram of our optofluidic DFB dye laser is shown in Figure 3.5. The laser chip is entirely made of poly(dimethylsiloxane) (PDMS), a silicone elastomer which has become popular for microfluidics[5][98] and nanofabrication[4][99], and has good optical properties in the visible region[100]. A sufficiently small microfluidic channel when filled with a dye solution of higher refractive index than that of PDMS (n_{PDMS} = 1.406 for GE RTV615) acts as a single mode optical waveguide. The gain medium is a 1mM

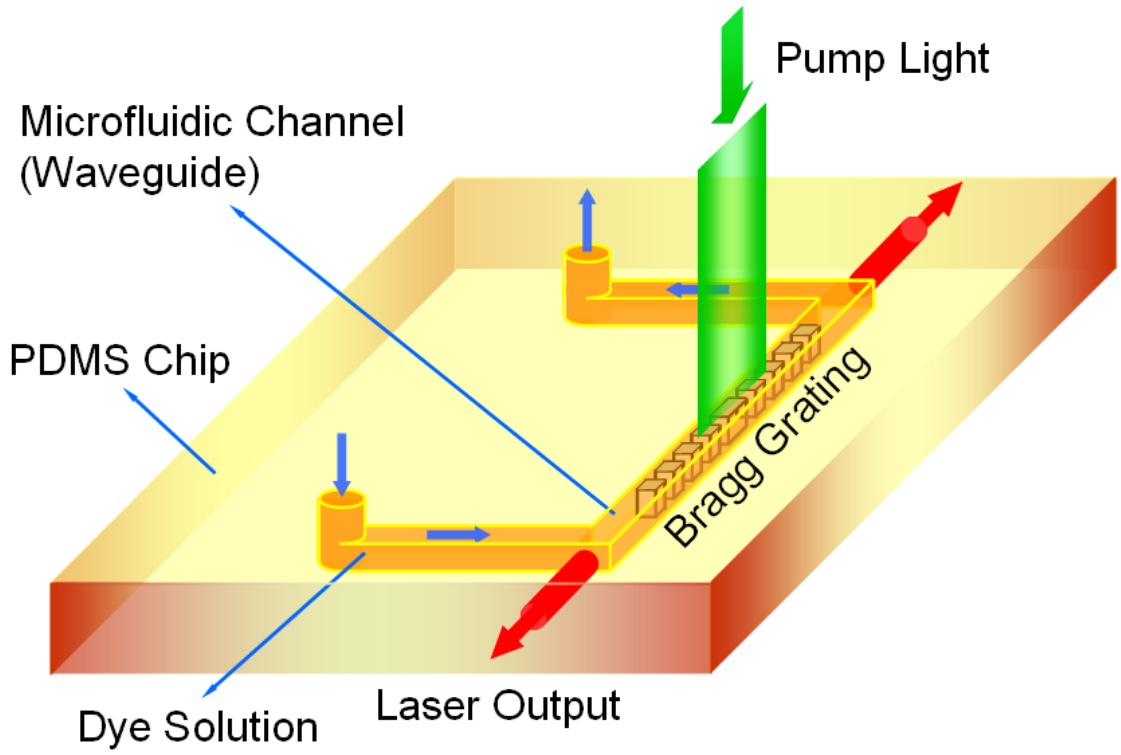

Figure 3.5: Schematic diagram of a monolithic optofluidic DFB dye laser chip.

solution of Rhodamine 6G in a methanol and ethylene glycol mixture with refractive index of 1.409. The periodic PDMS posts inside the channel form a 8mm long 15th order Bragg grating which provides the optical feedback necessary for the laser action. In addition, a $15\pi/2$ (effectively $\lambda/4$) phase shift is introduced at the center of the grating to ensure single frequency operation as discussed before. The PDMS posts also provide mechanical support to prevent the microfluidic channel from collapsing.

3.2.1 Longitudinal and Transverse Mode Selection

To make a single mode laser, both the transverse mode and longitudinal mode selection need to be carefully designed. We choose the waveguide to be 5μm wide and 2μm high. The reasons for this are two fold: first, the waveguide dimensions are relative small yet still easily achievable by photolithography; second, the 2:5 aspect ratio is large enough so that the PDMS channel will not collapse. Correspondingly, the PDMS posts inside the

channel were designed to be 3μm wide and 1.5μm (half grating-period) long. For a channel waveguide with a 2μm by 5μm core, finite element simulation (Comsol FEMLAB 3.2 with the Electromagnetics module) shows that the index difference needs to be smaller than 0.003 to maintain single mode. Given the index of PDMS is 1.406 (GE RTV 615), this means the index of the dye solution has to be smaller than 1.409. This can be specified by mixing two different organic solvents. The choice of solvents is limited due to the swelling problem of PDMS in most organic solvents [101]. The PDMS compatible solvents which are also used in conventional dye lasers include: ethanol, methanol, water, ethylene glycol and dimethylsulfoxide (DMSO), the refractive indices of which are listed in Table 3.1. We used a mixture of methanol and ethylene glycol which has a refractive index of 1.409. The available refractive index range with the listed solvents is from 1.33 to 1.478, which can lead to a quite large tuning range when used in fluidically tunable optical devices.

Table 3.1: Refractive indices of PDMS compatible solvents

Solvent	Refractive Index†
Methanol	1.33
DI Water	1.333
Ethanol	1.36
Ethylene Glycol	1.43
Glycerol	1.473
DMSO	1.478
Benzyl Alcohol	1.54∗

†At room temperature, sodium D line 589.3nm.
∗Not fully tested yet.

If we define the x direction along the width and the y direction along the height, the E_{11}^x mode (transverse E field along x direction, TE-like) is more confined than the E_{11}^y mode, and thus is the preferred lasing mode. The effective indices of the guided modes were calculated using a Finite-Element Method (FEM) mode solver (Comsol FEMLAB 3.2 with the Electromagnetics module). These indices were also used in the longitudinal mode spectrum simulation as discussed in Section 3.1.1. The small cross-section area not only reduces the required pump power to achieve the lasing threshold but also results in an extremely small consumption of dye solution (less than 40 picoliter per channel). To

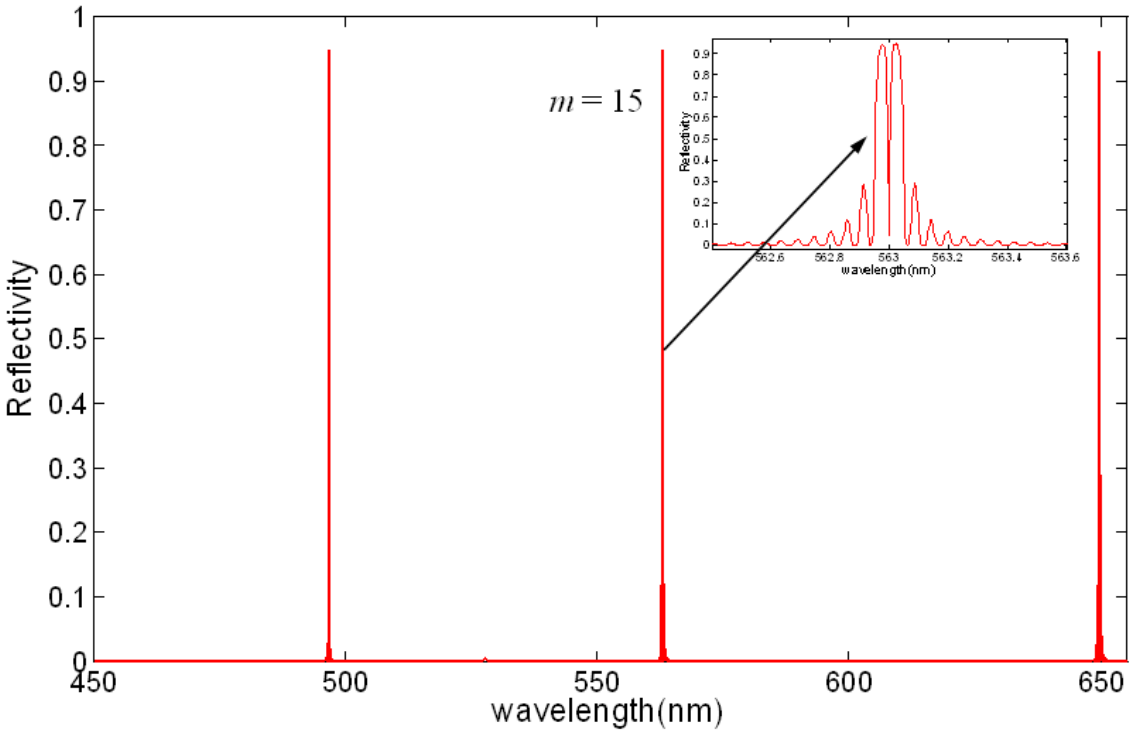

Figure 3.6: Simulated reflectivity spectrum of a 15 phase shifted 15th order DFB structure. The curve spanning from 550nm to 650nm is the gain spectrum of Rhodamine 6G. The inset shows the enlarged plot the 15th resonance at 563nm.

obtain stable single frequency operation, the FSR of the employed cavity structure has to be larger than the gain spectral bandwidth. Organic dye molecules are well known to have very broad gain spectra with a typical bandwidth of 30nm to 50nm (full width at half maximum FWHM). This forces the characteristic length of the resonant structure to be shorter than 4 μm. As given in Section 3.1.2, the lasing wavelength for a $\lambda/4$-shifted DFB laser is determined by the Bragg condition (Eq 3.1). Accordingly, the FSR is given by:

$$FSR = \frac{\lambda_m}{m-1} = \frac{\lambda_m^2}{2n_g\Lambda} \tag{3.12}$$

Therefore for a DFB structure with Λ = 3 μm (1.5 μm + 1.5 μm) and the group index n_g = 1.407, the 15th resonant wavelength and the FSR are 563nm and 40.2nm respectively. In addition the even order resonances are absent when a 50% duty-cycle square-wave shaped grating is used. The resulting effective FSR of ~90nm ensures only a single resonance

inside the gain spectrum of Rhodamine 6G which spans from 550nm to 650nm. However, as discussed in Section 3.1.2, it is well known that a DFB laser with a uniform index grating operates not at the Bragg wavelength but instead at the two degenerate wavelengths situated symmetrically on either side of the Bragg wavelength [10]. To break this degeneracy, an effective $\lambda/4$ shift is introduced at the center of the grating. Figure 3.6 shows the simulated reflectivity spectrum of the overall structure using Rouard's method given in Section 3.1.1. The parameters used are: Λ = 3 μm (1.5 μm PDMS post + 1.5 μm dye solution), grating length L = 8mm, $15\pi/2$ phase shift at the center, core index n_{core} = 1.409, and cladding/post index n_{clad} = 1.406. It is clearly seen that only the 15th resonance falls in the gain spectrum of Rhodamine 6G. The inset of Figure 3.6 shows the detailed 15th resonance, where the transmission resonance (high-pass dip) inside the stop band corresponds to the lasing mode.

As discussed before, an interesting property of the higher order DFB structure is that it enables multiple color lasing in the same cavity each at a single frequency. For example, the simulated spectrum (Figure 3.6) shows that the DFB structure employed in this chapter can support 497nm, 563nm and 650nm lasing as long as a suitable dye solution and a corresponding shorter wavelength pump source are chosen for each wavelength. This is a highly desired feature for applications where multi-wavelength laser sources are needed such as multi-color flow cytometry [102] and multiplex real time polymerase chain reactions (PCRs).

3.3 Fabrication

The fabrication of the optofluidic DFB dye laser uses the same replica molding soft lithography technique which is widely used to make microfluidic devices[4][5]. The fabrication process flow is shown in Figure 3.7. The detailed fabrication recipes can be found in Appendix A. Briefly, we started the fabrication by making a high resolution Chrome mask using a direct laser pattern generator, DWL 66. Then we created a patterned photoresist mold on a silicon wafer using conventional photolithography. SU8-2002 negative photoresist (MicroChem) was spin-coated at 3000rpm for 30 seconds on a silicon wafer yielding a thickness of 2μm. The photoresist was then patterned with a Cr-on-glass mask on a

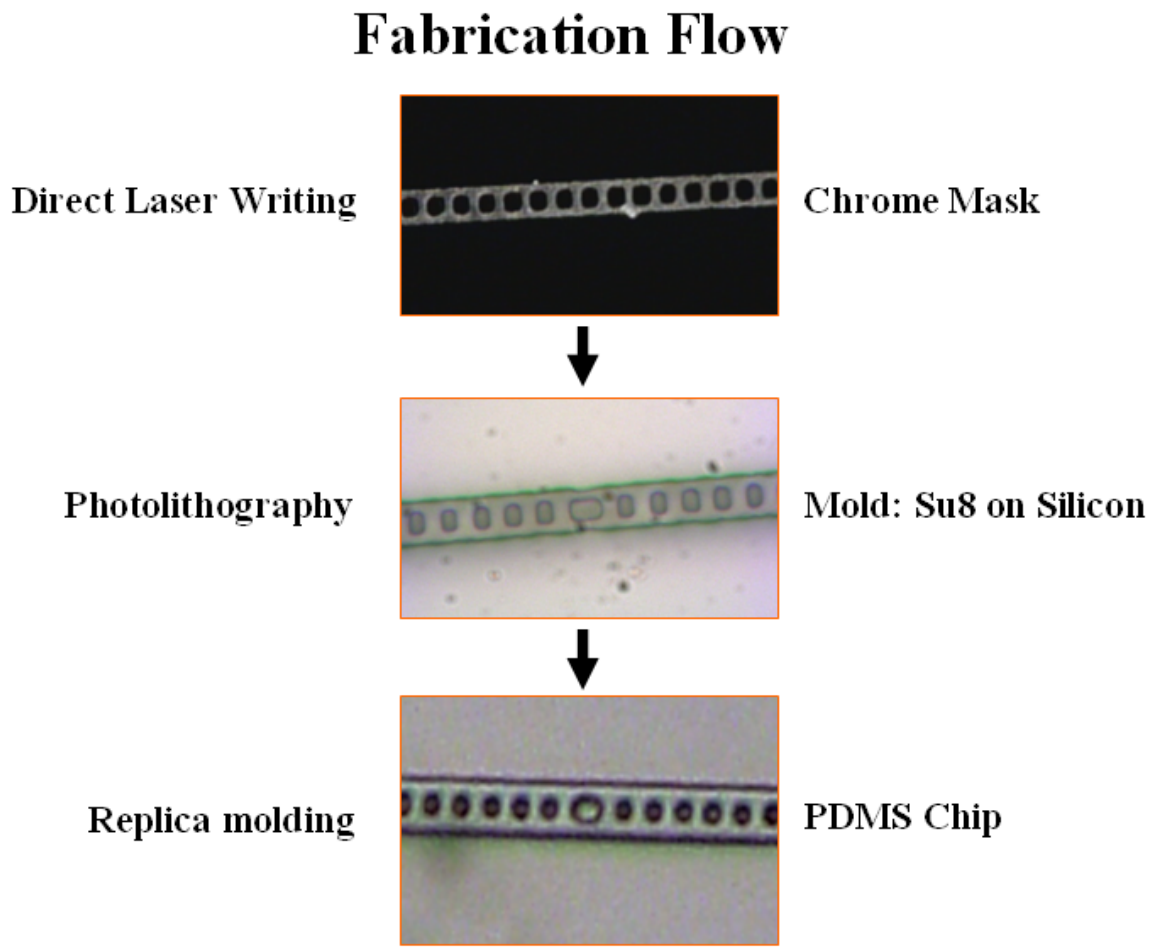

Figure 3.7: Fabrication flow chart for the optofluidic DFB dye lasers

SUSS MJB 3 mask aligner (13 seconds at 4.5mW/cm^2). The soft bake, post exposure bake and development of SU8 followed the manufacturer's instructions. The mold was treated with trimethylchlorosilane (TMCS) (Aldrich) vapor for 5 minutes before use to facilitate the release of PDMS. Then 5:1 part A:B PDMS prepolymer (GE RTV 615) was poured onto the mold and degassed in a vacuum chamber for 30 minutes. The prepolymer was then partially cured in an 80^{o}C oven for 30 minutes. The partially cured PDMS was peeled from the master and the liquid inlet and outlet ports were punched through the whole layer by using a 0.055-inch punch (Technical Innovations, Gaithersburg, MD). This patterned PDMS, containing the DFB structure, was then treated with oxygen plasma for 10 seconds at 80W and permanently bonded to another featureless PDMS to form a monolithic de-

vice. Finally, the resulting device was cut to size and baked at 80^{o}C overnight for complete cross-linking. Figure 3.8 shows an optical micrograph of the fabricated PDMS DFB laser cavity. An actual laser chip is shown as the inset.

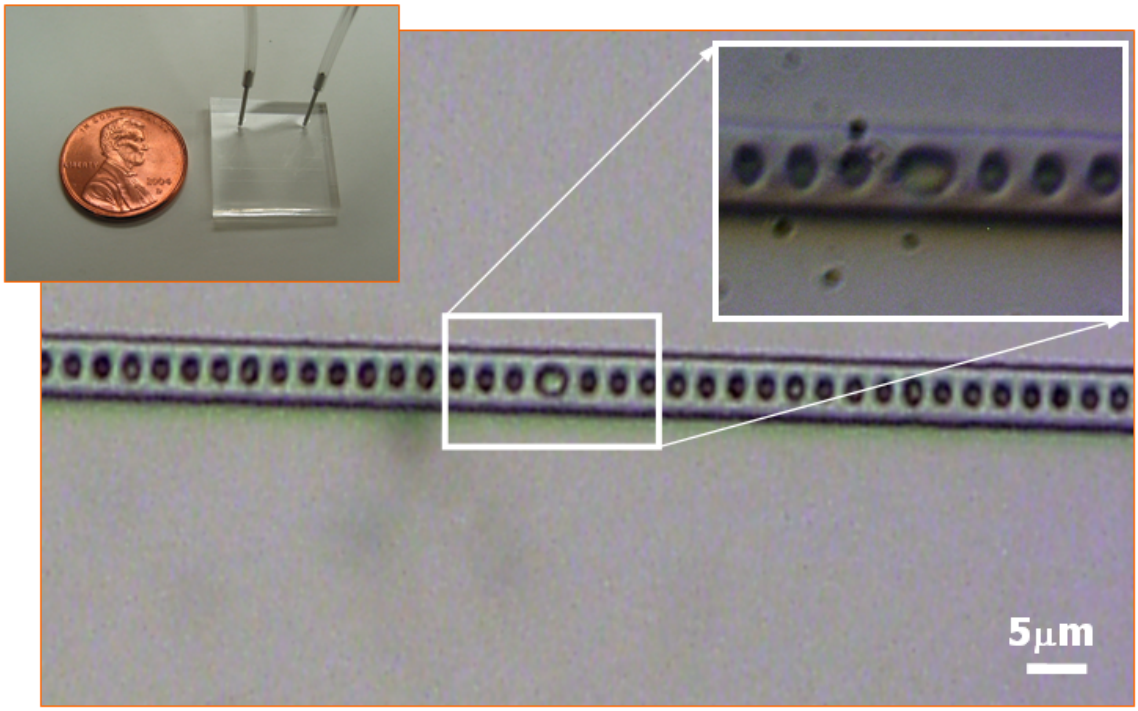

Figure 3.8: Optical micrograph of a microfluidic channel with an embedded phase shifted 15th order DFB structure on a PDMS chip. The grating period is 3μm. The channel width is 5μm. The central larger PDMS post introduces a 15π/2 phase shift. The upper left inset shows the picture of an actual optofluidic dye laser chip.

3.4 Lasing Results and Discussion

The dye solution was introduced into the microfluidic channel by applying 10psi pressure at the inlet port. We found, to operate the laser in the pulsed mode, it is not necessary to circulate the dye solution although continuous circulation does increase the output power. The characterization setup was extremely simple as shown in Figure 3.9. The laser chip was optically pumped with 6ns Q-switched frequency doubled Nd:YAG laser pulses of 532nm wavelength, focused to a ~100μm wide stripe aligned with the microfluidic channel. A 10X microscope objective was used to collect the emission light from one edge of

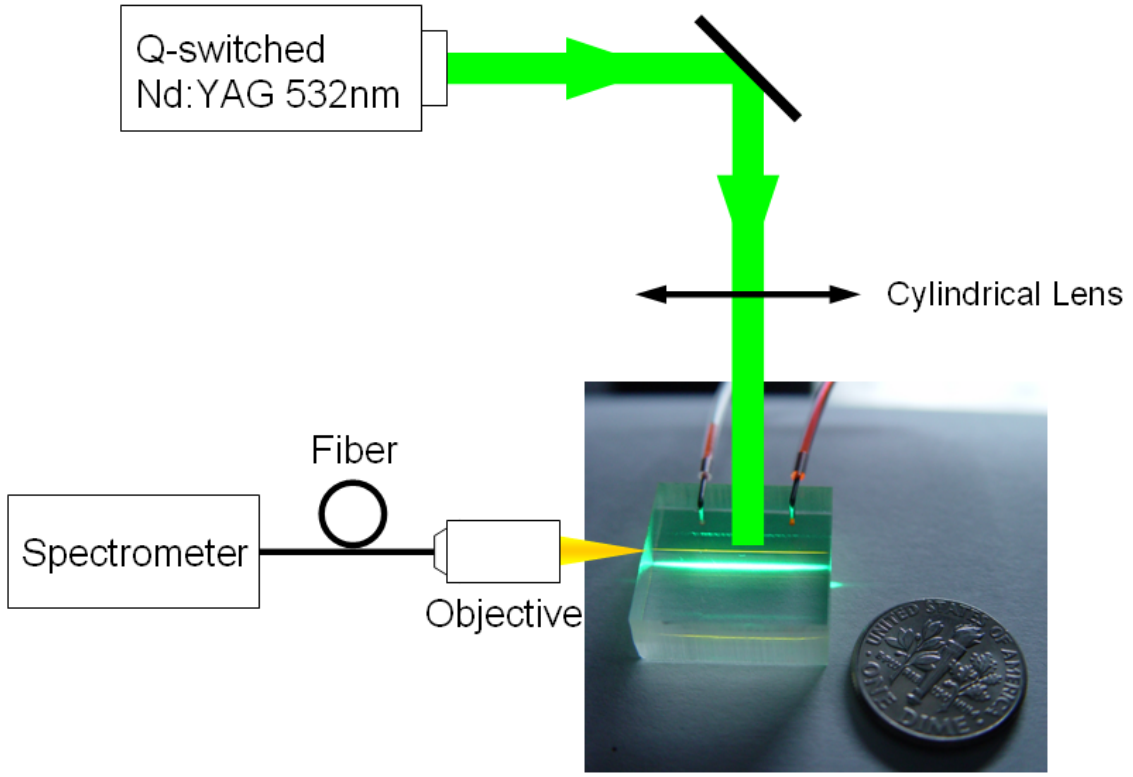

Figure 3.9: Characterization setup for the optofluidic dye lasers.

the chip and deliver it to a fiber coupled CCD-array based spectrometer with 0.1nm resolution (Ocean Optics HR4000). A typical single mode lasing spectrum is shown in Figure 3.10 where the lasing wavelength is 567.3nm, very close to the predicted value 563nm. The measured linewidth is 0.21nm for this particular device. Later, with improvements in the fabrication, we obtained laser linewidth < 0.1nm which is the resolution limit of our spectrometer. A plot of laser output energy versus the absorbed pump energy is shown as Figure 3.11. The threshold pump fluence is estimated to be ~0.8mJ/cm^2, which gives a peak pump intensity around 150kW/cm^2. This pump intensity is well within the reach of commercial high power visible laser diodes and diode pumped solid state lasers (DPSS), thus allowing the use of inexpensive compact laser systems or even light emitting diodes (LEDs) as the pump sources to construct low-cost and compact portable devices. The laser remains single mode at pump levels as high as 8mJ/cm^2. Further increase in the pump power damaged the PDMS chip. At moderate pump intensities (~200kW/cm^2) and 10Hz repetition rate, stable laser output lasted longer than 20 minutes and the chip can be reused many times after proper cleaning with ethanol. However, dye molecules (especially the hy-

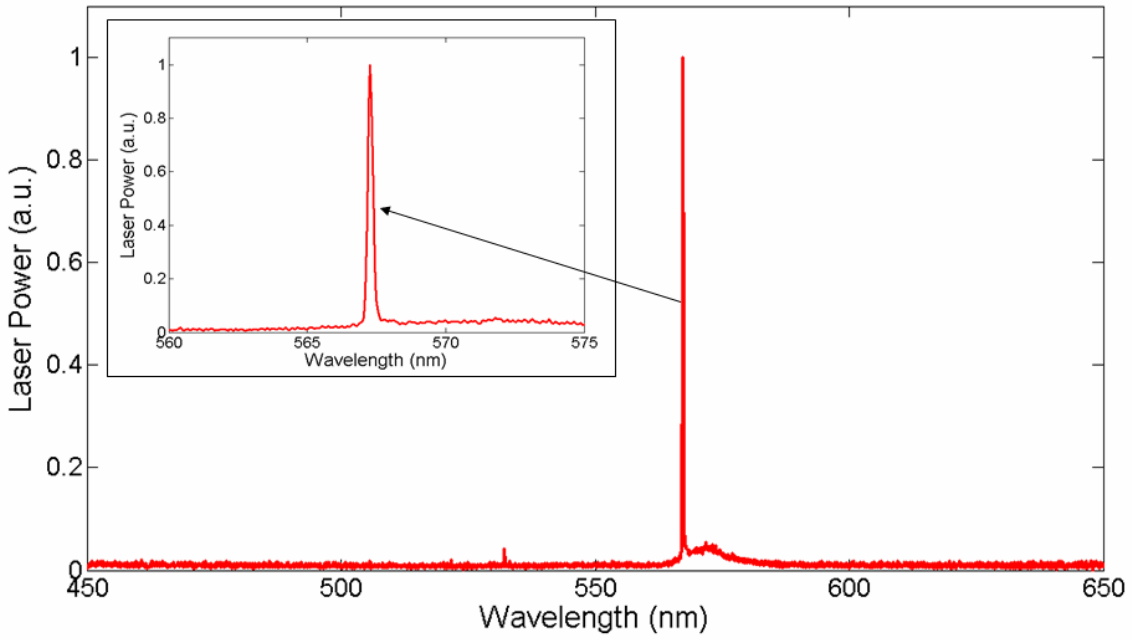

Figure 3.10: Single mode optofluidic DFB dye laser spectrum. The measured linewidth is 0.21nm.

drophobic ones) can be absorbed into PDMS gradually and decrease the waveguide quality due to the bleached dye absorption.

The linear flow rate at the center of the channel can reach 1mm/s at reasonable pressure (10-30psi). Considering the typical photobleaching time of Rh6G is ~50ms under pump intensities required for laser threshold (~100kW/cm^2) [36], this flow rate is fast enough to prevent the majority of the dye molecules from photobleaching under pulse operation up to 500kHz. However the dye molecules near the channel wall move at very low velocities due to the parabolic profile of the flow rate. Therefore they tend to get bleached before moving out of the pump region. This problem can be solved by using a liquid core/liquid cladding waveguide structure in which the dye solution is surrounded by a low refractive index sheath flow [80]. In this way, not only the dye solution is moving at a more uniform speed but also the channel dimensions can be large to enable higher flow rate.

We have measured laser output energy >1pJ per pulse without damaging the chip. Assuming a 10ns pulse width, this corresponds to an average power of ~100μW per pulse and an average intensity of 1kW/cm^2. This intensity is high enough for many fluorescence

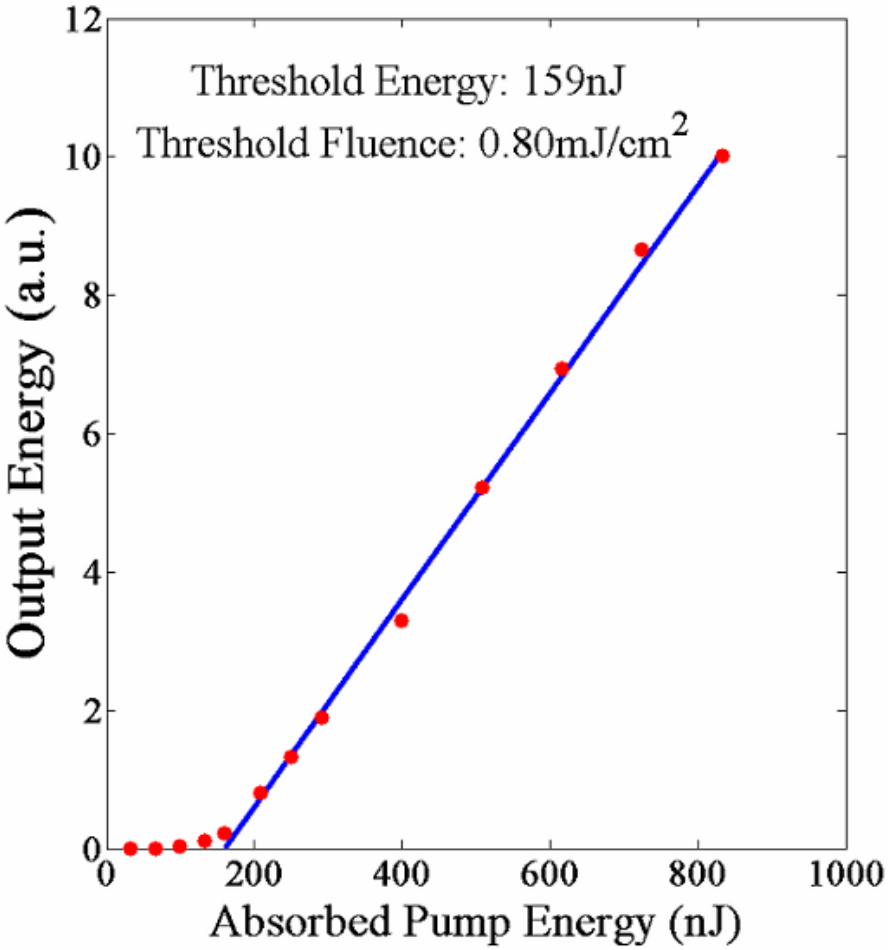

Figure 3.11: The light-out v.s. light-in curve. The threshold pump fluence is ~0.8mJ/cm^2.

and even spectroscopy applications. In addition, the current device is not designed for high power output. If higher power is desired, the transverse waveguide dimensions can be increased and a more efficient pump geometry can be used.

The elasticity of the silicone elastomer and the microfluidics compatibility of the laser chip immediately suggest two wavelength tuning mechanisms. First, the grating period is easily tunable by stretching or compressing the whole chip due to the low Young's modulus of PDMS (~750kPa)[5]. Second, the refractive index of the dye solution can be tuned by mixing two solvents with different refractive indices. For example, using methanol and dimethylsulfoxide (DMSO), the achievable refractive index change can be as large as 0.148 (1.33 for methanol versus 1.478 for DMSO). Furthermore, different dye molecules

can be used to cover an even larger spectral range. The mixing, switching and delivery of dye solutions can all be implemented on a silicone elastomer microfluidic chip using the recently developed mechanical micro valves and pumps[5].

3.5 Summary

In this chapter, we have proposed and demonstrated a phase shifted 15th order DFB structure embedded in a single mode channel waveguide as the optical cavity in an optofluidic dye laser system. Single mode operation was obtained with pump fluence from 0.8mJ/cm^2 to 8mJ/cm^2. The threshold pump intensity is within the reach of commercial high power blue laser diodes. The measured laser linewidth is less than 0.1nm. The operation of the laser chip is fully compatible with silicone elastomer based microfluidics technology[5] [6] [103]. The use of PDMS and soft lithography also results in inexpensive and easy fabrication, rapid device prototyping, biocompatibility and the opportunity to create disposable devices.

Chapter 4

Mechanically Tunable Optofluidic DFB Dye Lasers and Integrated DFB Dye Laser Arrays

One of the most attractive features of organic dye lasers is their ultra-wide wavelength tunability. In the last chapter, we have demonstrated a single frequency DFB dye laser on a PDMS chip. The natural next step is to make this laser tunable. In this chapter, we use the mechanical flexibility of PDMS elastomer materials combined with the reconfigurable nature of the liquid gain medium to demonstrate a mechanically tunable single-mode DFB dye laser with a 60nm continuous tuning range[9]. Due to the large elongation range of PDMS, the wavelength tuning range is only limited by the gain bandwidth. We also show the possibility of integrating large numbers of DFB dye lasers on a single chip [58]. As a proof of concept demonstration, we show the simultaneous operation of 13 DFB dye lasers on a chip using a single external pump.

4.1 Mechanical Wavelength Tuning

4.1.1 Wavelength Tuning of DFB Lasers

The lasing wavelength of a DFB laser can be tuned by changing either the effective index of the mode n_{eff}, the grating period Λ or the grating order m in equation (3.1), as has been demonstrated long ago in conventional DFB dye lasers [104]. The effective index n_{eff} can be varied by changing the core index or the cross sectional dimensions of the waveg-

uide. However, the low Young's modulus of PDMS (~750kPa) [5] enables a much more straight forward tuning method consisting of changing the grating period by simply stretching or compressing the elastomer chip along the waveguide direction. The wavelength tuning range is proportional to the fractional change in the grating period $d\lambda/\lambda = d\Lambda/\Lambda$. Moreover, the grating order m can be chosen by using different dye molecules whose emission spectra cover different spectral regions. The last two methods were used in this work to achieve a nearly 60nm tuning range from yellow to red. The potential tuning range for Rh6G and Rh101 is larger than 100nm covering the spectral range from 550nm to beyond 650nm (Figure 4.2). In fact, because of the multiple spectral resonances supported by the higher order grating, this laser cavity design can provide tunable output covering the entire available dye laser spectrum from 320nm to 1200nm [26] when suitable dye molecules and pump light are selected. With a mixture of several dye molecules, simultaneous multiple color lasing from the same cavity is also possible.

The fact that PDMS is a soft elastomer has been explored to make other adaptive optical elements, or the so-called elstomeric optics, in which the stretching, compressing and bending of the elstomeric material modulates the optical properties such as the period of a diffraction grating, the focal length of a lens and the curvature of a mirror [105]. The advantages of using PDMS include: 1. it can be deformed under small actuation forces due to its very low Young's modulus; 2. its elastomeric property makes the deformation reversible and repeatable without permanent distortion; 3. it can be molded at a sub-wavelength scale and with optically smooth surfaces; 4. it is biocompatible and microfluidics compatible; 5. the material and fabrication cost is low.

4.1.2 Laser Chip Design and Mechanical Tuning Setup

As shown in Figure 4.1, the optofluidic DFB dye laser structure used in this chapter is almost exactly the same as the one in Chapter 3. Slightly different channel dimensions and Bragg grating parameters were used as described below. When the microfluidic channel is subsequently filled with liquid of higher refractive index than that of PDMS, a buried channel waveguide is formed. The channel dimensions are 2μm by 3μm and the index

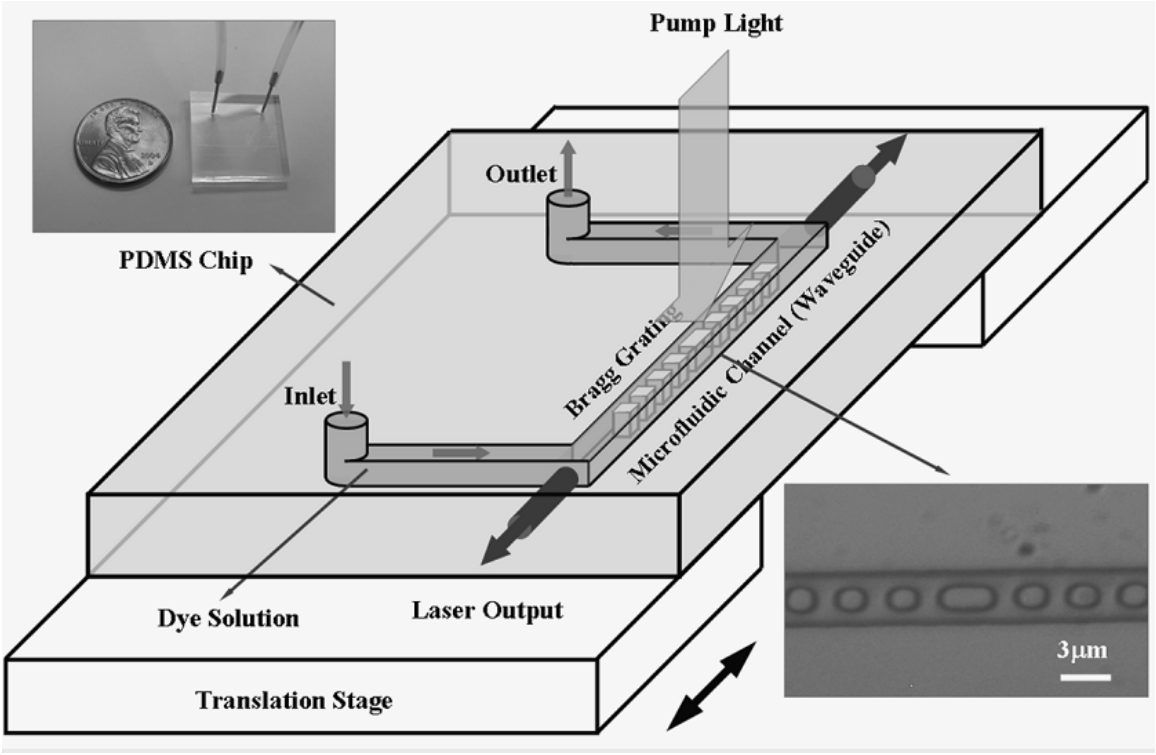

Figure 4.1: Schematic diagram of a mechanically tunable optofluidic DFB dye laser chip. The upper inset shows an actual monolithic PDMS laser chip. The lower inset is an optical micrograph of the central phase-shifted region of the laser cavity. A Bragg grating with 3080nm period is embedded in a 3 m wide microfluidic channel. The channel height is 2 m. The size of the PDMS posts is about 1.28 m 1.8 m measured from the optical micrograph. The central larger PDMS post introduces an effective /2 phase shift to ensure single wavelength lasing. The movement of the translation stage deforms the chip which causes the grating period to change.

contrast is less than 0.003 so that the waveguide supports only the fundamental spatial modes. Distributed optical feedback is provided by defining periodic PDMS posts inside the channel with a 3080nm period. The PDMS posts are 1.5μm wide and 1.8μm long. The PDMS posts together with the dye solution form a 1cm long 15th-order Bragg grating at wavelength approximately 578nm, near the gain spectrum peak of Rhodamine 6G (Rh6G). The PDMS posts are not half grating-period long so that the grating supports the even order 14th resonance that matches the gain spectrum of another longer wavelength dye modecule Rhodamine 101 (Rh101) used in this experiment. The PDMS posts also provide mechanical support, preventing the microfluidic channel from collapsing. An effective $\pi/2$ phase shift is introduced at the center of the grating to ensure single frequency operation at the Bragg wavelength. The gain medium, a 2mM solution of Rh6G or Rh101 in a methanol and ethylene glycol mixture with refractive index of 1.409, is then introduced into the flow channel to form the waveguide core. To pump the dye molecules, 6ns Q-switched Nd:YAG laser pulses with 532nm wavelength are focused through a cylindrical lens onto a $\sim$100μm by 1cm stripe aligned with the microfluidic channel. The details of the fabrication, dye chemistry, and operation of the laser chip can be found in Chapter 3.

To achieve the mechanical tuning, the laser chip was glued to two separate translation stages with the laser region suspended in the middle as shown in Figure 4.1. The movement of the translation stage deforms the chip along the waveguide direction which causes the grating period to change. The same PDMS prepolymer used in the device fabrication was also used as the clue between the chip and the stages. A 30 minutes bake at 80^{o}C is long enough to form a strong bond between the chip and the stages. The central part of the laser chip ($\sim$1cm long) was not glued to the stages, allowing the cavity to deform under stretch or compression. One of the stages is a high resolution micrometer with 1μm sensitivity which provides accurate control and quantitative measurement of the deformation of the elastomer chip. The mechanical stages allow us to both stretch and compress the chip along the channel direction, although the allowed shrinkage of RTV 615 is very limited [106].

Figure 4.2-(a) shows the simulated reflectivity spectrum of the overall structure using the Rouard's method described in Chapter 3. The parameters used are: Λ = 1280nm +

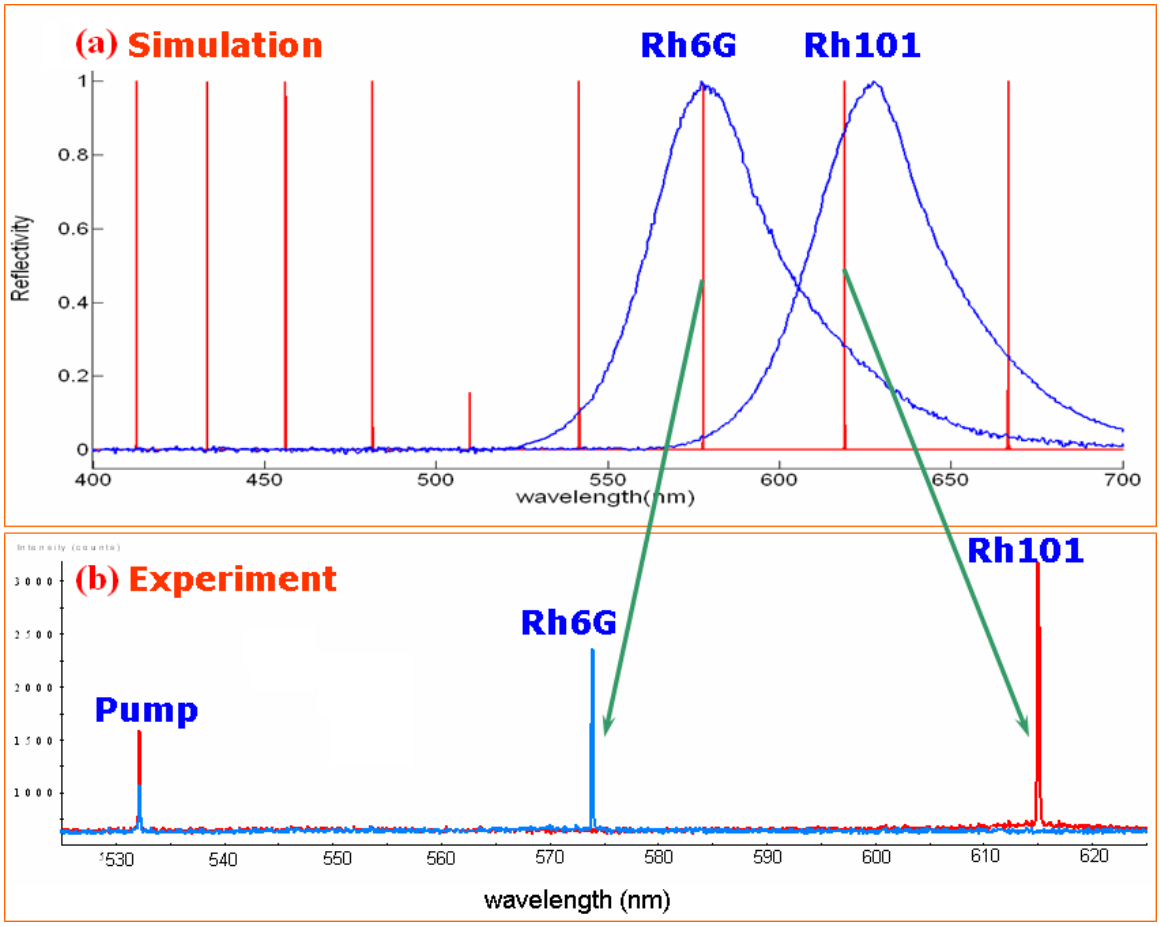

Figure 4.2: Two color lasing from the same DFB cavity. Upper: Simulated reflectivity spectrum of a $\pi/2$ phase shifted higher order DFB structure. The parameters used are given in the main text. Also shown are the normalized measured fluorescence spectra of Rh6G and Rh101 solutions used in the lasing experiment. Lower: Orange and red lasing spectra were observed when two different dye solutions Rh6G and Rh101 were subsequently introduced into the cavity.

1800nm, grating length L = 1cm, effective $\pi/2$ phase shift at the center, core index n_{core} = 1.409, and cladding/post index n_{clad} = 1.406. Also shown in Figure 4.2-(a) are the normalized measured fluorescence spectra of Rh6G and Rh101 solutions used in the lasing experiment. According to the simulation, the structure has its 14th and 15th resonances at 577.8nm and 612nm respectively. The Bragg wavelengths were chosen to match the gain peaks of Rh6G and Rh101. The free spectral range (FSR) is about 40nm, which is large enough to ensure that at most two resonances can be simultaneously supported within the gain spectrum (typically 30-50nm wide for dye molecules). Thus single frequency operation is obtained even at high pump levels due to the large gain discrimination.

4.1.3 Two Color Lasing and Mechanical Tuning Results

When the same laser cavity was subsequently filled with Rh6G and Rh101 dye solutions, we observed single mode lasing for each solution, as shown in Figure 4.2-(b). This verified our prediction in the previous chapter that the 15th order DFB structure can support multiple color single frequency lasing when different dyes are used. Due to the lack of suitable pump sources, we haven't demonstrated laser actions in shorter wavelengths below 550nm. However, we believe if a blue or UV pulsed pump source is used, such as a pulsed N_2 laser, an excimer laser, or a flash lamp, we can achieve all color lasing across the whole visible spectrum from this same DFB cavity since literally hundreds of different laser dyes are available to cover this spectral range[107].

The experimental results of mechanical cavity tuning are summarized in Figure 4.3. The points on this Figure represent experimental data whereas the curves follow the linear fit. From this plot, the single mode tuning range for Rh6G covers a range from 565nm to 594nm whereas for Rh101, the tuning range extends from 613nm to 638nm. A linear relationship between the lasing wavelength and the chip deformation was also observed in Figure 4.4, indicating completely reversible elastic extension of the cavity. When the length of the central suspended region is 1cm, the total chip deformation required to traverse the above tuning ranges are about 500 μm for Rh6G and 400 μm for Rh101. These macroscopic deformations correspond to 28nm and 25nm distortions of the grating period, respectively.

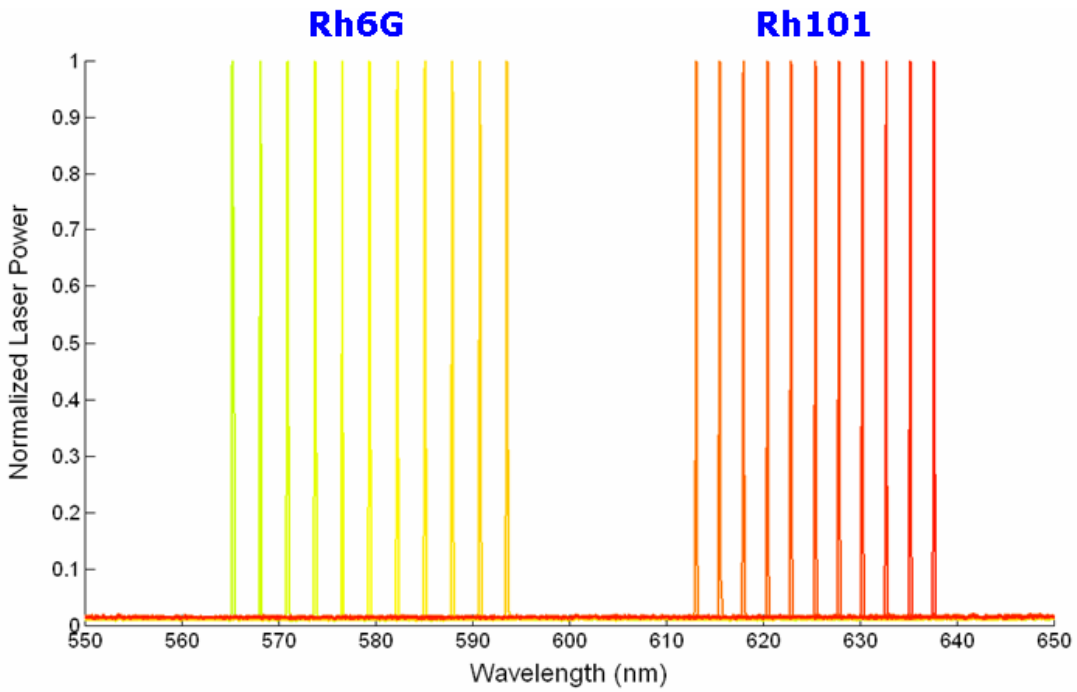

Figure 4.3: Normalized laser output of the mechanically tunable optofluidic DFB dye laser. Different peaks correspond to different grating periods. The measured laser linewidth is less than 0.1nm throughout the tuning range.

Because of the extremely large available elastic deformation of PDMS of over 120%, the ultimate tuning range is limited by the gain bandwidth of the laser dyes chosen. Only ~5% deformation was used to achieve the ~60nm tuning range demonstrated in this experiment, and we believe that an even wider tuning range from 550nm to 650nm is obtainable with improved cavity design and a more uniform mechanical loading. The tuning is continuous and completely reversible, and no noticeable degradation of the chip was observed during a 100-cycle full range tuning test. Throughout the tuning range, stable single-mode operation was maintained with measured linewidth below 0.1nm, the resolution limited by our spectrometer (Ocean Optics HR4000). The absorbed pump thresholds of this tunable dye laser are ~150nJ and ~200nJ for Rh6G and Rh101 respectively. As expected, we observe a decrease in the laser output power as the lasing wavelength is moved away from the peak of the gain spectrum in either direction. The deformation along the channel also causes the transverse waveguide dimensions to change slightly, resulting in changes of the effective

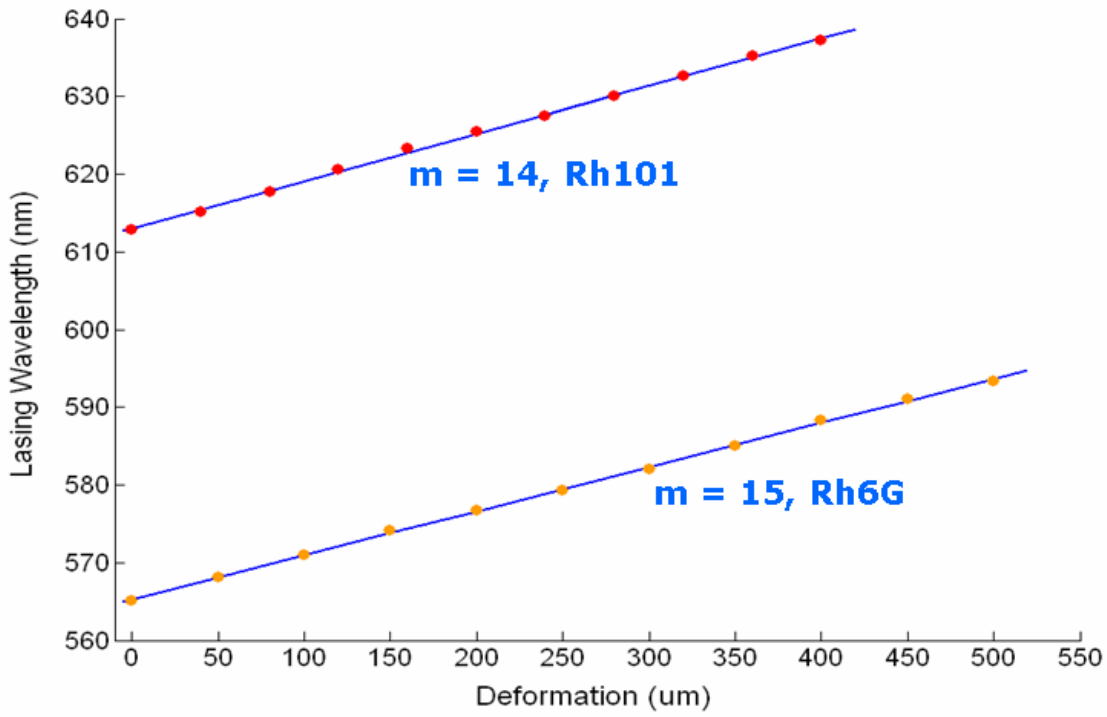

Figure 4.4: Lasing wavelength versus the measured chip deformation. The points are the experimental data and the curve is the linear fit. The achieved single mode tuning range for Rh6G is from 565nm to 594nm and is from 613nm to 638nm for Rh101.

index of the guided mode. However, given that the Poisson's ratio of PDMS is approximately 0.5, the estimated effective index change is only about 1.5×10^{-5}, thus the effect of lateral waveguide distortion on the lasing wavelength is negligible.

In some cases, the transverse loading geometry may be more preferred, in which the deformation force is applied transverse to the channel. Since PDMS is almost a perfectly incompressible material with Poisson's ratio ~0.5, the transverse strain can be efficiently translated to longitudinal strain. We have also implemented elastic tuning using a transverse load and achieved a ~10nm tuning range for each dye mentioned above. For the same wavelength tuning range, the transverse deformation of the waveguide is 4 times larger in the transverse loading geometry than in the longitudinal loading. Therefore the contributions from the effective index change on the wavelength tuning is expected to be larger.

4.2 Integrated DFB Laser Array

4.2.1 Fabrication and Initial Demonstration

We also fabricated an array of five DFB dye lasers on a single PDMS chip. Figure 4.5 shows the measured lasing spectra from this DFB array after filling the lasers with the Rh6G dye solution. Each laser was pumped individually and the combined lasing spectrum was shown in Figure 4.5. Lasers with output wavelengths spanning a ~15nm range were measured from the DFB stripes with different grating periods. The low pump threshold (< 1uJ) of each optofluidic DFB dye laser makes it possible to use a single high energy pulsed laser to pump hundreds of such lasers on a chip. This opens up the possibility of building highly parallel multiplexed biosensors on a chip with applications ranging from multiple-color flow cytometers and surface plasmon resonance based sensors to Raman spectroscopy sources and compact excitation spectroscopy systems. The introduction of replica molded multi-spectral sources in PDMS fluidic systems also provides an alternative to tunable lasers for constructing compact and inexpensive multi-wavelength scanning-less spectrometers integrated in microfluidic devices [108].

A unique feature of soft lithography is the capability to bond multiple patterned thin films of elastomer to build multilayer structures. Typically, a thick layer with the top structure is prepared as previously described. Each following thin layer of PDMS is spin-coated onto the mold with a typical thickness of ~30μm and baked at 80^{o}C for 20 minutes. The growing thick layer is then assembled onto each new thin layer and bonded by oxygen plasma treatment and baking at 80^{o}C for 20 minutes. Seven-layer devices have been reported and no obvious limitations exist to limit the number of layers [5]. We have used this method to fabricate a three-layer DFB laser device with 10 lasers in each layer. Figure 4.6 shows the optical microscope image of a two-layer DFB laser array. The slight misalignment between the two layers was deliberately introduced to make more efficient use of the total pump area. With multilayer devices, each layer can perform different functions so that the integration level and the compactness of the device can be greatly improved.

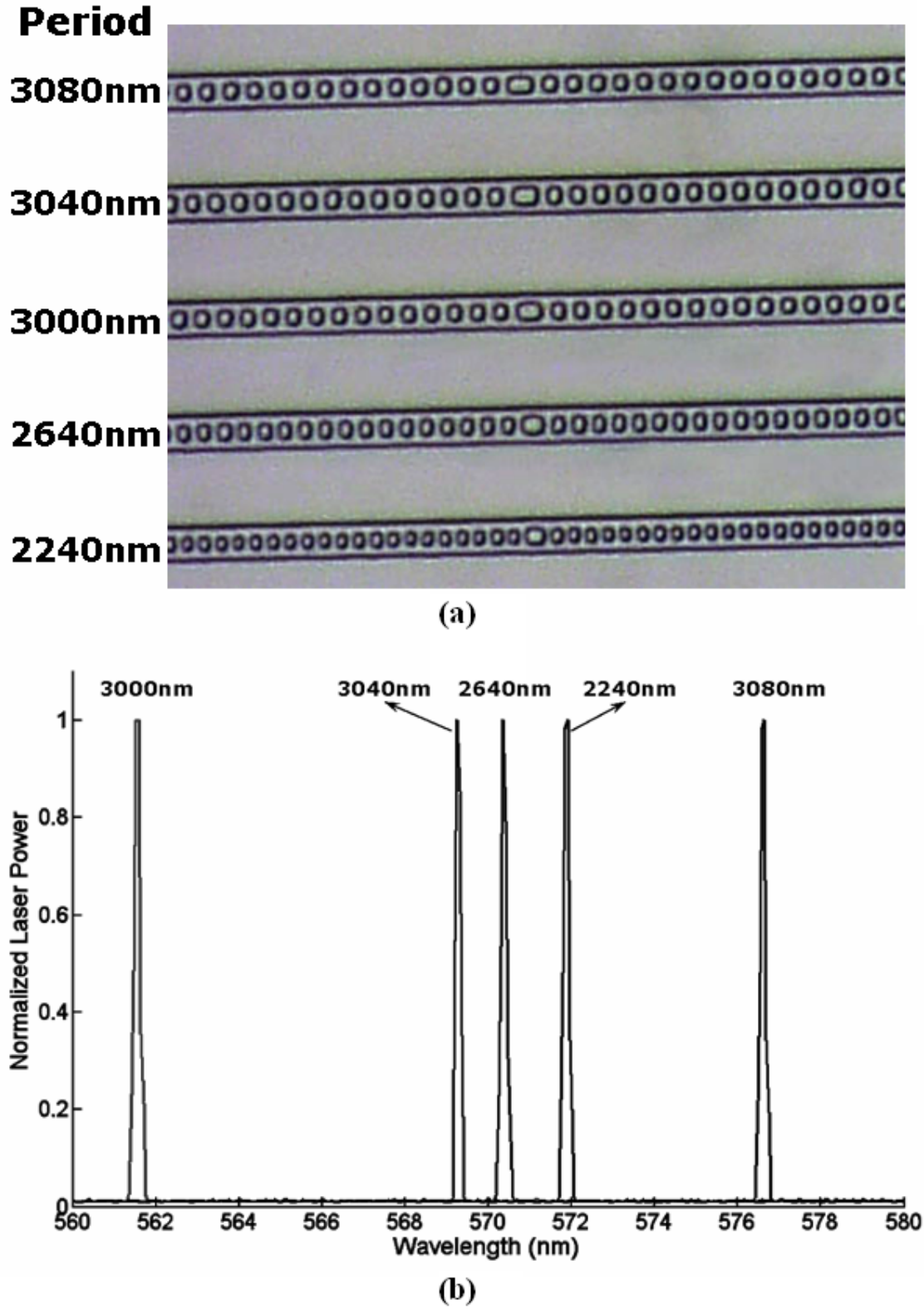

Figure 4.5: (a): Optical micrograph of an integrated array of five optofluidic DFB dye lasers. The grating period of each laser is given on the left. (b): normalized laser output of the array using Rh6G dye solution as the gain medium.

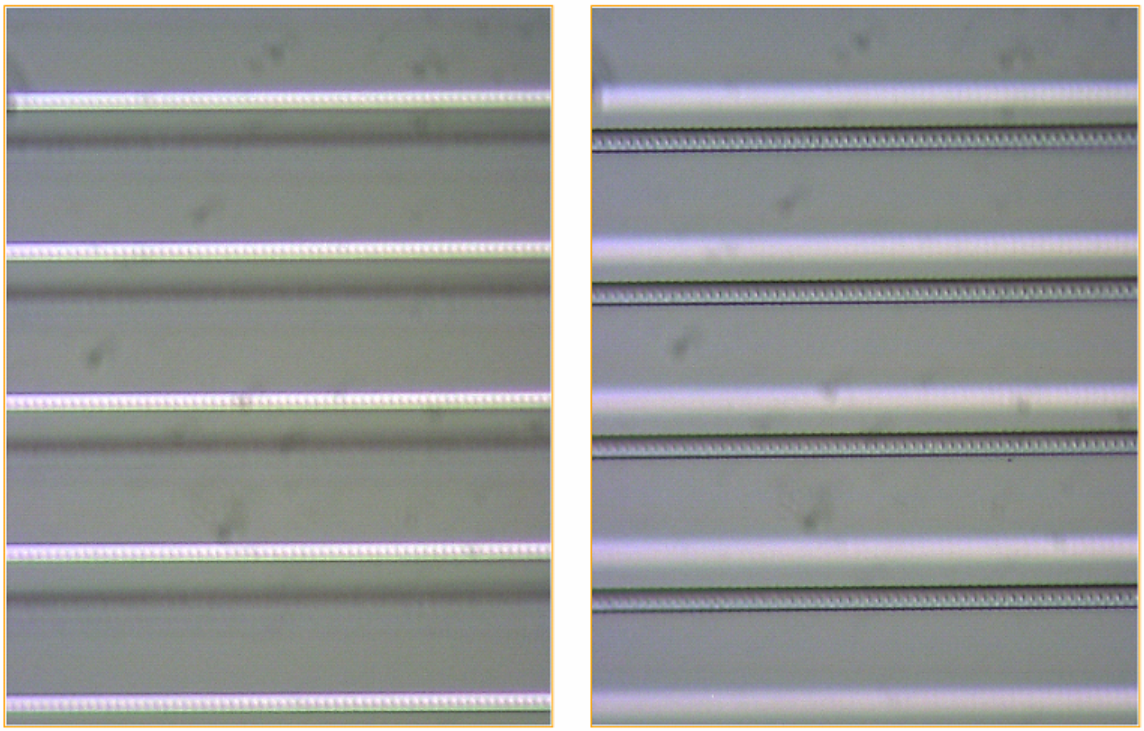

Figure 4.6: Vertical stacking of optofluidic DFB laser arrays using multi-layer soft lithography. Left: upper laser array is in focus. Right: bottom laser array is in focus.

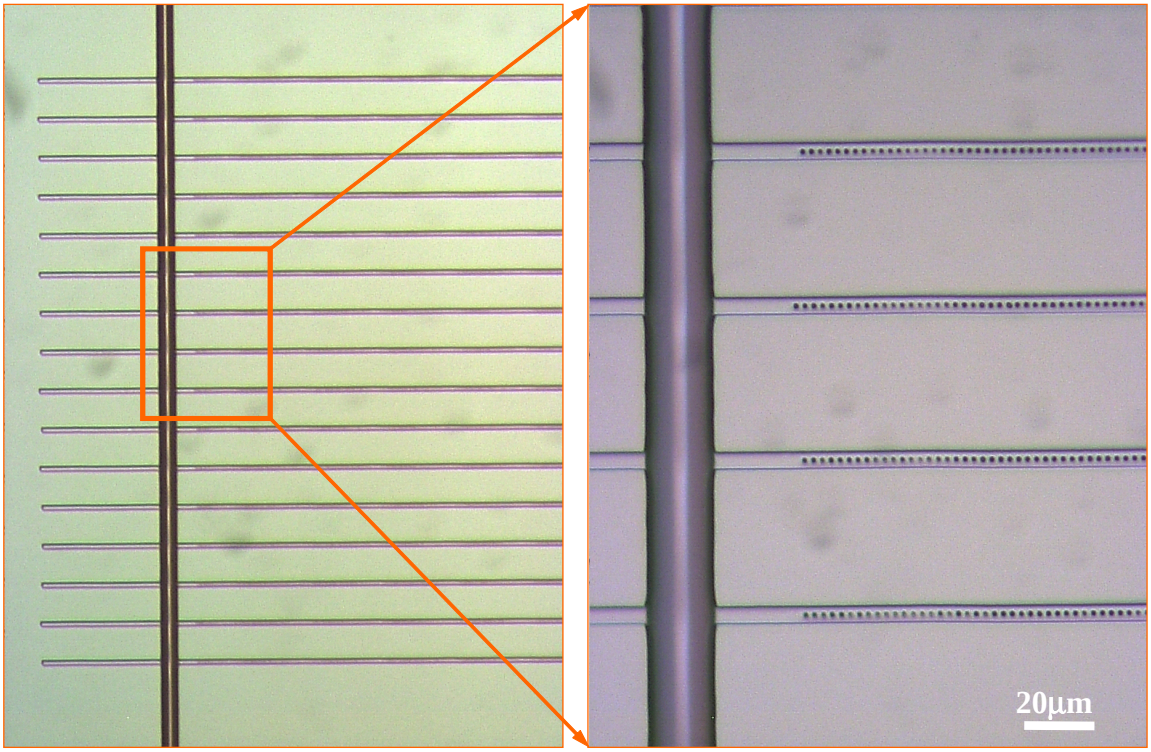

Figure 4.7: Optical micrograph of an array of 16 DFB dye laser cavities connected to the input liquid channel in PDMS. The lasing wavelengths are designed to operate from 565nm to 640nm with 5nm spacing. The waveguide dimensions are 4μm wide and 2μm high. The PDMS posts are 2μm wide and half grating-period long.

4.2.2 Simultaneous Operation of Thirteen DFB Lasers On a Single Chip

Although we can achieve individual single mode lasing, the DFB lasers in the integrated array shown in Section 4.2 could not be operated simultaneously. One possible reason is that the spatial separations between adjacent waveguides are so small that lasing modes can interact with each other and give rise to complex output behaviors. To demonstrate the parallel operation of laser arrays, we fabricated an array of 16 DFB dye lasers with the spatial separation 10 times the waveguide width to avoid coupling. The waveguide dimensions of the lasers were 2μm high, 4μm wide and 8mm long, thus the spatial separation was chosen to be 40μm between adjacent waveguides. The final PDMS device is shown in Figure 4.7. The grating periods are chosen so that the designed lasing wavelengths span from 565nm to

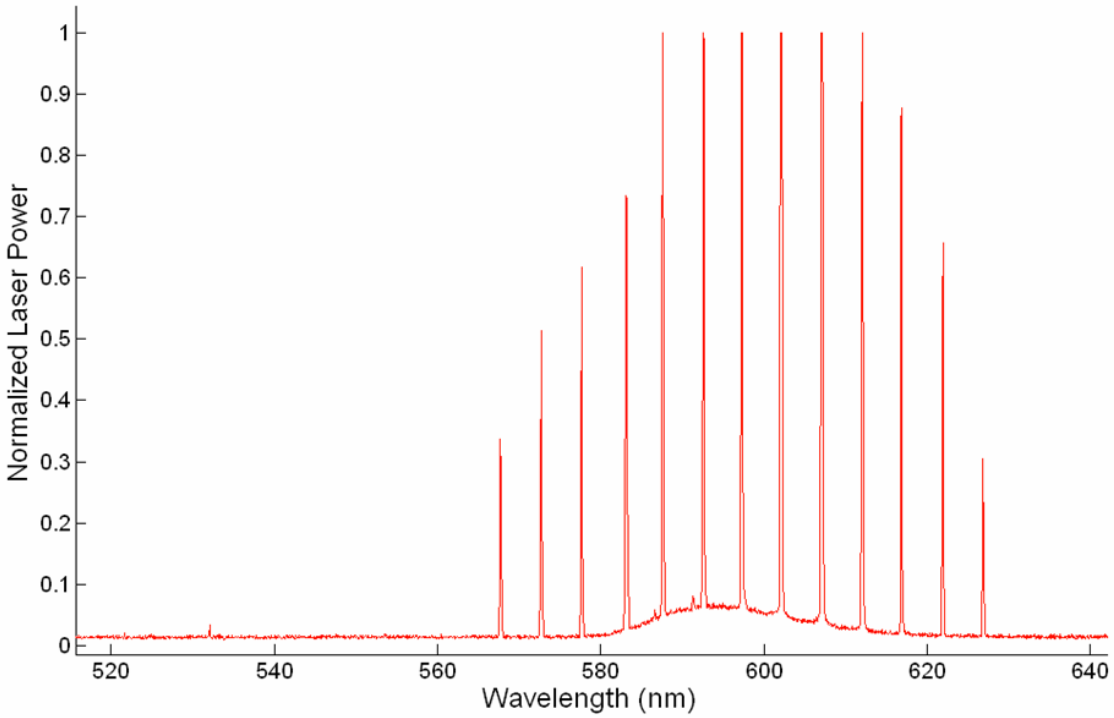

Figure 4.8: Simultaneous lasing spectrum of the 16 DFB laser array. 13 lasers operated above the thresholds. The wavelength spacing was ~4.94nm due to the PDMS shrinkage. The middle 6 laser lines saturated the detector.

640nm, all within the gain spectrum of Rh6G. The designed wavelength spacing between adjacent lasers is 5nm.

The total area of the laser array is about 1.3mm by 8mm. We used 6ns Q-switched Nd:YAG laser pulses at 532nm to pump this whole area. Figure 4.8 shows the simultaneous lasing spectrum from the DFB laser array at the pump level of ~3mJ/cm^2. Further increase in pump power to above ~6mJ/cm^2 caused liquid evaporation and eventually damaged the chip due to the poor heat conductivity of PDMS. Out of the 16 lasers, 13 achieved lasing and all operated in the single mode regime. The real lasing wavelengths were shifted from the designed ones due to the PDMS shrinkage after curing. The wavelength shifts were different for each lasers, but all around 4.9nm. This corresponds to about 2% shrinkage of the dimensions from the designed values.

This experiment demonstrated the potential of integrating many DFB dye lases on a single chip with a single external pump. Clearly, shorter laser cavities using first order

gratings and smaller waveguides will allow much higher integration density. Using the vertical integration scheme shown above, more efficient use of the pump light and even higher level of integration can be achieved. Such simultaneously operated integrated laser arrays can find applications in digital scanning-less spectroscopy and multiplexed sensing applications such as surface plasmon resonance (SPR) sensors and multiple color flow cytometry.

4.3 Summary

We have demonstrated a continuously tunable optofluidic DFB dye laser on a monolithic PDMS chip that uses simple mechanical deformation for accurate wavelength control. Single-mode operation was maintained throughout a ~60nm tuning range. Due to the higher order of the DFB grating in our devices, a single laser is capable of generating tunable output covering the spectral region from near ultra-violet to near infrared when a UV pump source is used. Integrated multi-spectral DFB laser arrays were also demonstrated by replica molding. Vertical integration was achieved using multi-layer soft lithography. With a single pump source, we achieved simultaneous operation of 13 DFB lasers on a single chip. Such laser arrays can be used to make highly parallel multiplexed biosensors and scanning-less spectrometers on a chip [108]. It is important to note that these lasers are still not stand-alone devices because an external gas pressure source is still required to actuate the microfluidic valves, and an external pump laser is required to pump the dye. The gas pressure source can be eliminated by using electrokinetically driven flow, whereas an external pump light will continue to be necessary for our dye laser designs. For portable and inexpensive devices, visible semiconductor lasers or bright LEDs can be used as the pump source.

Chapter 5

Microfluidic Tuning of Optofluidic DFB Dye Lasers

In the previous discussions, we have emphasized the compatibility of our laser devices with PDMS soft microfluidics. This compatibility suggests another fully integrated microfluidics-based wavelength tuning method. The refractive index of the dye solution can be tuned by mixing two solvents with different refractive indices. For example, using methanol and DMSO, the achievable refractive index change can be as large as 0.148 (1.33 for methanol versus 1.478 for DMSO). Furthermore, as demonstrated earlier, different dye molecules can be used to cover an even larger spectral range. The mixing, switching and transport of dye solutions can all be implemented on a PDMS elastomer chip using the recently developed mechanical micro valves and pumps [5][103]. More generally, the integration of fluidic and optical functions on the same chip is a powerful enabling technique for building adaptive optical devices and more complete "lab-on-a-chip" systems.

5.1 Monolithic Integration with PDMS based Microfluidic Tuning Circuits

5.1.1 Microfluidic Tuning Circuits

A fully integrated microfluidic tunable DFB dye laser based on multilayer soft lithography is obtained by integrating a microfluidic mixing circuit with the DFB laser cavity.

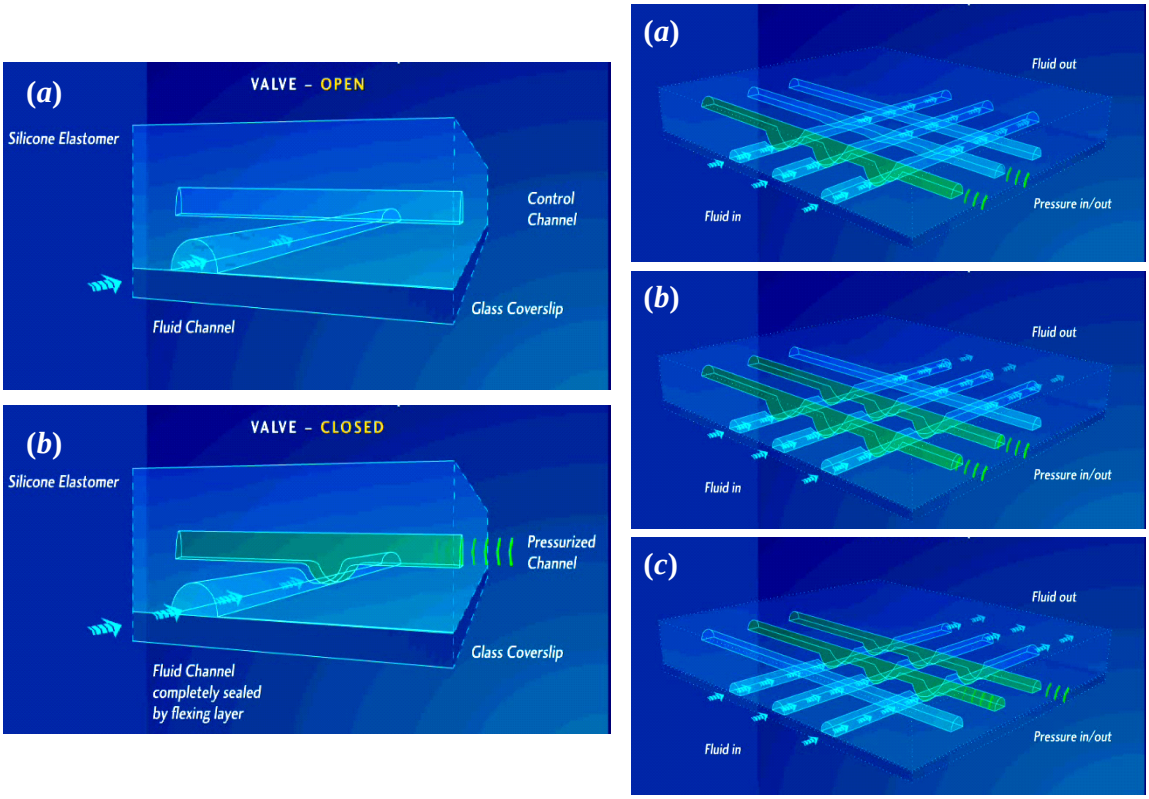

Figure 5.1: PDMS micro mechanical valve and peristaltic pump (push-down version). Left: operation of the valve. Right: operation of the peristaltic pump. Source: www.fluidigm.com

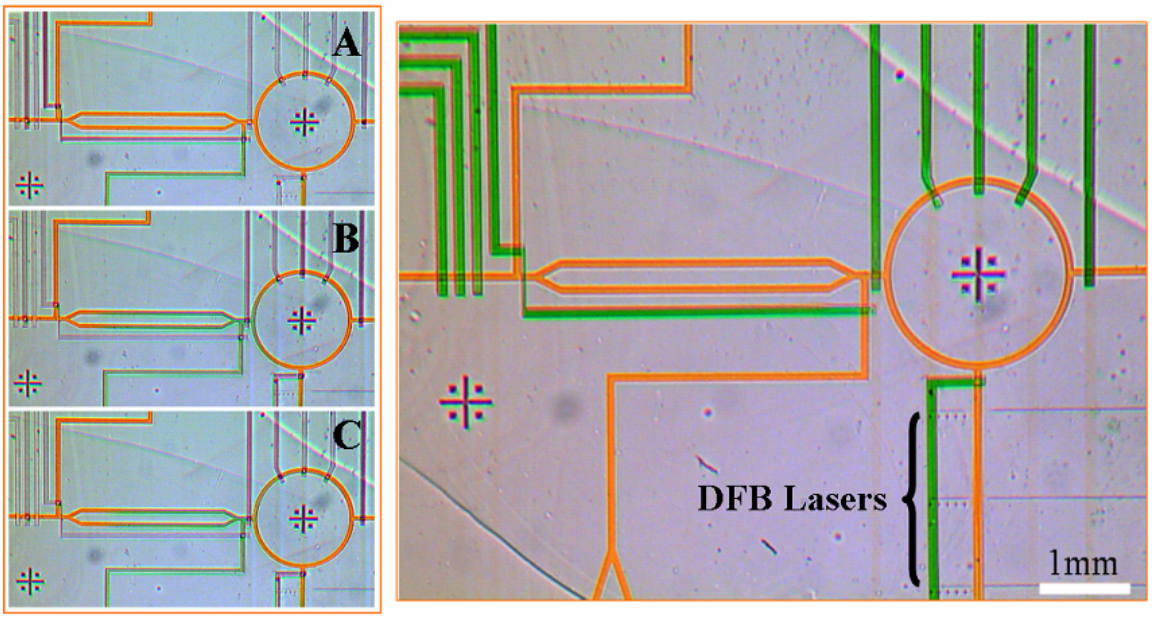

Figure 5.2: Integration of a high resolution microfluidic dispenser and a rotary mixer with DFB dye lasers. Left: Different stages of the microfluidic mixing. A. the rotary mixer is filled with orange dye solution; B. an accurate amount of green dye solution is delivered into the mixer; C. the pneumatic pump mixes the two solutions. Right: Optical micrograph of a monolithic PDMS device in which a microfluidic mixing circuit is integrated with an array of optofluidic DFB dye lasers.

Figure 5.2 shows an automated high resolution microfluidic dispenser and a rotary mixer integrated with an array of 5th order DFB dye lasers. The lower green channels (dead-ended channels) are the control lines and the upper orange layer is the fluid layer. The crossing areas between the control lines and the fluidic channels formed the active micro mechanical valves which can be closed by applying pressure in the control channels which mechanically deforms the membranes between the control and fluidic layers and closes the rounded fluidic channel. Three consecutive valves on a single fluidic channel can form a peristaltic pump [5]. The operations of the valves and pumps are shown in Figure 5.1. Figure 5.1 shows the push-down version, whereas we used the push-up valve structures which requires smaller actuation forces. The invention of such on-chip micro mechanical valves and pumps has enabled very sophisticated liquid manipulation [7] and large scale integration [6] in PDMS microfluidic devices. The detailed operation of the dispenser and the mixer can be found in reference [103]. In short, accurate amount of two different dye solutions can be delivered into the mixer and get mixed uniformly before entering the laser cavities. Three stages of the microfluidic mixing are shown in Figure 5.2. First, the ring-shaped rotary mixer was filled with the first dye solution (orange). In the laser tuning experiment, this dye solution was a 1mM Rh6G in methanol. Then, an accurate amount of the other dye solution (green) (a 1mM Rh6G in DMSO in the real tuning experiment) was delivered into the mixer through the high resolution dispenser to the left of the ring mixer. The pneumatic pump made of three pushed-up valves mixed the two solutions uniformly. Finally the valve separating the mixer and the laser cavities was opened and the mixed dye solution was pumped into the laser cavities. All these manipulations can be computer controlled through a PCI card connected to a solenoid pressure valve array whose valves are connected to the control channels on the chip through small plastic tubings.

Any adaptive device can be thought of as a sensor if the adaptation is due to some variations one wishes to characterize. Therefor the fluidically tunable DFB dye laser can be used as an active sensor to detect small refractive index or absorption changes in the liquid gain medium due to the presence of small amounts of certain analytes. The fluidic tuning can be also used to build tunable filters for fluorescence detection and spectroscopy applications. In many cases, fluidic tuning is preferred over solid state material based meth-

ods due to its reconfigurable nature, higher index contrast dn/n, thermal stabilization, self healing, optically smooth interfaces, ability of introducing active optical elements such as fluorescent dyes, metallic nanoparticles and quantum dots, ability of generating gradients in optical properties and the intrinsic compatibility with liquid phase biological and chemical reactions [8].

5.1.2 Fabrication

The fabrication process for the laser structures is the same as given in Chapter 3. The two-layered microfluidic circuits were fabricated by multilayer soft lithography developed by Steven Quake's group and Axel Scherer's group at Caltech [5] [103]. The master molds for the fluidic layer and control layer were patterned SPR220-7 photoresist on two separate Si wafers fabricated by conventional photolithography. We used a pushed-up valve structure to control the liquid flow due to its smaller actuation force than a pushed-down valve structure [109]. To monolithically integrate the DFB dye lasers with the microfluidic circuits, the SU8 laser mold was fabricated on the same silicon wafer as the fluidic layer mold using a double-exposure photolithography process. Therefore, the replica molded PDMS fluidic layer contains both the laser structures and the microfluidic channels. The whole process requires multiple photolithography steps. Also the accurate alignment between the two layers is important for the proper operation of the device. The detailed fabrication recipe is given in Appendix A.

5.2 Experimental Results of Microfluidic Wavelength Tuning

5.2.1 15th Order DFB Dye Laser

The waveguide structures used in previous two chapters are not suitable for fluidic tuning, because the relative large dimensions of the waveguide cause multiple transverse mode operation when the index contrast is increased to slightly above 0.003. Figure 5.3

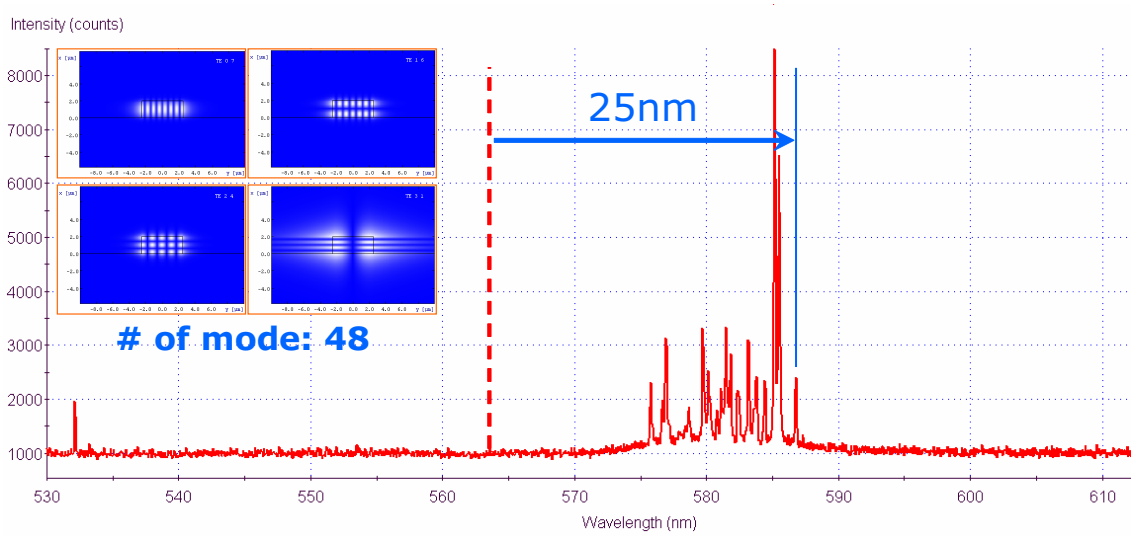

Figure 5.3: Lasing spectrum of the 15th order optofluidic DFB dye laser with high index contrast between the liquid core and the PDMS cladding. The waveguide dimensions are 2μm by 5μm. The grating period is 3μm. The refractive index of the Rh6G dye solution is 1.478 in DMSO. More than 20 lasing modes were observed. The inset shows four simulated TE-like transverse mode profiles.

shows a measured lasing spectrum of the DFB laser structure used in Chapter 3 when a high refractive index dye solution was used. In this case, the gain medium was a solution of 2mM Rh6G in DMSO which has a refractive index of 1.478. In this experiment, the waveguide dimensions were 2 μm by 5μm and the grating period was 3μm. More than 20 lasing lines were observed in the spectrum. Finite element simulation showed the waveguide supports totally 48 transverse modes. The measured longest lasing wavelength was 587nm, close to the predicted 588nm for the lowest TE_{00} mode, which had moved by ~25nm to longer wavelength compared with the case when the core index is 1.409. To avoid multiple transverse mode operation during fluidic tuning, smaller waveguide (channel) dimensions have to be used.

5.2.2 5th Order DFB Dye Laser

We have fabricated a PDMS channel of transverse dimensions 250nm by 880nm with an embedded 5th order Bragg grating, using a Si master mold fabricated by Ebeam lithog-

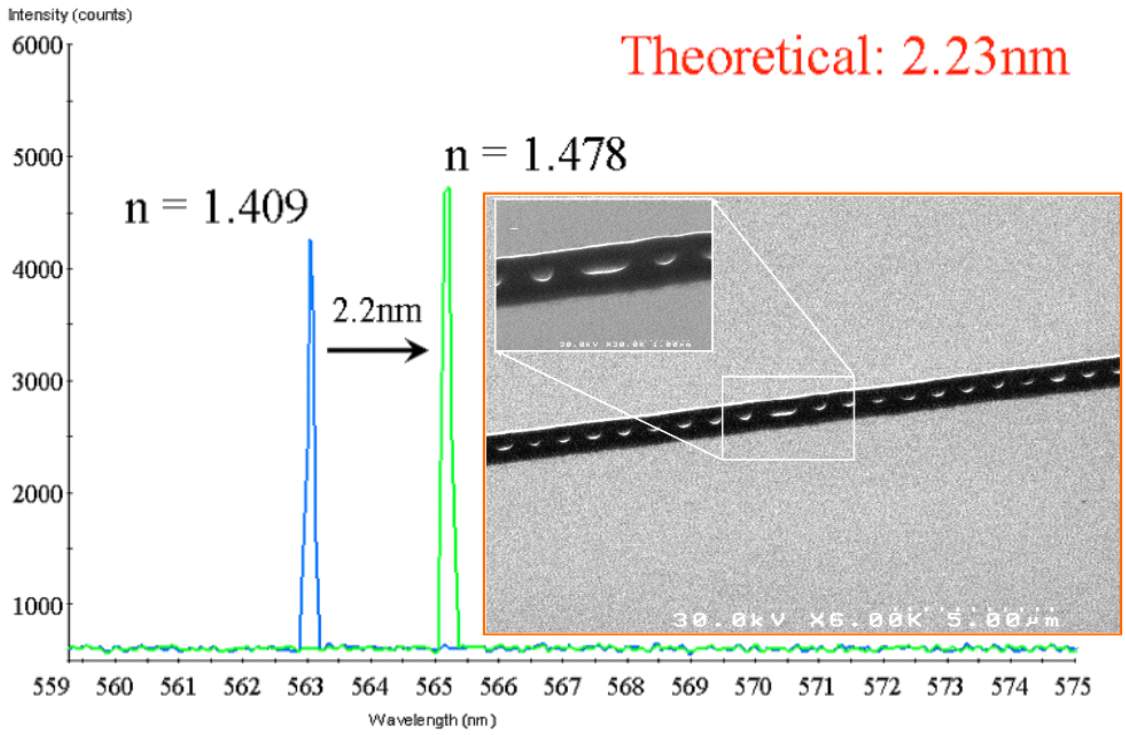

Figure 5.4: Fluidic tuning of a 5th order DFB dye laser with waveguide core dimensions 250nm by 880nm. The inset shows a scanning electron micrograph of the silicon mold. The grating period is 1μm.

raphy (EBL) and reactive ion etching (RIE). The laser cavity is 4mm long. The inset of Figure 5.4 shows a scanning electron micrograph (SEM) of the master mold. This waveguide remains single mode throughout the index range from 1.406 to 1.478, which gives a predicted 2.23nm single mode tuning range. The experimental lasing results matched the theoretical values almost exactly as shown in Figure 5.4.

The small tuning range is due to the small depth of the waveguide. The size of the guided mode is about 0.6μm×1μm which is considerably larger than the size of the waveguide core. In this case, a large portion of the waveguide mode resides outside the waveguide core. Therefore, even a relatively large index change in the core results in only a small change in the effective index. The optimized waveguide geometry for large single mode tuning range will be considered in the next section. Although this range is small compared to that of elastic tuning and the available gain bandwidth, better waveguide design and techniques such as Vernier effect [110] can be used to fully utilize the wide gain bandwidth of dye molecules.

Note the small sizes of the 5th order DFB lasers resulted in extremely small consumptions of dye solution. Only two picoliter dye solution is needed to fill each laser cavity. The pump threshold energy was also reduced to only ~30nJ due to the small size. With this cavity size, much higher integration densities can be achieved than those demonstrated in Chapter 4.

5.3 Optimum Cavity Structure for Microfluidic Tuning

The wavelength tuning range by index modification is given by the fractional change in the effective index of the guided mode

$$\frac{\Delta\lambda}{\lambda} = \frac{\Delta n_{eff}}{n_g} = \Gamma\frac{\Delta n}{n_g} \tag{5.1}$$

where Γ is the confinement factor (the fraction of mode energy inside the core), Δn is the real refractive index change of the core, and n_g is the group velocity of the mode. The larger the effective index change, the larger the tuning range. It appears then we should use

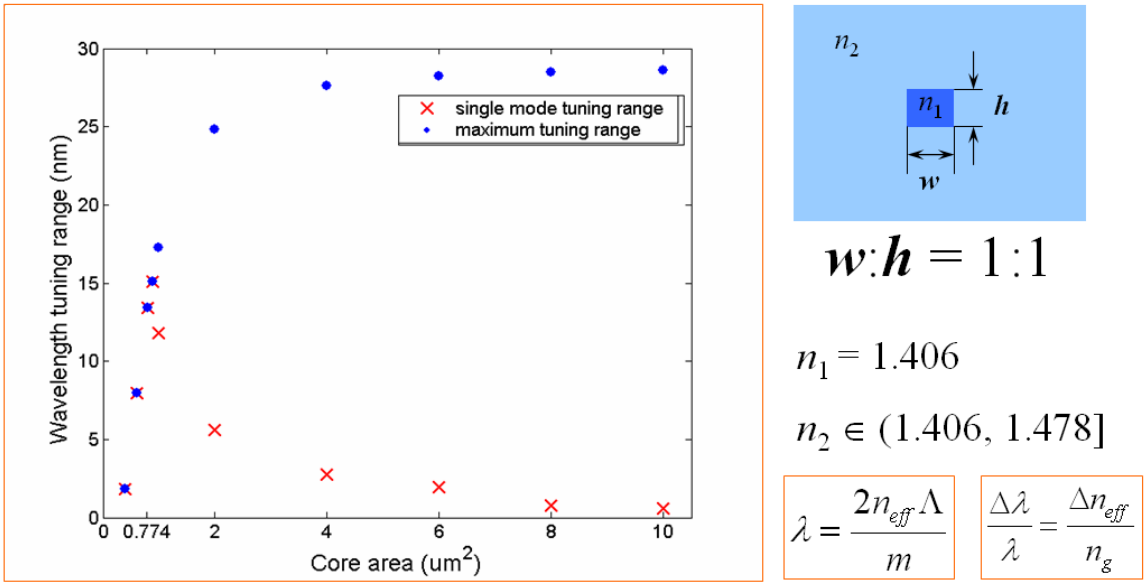

Figure 5.5: Optimum waveguide dimensions for maximum single mode wavelength tuning range by fluidic index tuning. The maximum single mode tuning range of ~ 15nm is achieved with core dimensions 880nm by 880nm for core index change from 1.406 to 1.478.

a large waveguide core so that the real refractive index change gets efficiently translated to the effective index change due to the large Γ. However, when the waveguide core is large, it leads inevitably to multiple transverse mode operation. Therefore, to maintain single spatial mode operation, the allowed index change of the core is limited by a maximum value determined by the waveguide dimensions. Above a certain core size, the single mode tuning range starts to drop with further increases in the core dimensions. Therefore there exists an optimum core size that allows the maximum single spatial mode wavelength tuning range. We used FEM simulation (Comsol FEMLAB 3.2) to find this optimum size while fixing the aspect ratio (width/height) of the core to be 1:1. The simulation results are given in Figure 5.5. The blue dots are the maximum wavelength tuning ranges (corresponding to the fundamental transverse mode) for the given core sizes, while the red x's are the maximum single mode tuning ranges. The largest single mode tuning range is obtained when the core dimensions are 880nm by 880nm and the core index is changed from 1.406 (PDMS) to 1.478 (DMSO).

As for the longitudinal mode control, for the optimum waveguide core dimensions ob-

tained above, we can fabricate either a 5th-order Bragg grating as PDMS posts in the middle of the core, or a 1th-order Bragg grating on the two sidewalls of the core (Figure 5.6). The required feature sizes can only be obtained with advanced nanofabrication tools such as E-beam lithography (EBL) and Focused Ion Beam (FIB) milling. We have successfully fabricated 1th-order sidewall Bragg gratings in Si with 100nm features using EBL as shown in Figure 5.6. However the dry etching to a depth of 880nm has proved to be a more

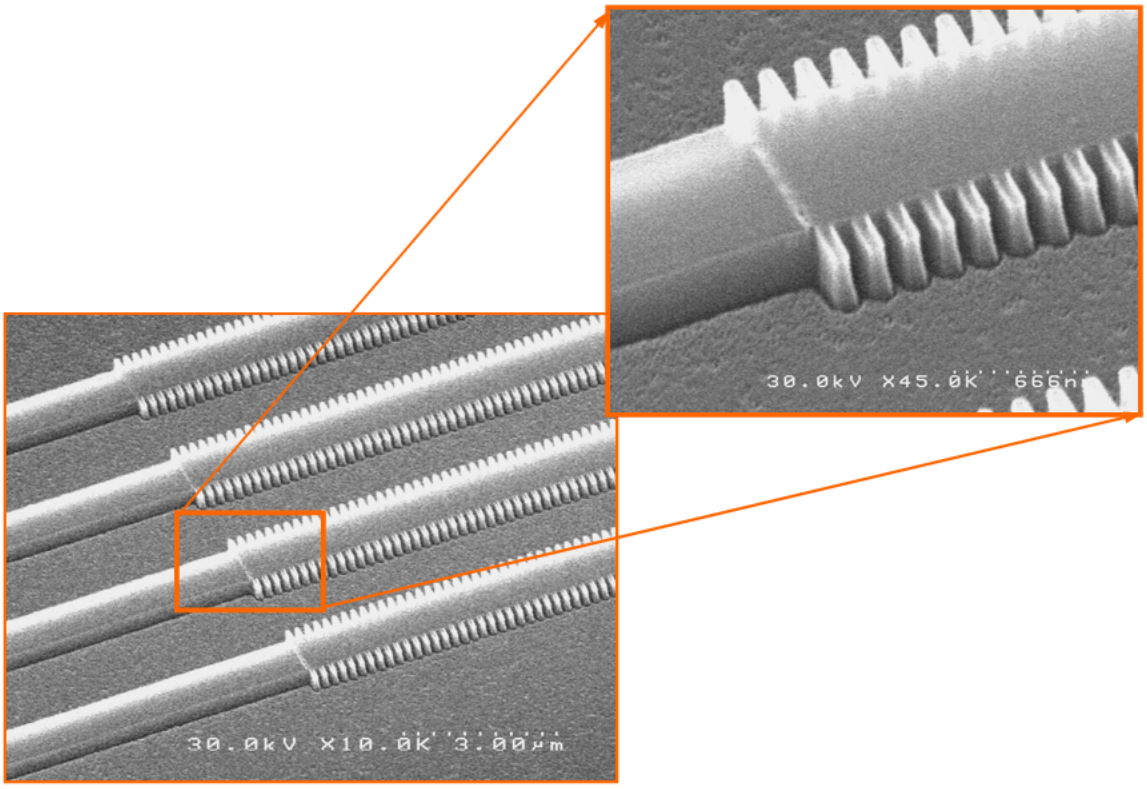

Figure 5.6: Si mold for the 1st-order DFB optofluidic dye laser fabricated by Ebeam lithography (EBL) and reactive ion etching (RIE).

challenging task. The etching recipe we used only allowed the maximum etching depth of ~250nm into Si. This is the main reason why we haven't achieved 15nm tuning range predicted by the simulation. However, people have demonstrated micron scale etching depth in Si, thus improvements in the etching step should allow us to achieve larger fluidic tuning ranges in the future.

5.4 Summary

In this chapter, we showed that optofluidic DFB dye lasers can be monolithically integrated with PDMS based soft microfluidics. This feature is crucial for future fully integrated "lab-on-a-chip" applications. Automated microfluidic wavelength tuning was achieved by accurately mixing two solvents methanol and DMSO on chip to change the refractive index of the waveguide core. Experimental results with both the 15th order and 5th order DFB structures matched the theoretical predictions well. We also used FEM simulations to investigate the optimum cavity structure for microfluidic wavelength while maintaining single mode operation. A maximum single mode tuning range of 15nm can be obtained with the waveguide dimensions 880nm by 880nm if the core index is changed from 1.406 to 1.478.

Chapter 6

Optofluidic Microring Dye Lasers

Owing to their high quality (Q)-factors and small sizes, microring resonators have attracted attentions for numerous applications such as lasers, filters, modulators and sensors [39]. In particular, ultralow threshold lasers have been made using microring-like cavities [39]. In the context of "lab-on-a-chip" applications, microring structures may enable the implementation of low threshold liquid dye lasers on a microfluidic chip which can be pumped by a laser diode or a high power LED to make fully integrated devices. In the previous chapters, we have demonstrated DFB liquid dye lasers on monolithic PDMS devices using a soft lithographic replica molding method. Here we show the same fabrication process and material system can be used to make microring liquid dye lasers which can be monolithically integrated with PDMS microfluidics and the required pump threshold power is within the reach of commercial visible laser diodes. This is, to our knowledge, the first integrated optical microring liquid dye laser ever demonstrated.

6.1 Accidental Beginning

Our work on optofluidic microring lasers accidentally started while we were working on the microfluidic tuning of DFB dye lasers. Recall that the microfluidic circuits we used to fluidically tune the lasing wavelength included a ring shaped fluidic mixer, as shown in Figure 6.1 and Figure 5.2. When the pump light was focused onto a small portion of the ring, shaded area in Figure 6.1, we observed a clear multi-mode lasing spectrum above certain pump level due to the ring-shaped resonator. Lasing only occurred at the long

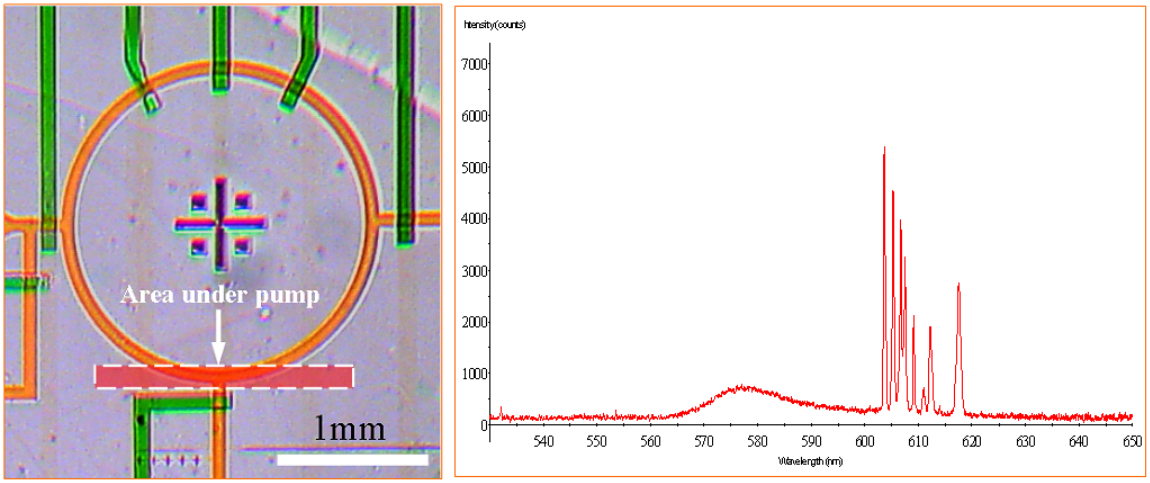

Figure 6.1: Optofluidic microring dye laser. Left: a liquid core microring resonator initially used as a microfluidic mixer. The ring radius is 1 mm and the channel width is 80 m. The shaded area inside the dashed box is the area that is under pump light. Right: a typical lasing spectrum of the ring dye laser.

wavelength tail of the gain spectrum because only a small portion of the ring was pumped and the large self absorption along the ring prevented lasing in the short wavelength region. It was quite fun to see the whole ring light up and change color to red when the laser threshold was reached.

6.2 Single Ring Based Cavities

6.2.1 Pinciples of Operation

As shown in Figure 6.2, the optofluidic microring dye laser was fabricated on a monolithic PDMS chip using replica molding soft lithography as described in Chapter 3. A microfluidic channel when filled with liquid of higher refractive index than that of PDMS (1.406, GE RTV 615) acts as a channel optical waveguide. When the cross section dimensions of the channel are 2μm by 3μm and the index contrast is less than 0.003, the waveguide supports only the two fundamental spatial modes. A 200μm diameter microring resonator which is side-coupled to a bus waveguide forms the laser cavity. For a single layer device, a fused coupling region (as shown in Figure 6.3-(a)) is used to enable the transporta-

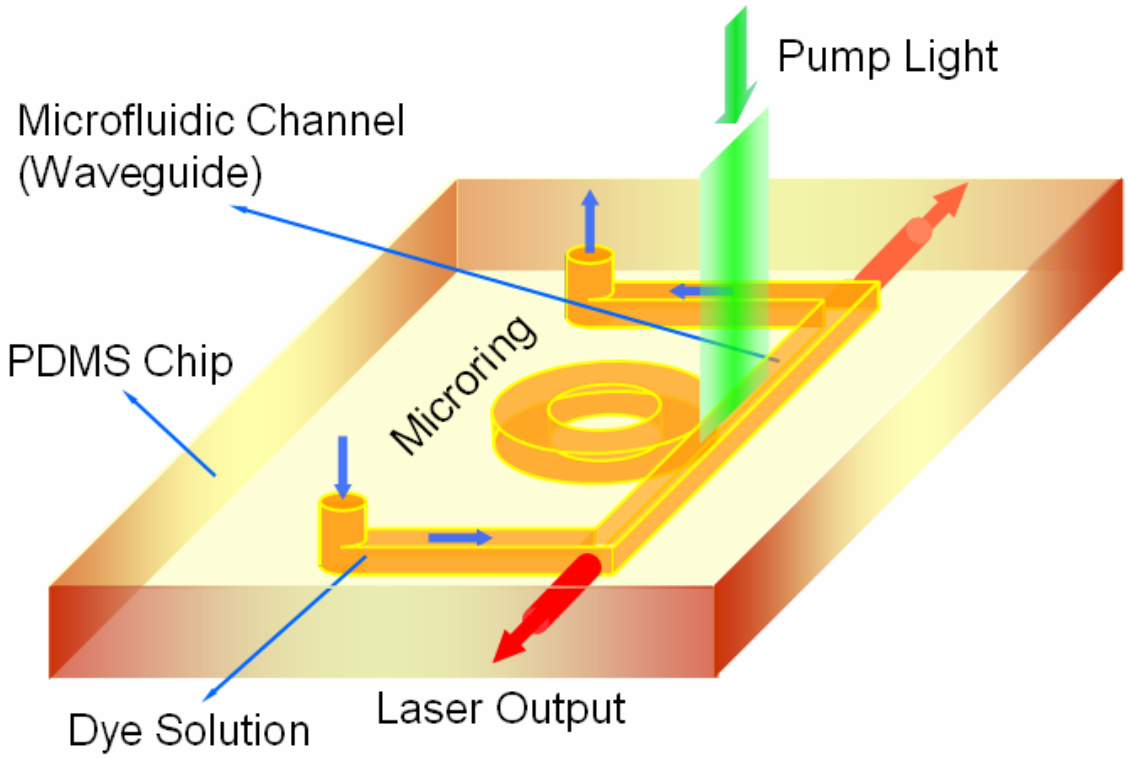

Figure 6.2: Schematic diagram of an optofluidic microring dye laser chip.

tion of dye solution into the microring. This introduces additional scattering losses which lower the loaded Q[4] and the coupling coefficient is expected to be large. These problems can be solved using a double layer structure in which the microring resonator and the bus waveguide are located in separate layers and vertical coupling scheme can be used. The gain medium is a 1mM solution of Rhodamine 6G in a methanol and ethylene glycol mixture with refractive index of 1.409. The pump light are 532nm Q-switched Nd:YAG laser pulses with 6 nanosecond pulse width. The pump light is focused by a cylindrical lens to a 500μm by 1000μm area covering the microring and a portion of the bus waveguide. Laser light coupled out of the microring into the bus waveguide can get further amplified by the pumped dye solution in the waveguide. The resonant wavelengths of a microring laser are determined by the condition

$$m\lambda_m = 2\pi n_{eff} R \tag{6.1}$$

(1) where λ_m is the mth resonant wavelength, n_{eff} is the effective index of the guided mode and R is the ring radius. For a 200μm diameter ring, this gives a FSR of 0.38nm around 580nm. It's clear from this expression that the optofluidic integration enables tunable laser wavelength by changing n_{eff}, R or m. The effective index can be varied by changing the refractive index of the liquid core. Due to the very low Young's modulus of PDMS (~750kPa [5]), the ring radius and shape can be mechanically changed by simply stretching or compressing the chip. Finally, the resonance order can be chosen by using different dye molecules which cover different spectral regions.

6.2.2 Lasing Results and Discussion

The transparent PDMS chip was placed on a high reflectivity mirror so that the transmitted pump light can be reflected vertically back to the laser cavity. This not only makes more efficient use of the pump light but also lowers the laser threshold. Furthermore, this makes possible a vertical resonant structure at the pump wavelength which can further reduce the laser threshold. The dye solution was pressure driven into the microfluidic channel by applying 10psi pressure at the inlet port. A 10X microscope objective was used to collect the emission light from one edge of the chip and deliver it to a spectrometer with 0.1nm resolution (Ocean Optics HR4000). A typical multiple longitudinal mode lasing spectrum is shown in Figure 6.3-(b) where the linewidth of each mode is < 0.1nm. The measured FSR agrees with the predicted value 0.25nm. A plot of laser output energy versus the absorbed pump energy is shown in Figure 6.4 The threshold pump energy is only 9.2nJ due to the small size of the laser. This is well within the reach of the output power of commercially available laser diodes. This device can be used an active biosensor without any modification, in which the analytes can be either functionally attached to the channel wall or directly injected into the liquid flow and the shift in lasing wavelength is detected. In the future, we plan to study the mechanical and fluidic tunability of this laser. In addition, in order to build a single mode microring dye laser, we'll use the Vernier effect in which two microring resonators with slightly different diameters will be used as the frequency selective element. Another interesting direction is to achieve mode locking by introducing

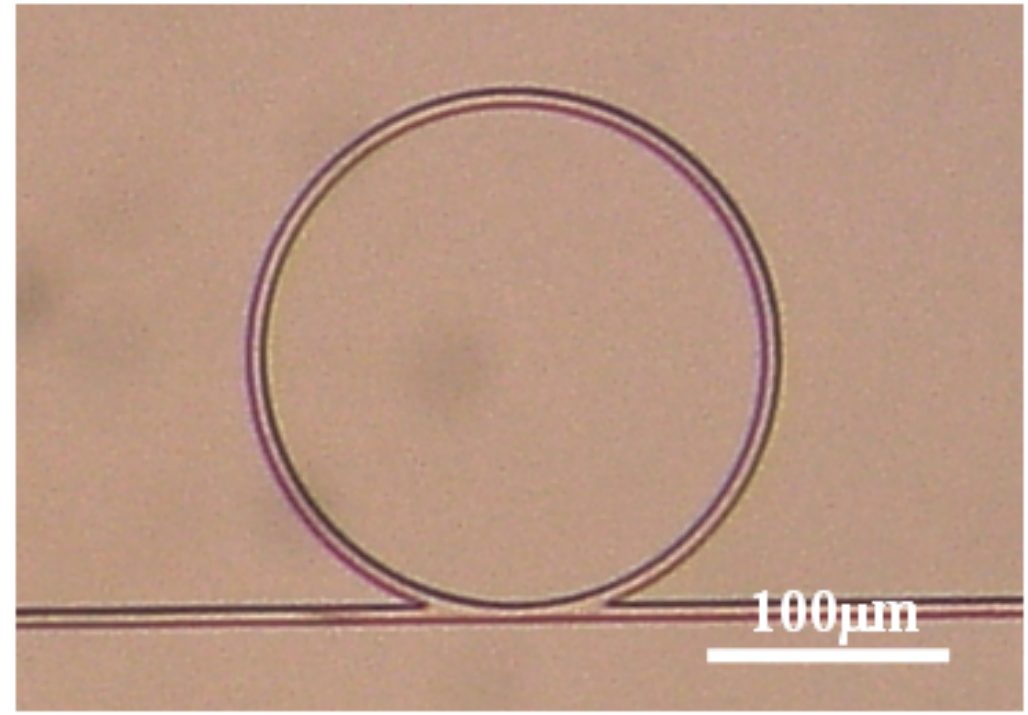

(a)

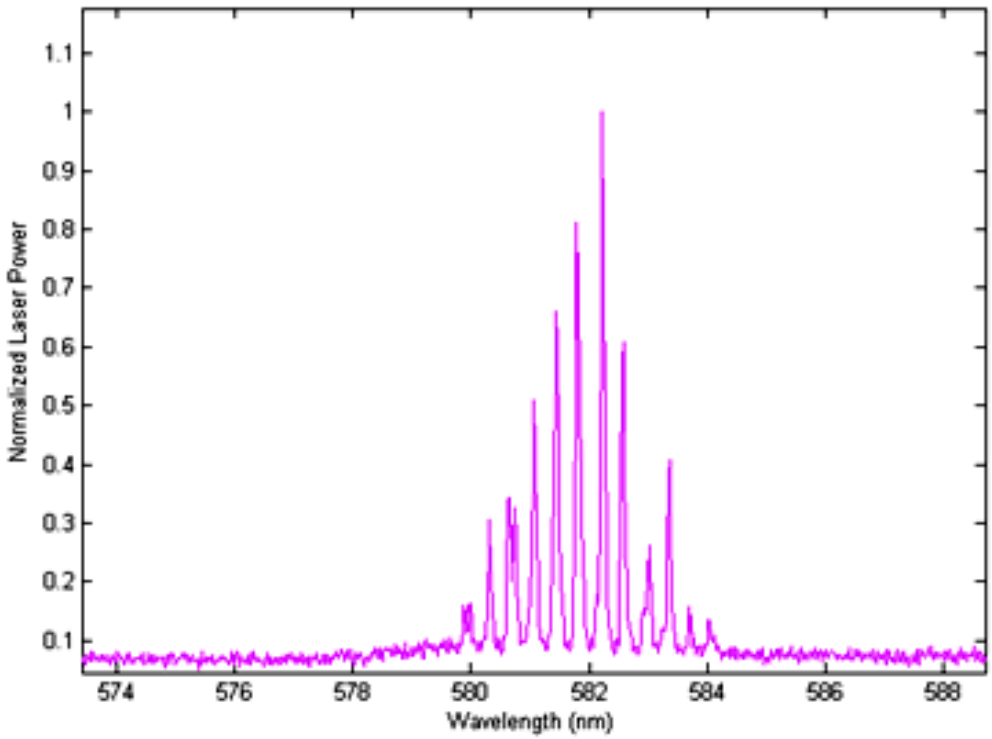

(b)

Figure 6.3: (a) Optical micrograph of an optofluidic microring resonator in PDMS. The waveguide dimensions are 3μm wide and 2μm high. The ring diameter is 200μm. (b) A typical measured lasing spectrum of an optofluidic microring dye laser with a 200μm diameter ring.

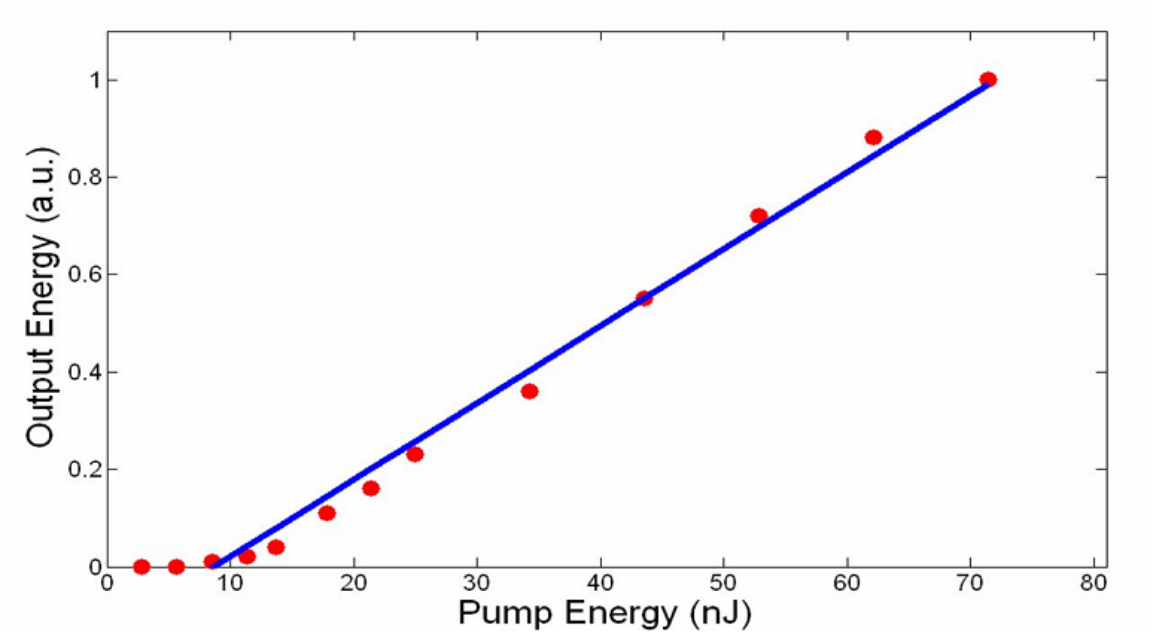

Figure 6.4: Light-in v.s. Light-out curve. The laser threshold is 9.2nJ.

saturable absorber dyes.

6.3 Coupled Microring Array Based Cavity

Among microring based photonic structures, coupled microring arrays have received much attention recently due to their potential use as a slow light structure [111] [112]. Not surprisingly, slow light structures can often form laser cavities due to the geometrical resonance and slow group velocities they possess. In this section, we use a coupled microring array to form a laser cavity and demonstrate single frequency lasing using the Vernier effect.

6.3.1 Coupled Microring Arrays and Vernier Operation

It has been shown when a series of microring resonators periodically side coupled to two bus waveguides (also called double-channel side-coupled integrated spaced sequence of resonators (SCISSORs)), the structure exhibits photonic bandgaps due to both the distributed feedback resonances caused by the bus waveguides and the microring resonances

[112]. When the ring separations are equal to half of the ring circumference, these two bandgaps overlap. Here we use this degenerate coupled ring structure as a laser cavity. In addition, we use the Vernier effect to increase the FSR of the cavity by using rings with two different diameters. The detailed structure is shown in Figure 6.6. The two ring radii are $R1$ = 5μm and $R2$ = 5.4μm . The ring separation is chosen to be $\pi(R1+R2)/2$ so that the "Bragg gaps" and the "ring resonator gaps" overlap [112], resulting in simplified band structure. Defect modes are formed in the bandgaps by introducing a suitable waveguide phase shift in the center [113]. In our case, the defect length L_{defect} is close to $1.5\pi(R1 + R2)/2$.

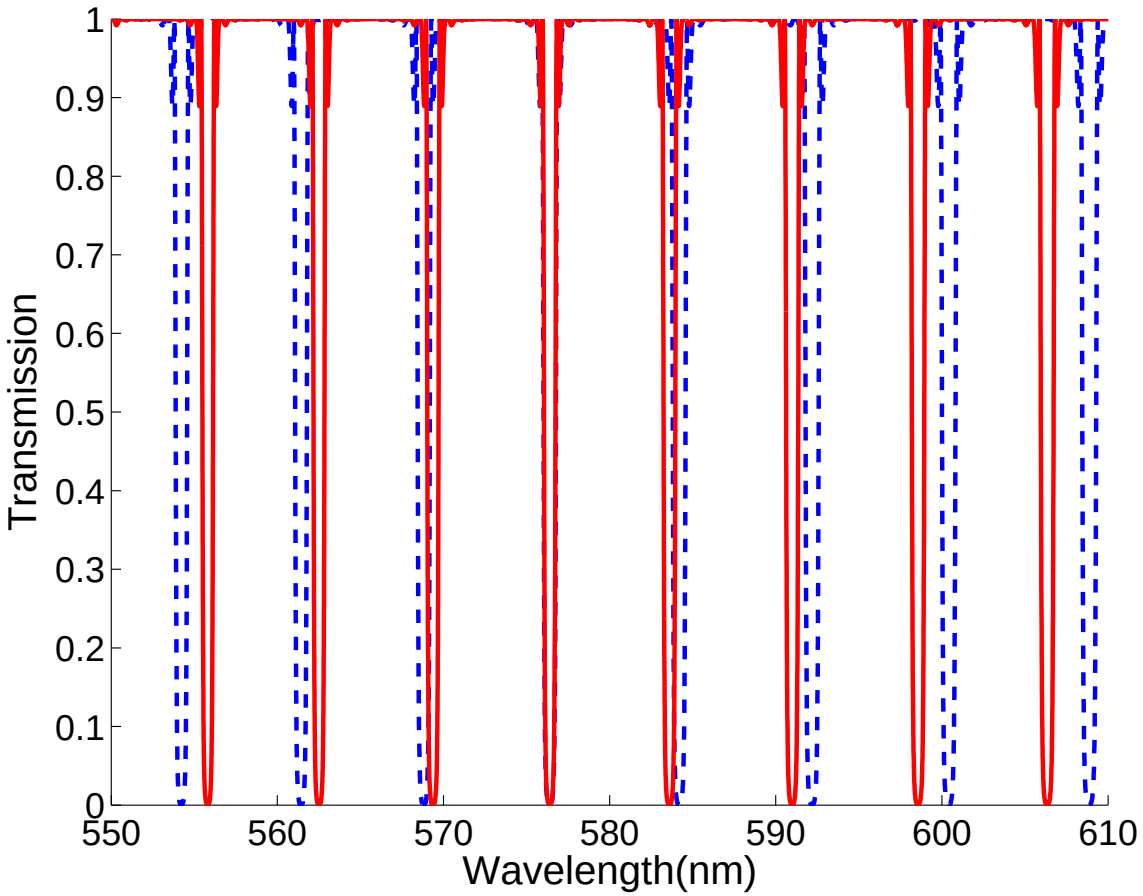

Figure 6.5: Vernier operation of coupled microring resonators. The simulated transmission spectra due to the two different diameter rings. Only the stopband around 590nm overlap completely, others are misaligned due to the different ring diameters. The detail of the structure is shown in Figure 6.6.

When two different ring diameters are used, the bandgaps due to the two different ring

resonances are normally misaligned, and only overlap at specific wavelengths due to the Vernier effect [20]. We used the transmission matrix given in [112] for the unit cells to simulated the overall transmission spectrum of the structure. Figure 6.5 shows the simulated transmission spectra due to the two different diameter rings. It can be seen that only the bandgap around 576.4nm overlap completely, all others are misaligned between the spectrum range from 550nm to 610nm.

6.3.2 Single Mode Microring Dye Lasing Results

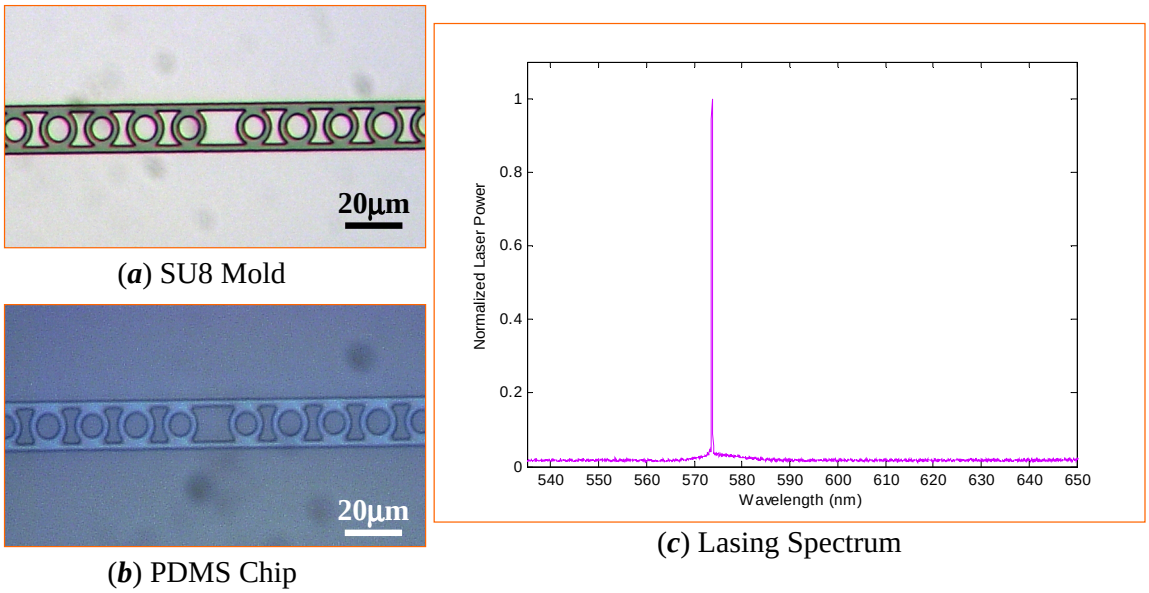

(***a***) SU8 Mold

(***b***) PDMS Chip

(***c***) Lasing Spectrum

Figure 6.6: Single mode optofluidic microring dye laser using Vernier effect. The laser cavity is a distributed feedback coupled microring structure between two bus waveguides. The two ring radii are $R1 = 5\mu$m and $R1 = 5.4\mu$m . The ring separation is chosen to be $\pi(R1 + R2)/2$ to simplify the photonic band structure. The central larger waveguide separation forms a defect mode in the band gap. The transverse dimentions of all the waveguides are 2μm by 2μm

1mM Rh6G dye solution with refractive index of 1.415 was introduced into the 2μm by 2μm microfluidic channel to form the waveguide core. The laser chip was optically pumped with 6ns Q-switched frequency doubled Nd:YAG laser pulses of 532nm wavelength, focused to a ~50μm wide stripe aligned with the dye laser cavity. The rest of the characterization setup is the same as given in Chapter 3. Single frequency lasing was ob-

served with pump levels from ~1mJ/cm^2 to ~2mJ/cm^2. The lasing wavelength of ~574nm is close to the predicted value of 576.4nm. The relative large laser threshold is likely due to the lossy coupling regions between the ring resonators and the waveguides, and the small ring diameters.

6.4 Summary

We have demonstrated, for the first time, a microfabricated liquid-core microring dye laser on a monolithic PDMS chip. The fabrication and operation of the laser chip is fully compatible with PDMS based microfluidics technology [5]. We have also demonstrated a single frequency microring dye laser using the Vernier effect with a coupled ring array based cavity. Besides low threshold laser applications, such liquid-core microring resonators can also be used to build optical filters, biosensors and ultrashort pulse generators on a microfluidic chip.

Chapter 7

Evanescent Gain Optofluidic Dye Lasers

The dye laser cavities in all previous chapters rely on liquid-core channel waveguides. In such structures, in order to obtain single spatial mode operation, the waveguide (channel) dimensions must be on the order of a few microns or smaller. Therefore, relative high pressures (~10psi) are needed to push liquid dye solutions into such small channels, which inevitably limits the maximum flow rate achievable in these devices. This is a rather undesirable feature when high flow rate is needed such as in fast tuning devices or CW dye lasers which require fast replenishment of the photo-bleached or triplet-state trapped dye molecules. In addition, the refractive index of the liquid core must be higher than that of the cladding (in our case, 1.406 PDMS). This rules out the use of more popular low index solvents such as water, ethanol and methanol. To remove the above limitations, in this chapter, we introduce a liquid-cladding waveguide DFB laser structure based on evanescent gain. We also present a proof-of-concept experiment which clearly showed evanescent gain laser action.

7.1 Liquid-Cladding DFB Dye Lasers Based on Evanescent Gain

7.1.1 Liquid-Cladding Waveguide

In stead of the waveguide core, liquid dye solutions can also be used to form the cladding of a waveguide structure as shown in Figure 7.1. A patterned high index material,

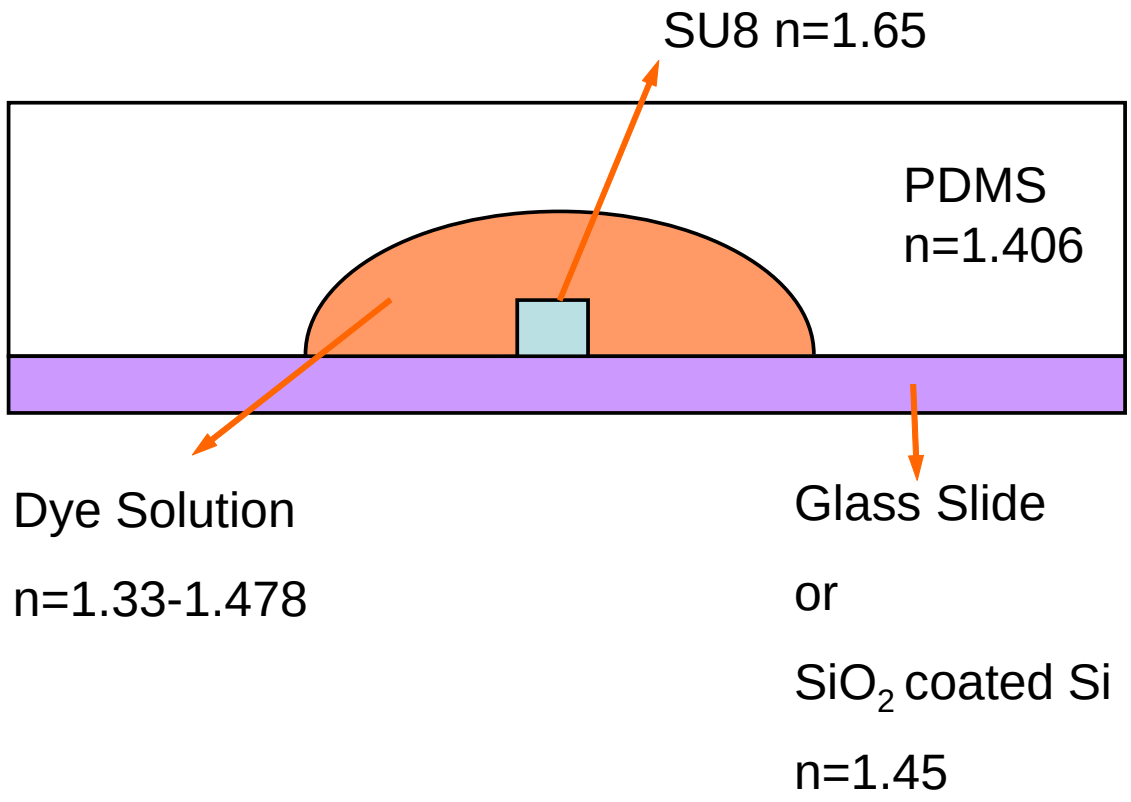

Figure 7.1: Schematic cross section of a liquid-cladding waveguide structure.

such as SU8 (n=1.65), acts as the core of the waveguide when it is deposited on a low index substrate, such as glass and polymethylmethacrylate (PMMA). A microfluidic channel with a large cross-section can then be aligned to cover the solid core, and the low index liquid subsequently introduced into the channel forms part of the waveguide cladding. If the upper cladding liquid is a pumped dye solution, the evanescent tail of the guide mode can extract energy from the dye solution and lead to optical gain.

Compared with liquid-core structures, liquid-cladding waveguides allow the use of more popular low index solvents in the dye solutions such as water, ethanol and methanol. More liquid choices also lead to a larger available refractive index tuning range. The large dimensions of the microfluidic channel also allow much faster flow rate of the dye solution. For example, if the channel is 100μm wide and 10μm high, a 40psi applied pressure can drive the liquid at the center of the channel to move at a 10 meter/second velocity. This rate is fast enough to allow us to consider the possible CW dye laser operation in such

structures [114] [115]. The higher index contrast between the core and the cladding also allows smaller device footprints and higher integration densities.

7.1.2 Evanescent Gain DFB Laser Cavity

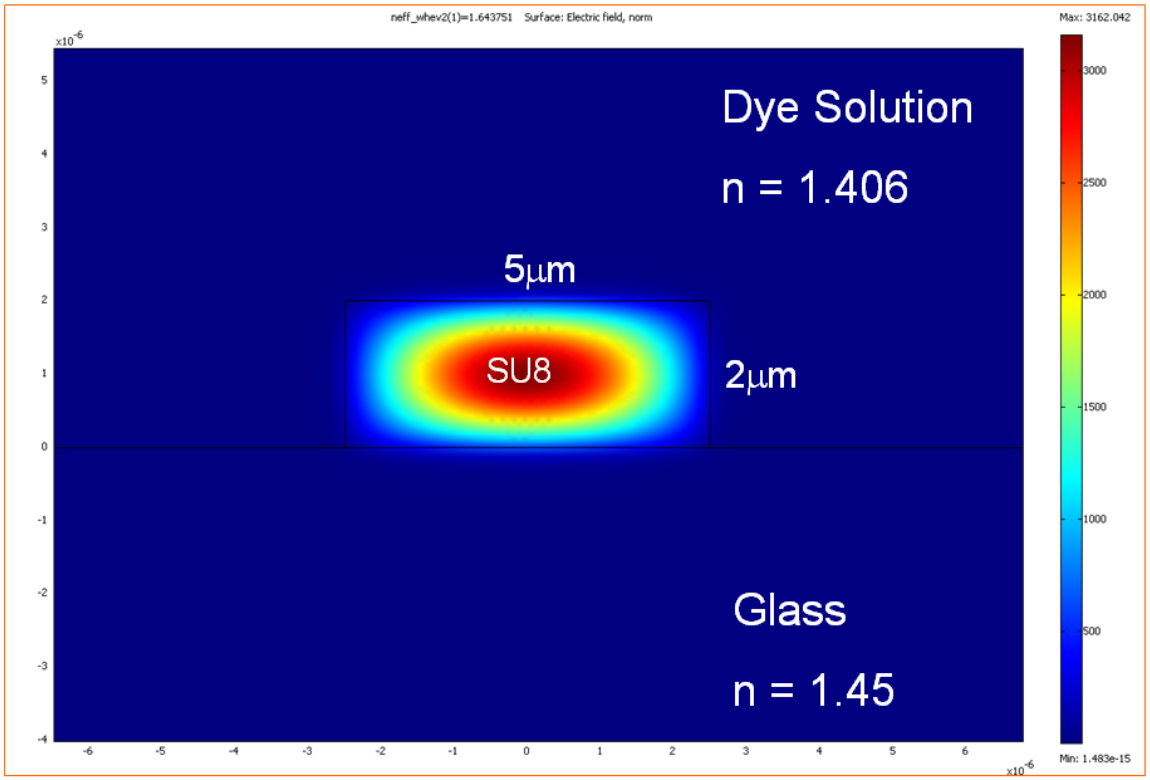

Figure 7.2: Fundamental transverse mode profile of the liquid-cladding waveguide simulated by FEM (Comsol FEMLAB 3.2). The effective index is 1.643 at 580nm.

For a proof-of-concept demonstration, we used the same higher order DFB cavity geometry used in Chapter 3. The main advantage is that it allows us to use same set of photomasks to fabricate the devices used in this chapter. Recall that the core dimensions are 5μm wide and 2μm high. The previous periodic posts inside the channel now become periodic holes. The dimensions of these holes are 3μm wide and 1.5μm long (half grating period). The microfluidic channels we used were rounded PDMS channels with 100μm width and 20μm height. The refractive index of the dye solution was tuned to be 1.406, the same as PDMS, to avoid reflections from the dye solution and PDMS interface.

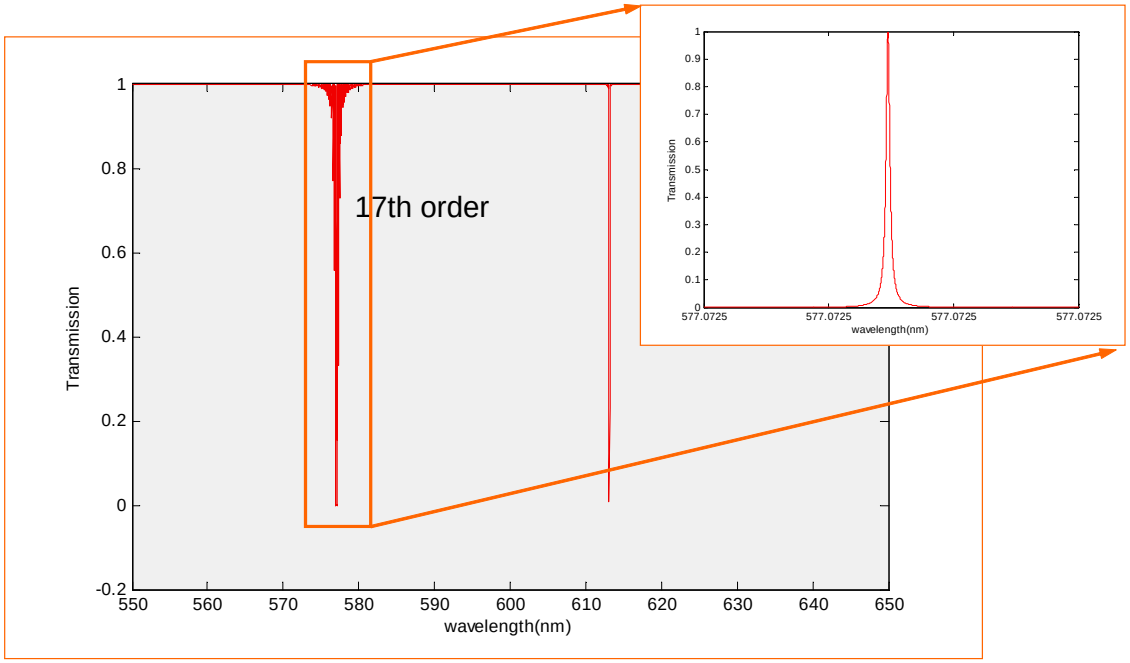

Figure 7.3: Simulated longitudinal mode spectrum of the liquid-cladding DFB structure. The effective index 1.643 used in the simulation is that of the fundamental transverse mode.

We did the same FEM simulations (Comsol FEMLAB 3.2) as in Chapter 3 with the new refractive indices to obtain the transverse mode profile and the effective index, which are shown in Figure 7.2. Now that the structure has much higher index contrast between the core and the claddings (1.65 v.s. 1.406&1.45), it is no longer a single mode waveguide. As an example, Figure 7.2 shows only the fundamental transverse mode. The effective index of the fundamental mode is 1.643 at 580nm. It is clear that most of the mode resides inside the solid core, which leads to a small overlap with the gain region. Thus, in an evanescent gain structure, the higher order spatial modes are more favored for laser action due to the large overlap between the evanescent tails with the gain medium.

The longitudinal mode spectrum of the DFB structure was simulated using Rouard's method as described in Chapter 3. For example, Figure 7.3 shows the simulated transmission spectrum using the effective index of the fundamental mode. The DFB structure has its 17th resonance around 577nm which is close to the gain peak of Rhodamine 6G (Rh6G). An effective $\lambda/4$ defect was introduced at the center of the grating to break the doubly degeneracy of a uniform DFB laser. The inset of Figure 7.3 shows the transmission resonance

due to the defect mode.

The structure of this laser cavity is not optimized for evanescent gain operation. The large and asymmetric waveguide core supports more than 40 transverse modes according to FEM simulation, which can lead to very complicated laser behaviors. A sub-wavelength scale waveguide should give much better transverse mode control, and larger overlap between the evanescent tail and the gain region. For example, all other parameters the same,

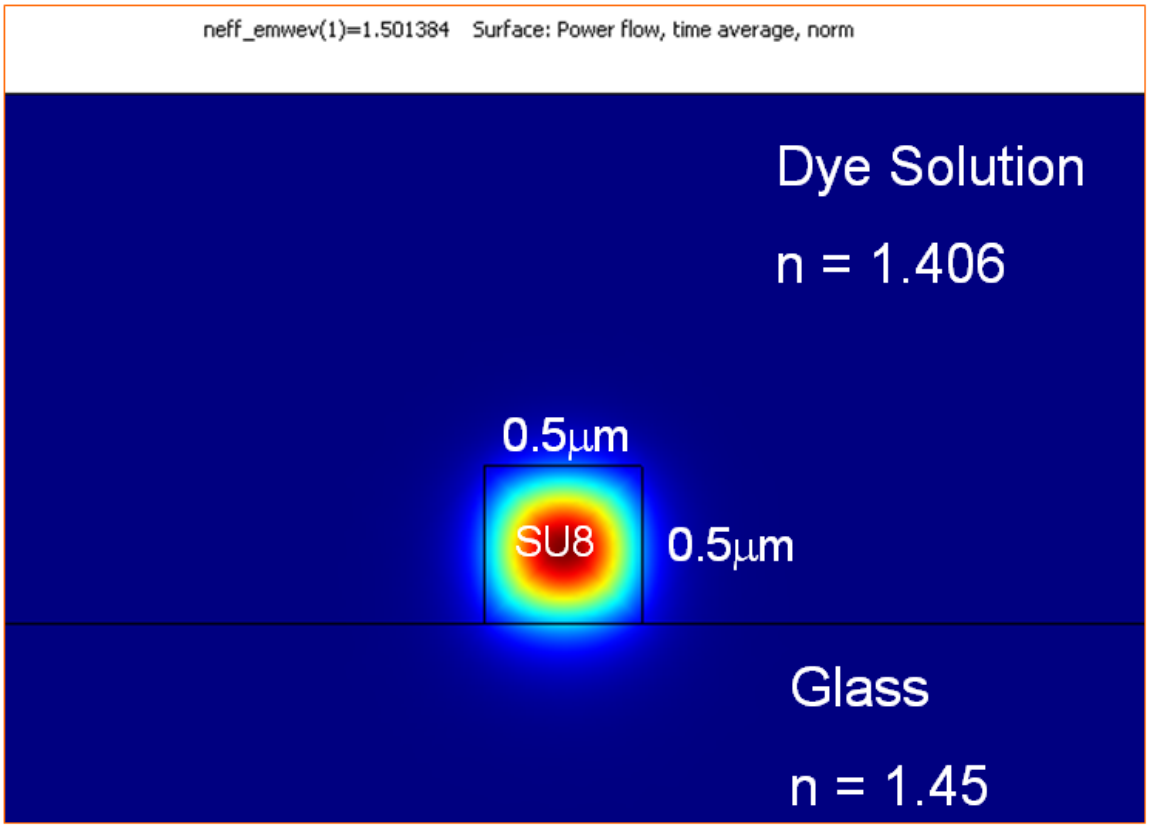

Figure 7.4: A single mode sub-wavelength scale waveguide with a large overlapping factor between the mode and the upper cladding.

FEM simulation (Figure 7.4) shows that a waveguide core with 0.5μm by 0.5μm dimensions supports only the fundamental transverse mode at 580nm, and has a overlapping factor of 15% between the mode and the upper cladding region. Even larger overlapping factor (thus modal gain) can be obtained by further decreasing the core size or increasing the dye solution index. The fabrication of such sub-wavelength scale waveguides requires advanced fabrication methods such Ebeam lithography, Focused Ion Beam milling or EUV

lithography.

7.2 Fabrication

The fabrication method of the SU8 core on the low index substrate is essentially the same as the one used to make the mold for the 15th order DFB dye laser. The only different is now the substrate is no long a silicon wafer. The substrates we have used so far include silicon wafers coated with a 5μm thick SiO_2 layer and normal microscope glass slides. The detailed fabrication process can be found in Appendix A. Although the glass slides are inexpensive and transparent, the fabrication on glass slide turned our to be problematic. The bonding between SU8 and SiO_2 is relative weak. Therefore slow cooling during the several baking steps (Appendix A) is essential to reduce the stress between SU8 and the substrate. Due to the poor thermal conductivity of glass, the cooling steps with glass slides are more difficult to control than with Si wafers, and often lead to detached or warped SU8 structures as shown in Figure 7.5-(a). The devices fabricated on SiO_2 coated Si wafers have much better qualities as shown in Figure 7.5-(b). Therefore in this chapter we only discuss the devices fabricated on Si wafers coated with a 5μm thick silicon dioxide layer. The PDMS microfluidic channels were fabricated with replica molding soft lithography as before. The wafer and the PDMS channel were both treated with O_2 plasma for 30 seconds at 80W in order to form a permentant bonding. The PDMS channels were then aligned and bonded with the SU8 waveguides under a steroscope or mask aligner. Then the whole chip was baked at $80^{0\text{ø}}$ overnight. A typical device is shown in Figure 7.6.

There exist polymer materials with even lower refractive index than glass, such as Cytop^{TM} (Asahi Glass). Devices fabricated on such substrates can shorten the evanescent tails in the substrate and lead to more efficient overlap of the guide mode with the gain material.

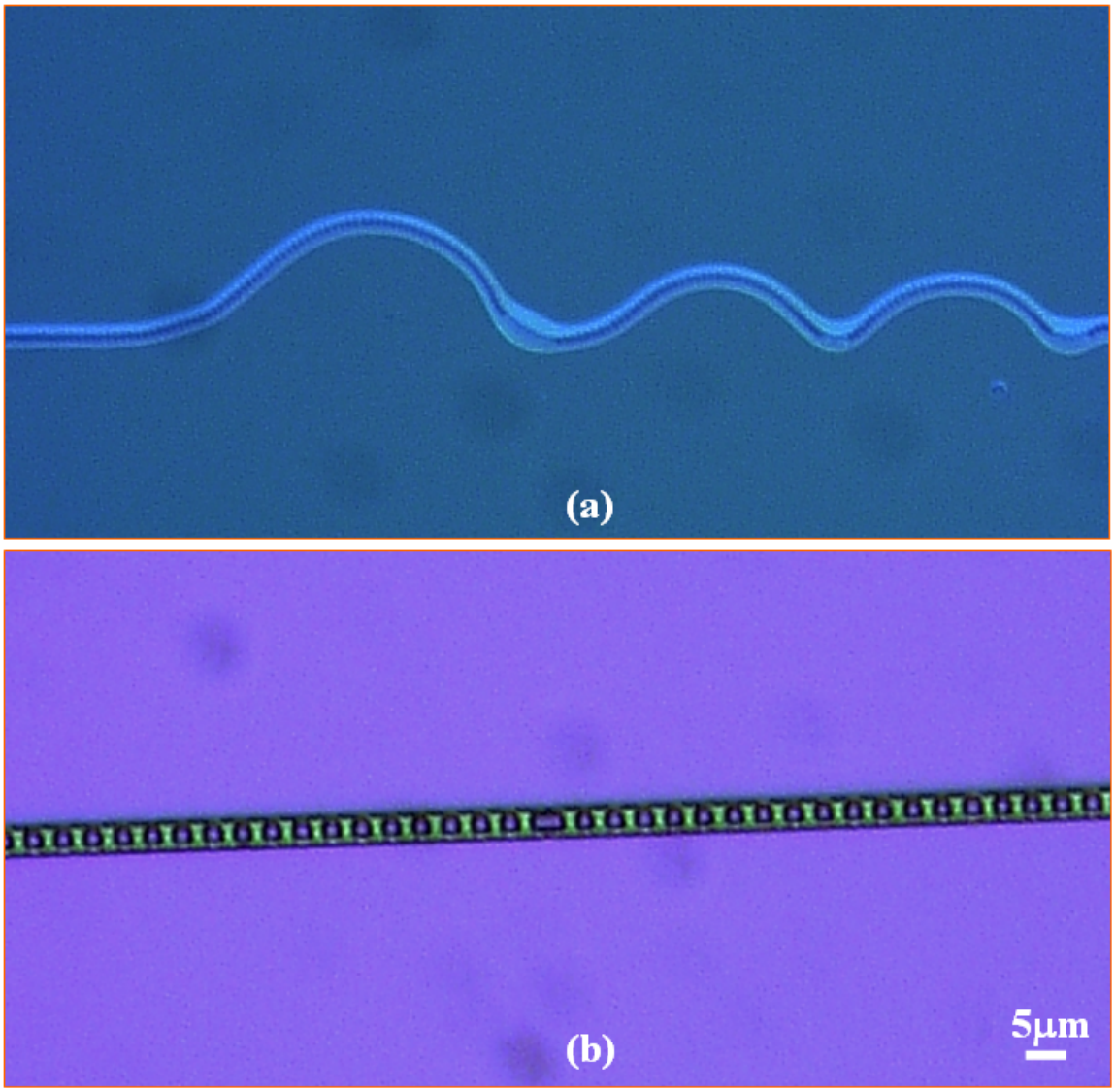

Figure 7.5: Fabrication of SU8 DFB waveguide cores on glass slides and silicon dioxide coated Si wafers. (a). SU8 waveguide detached from the glass slide substrate (b). High quality SU8 waveguide on SiO_2 coated Si wafer.

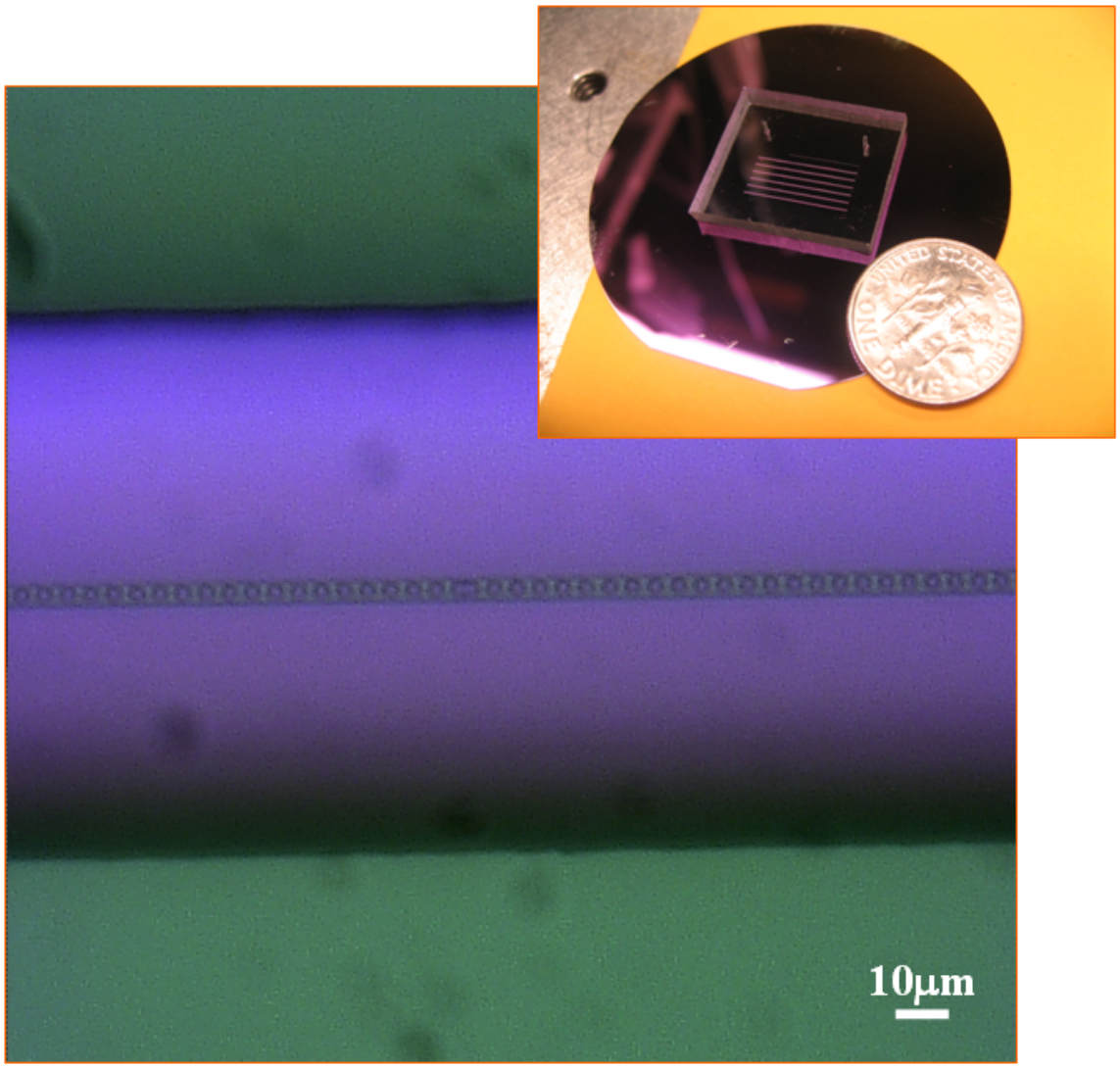

Figure 7.6: Optical micrograph of an liquid-cladding evanescent gain DFB dye laser. The SU8 DFB waveguide core is under a 100μm wide PDMS microfluidic channel. The channel height is 10μm. The inset shows an actual chip on a 2 inch wafer.

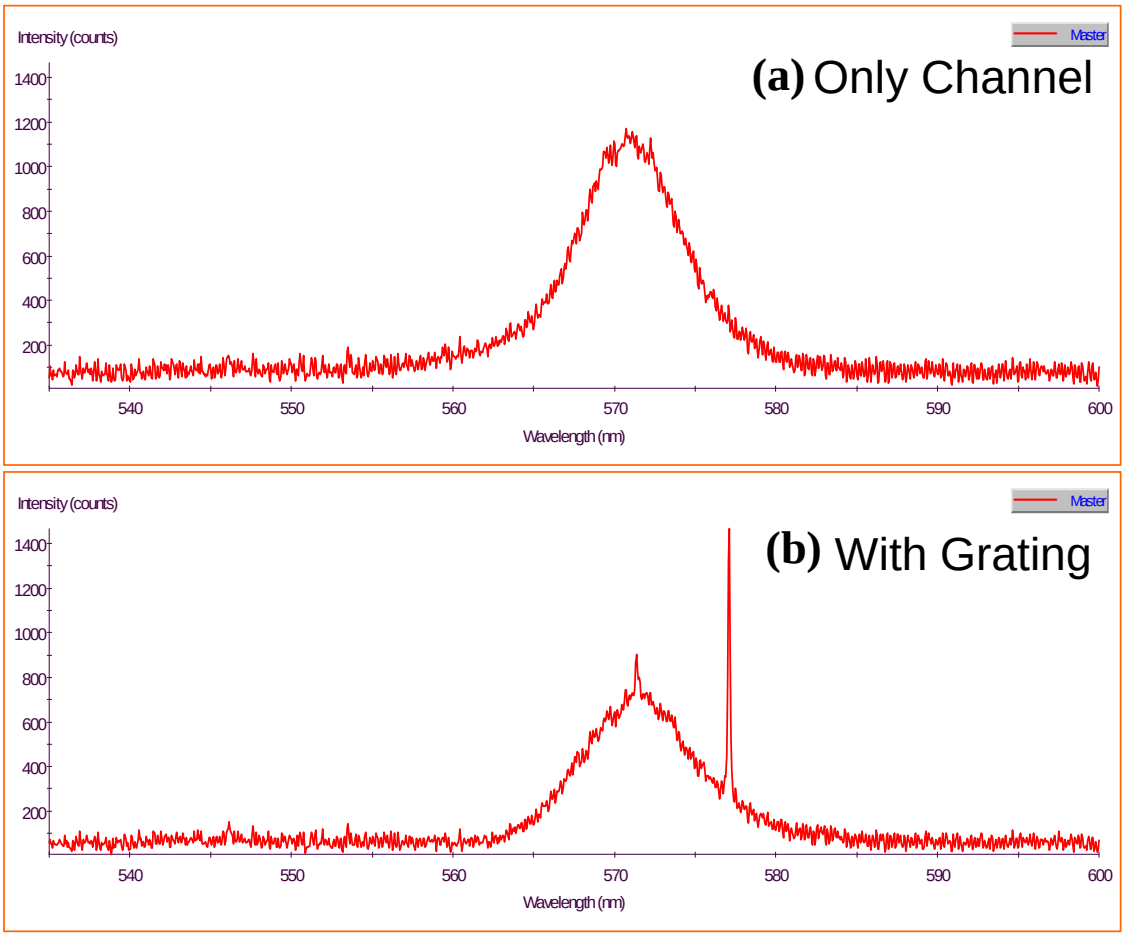

Figure 7.7: (a) Emission spectrum of a PDMS channel filled with Rh6G dye solution, without the SU8 DFB waveguide core. (b) Lasing spectrum with the SU8 DFB waveguide core.

7.3 Preliminary Lasing Results and Discussion

The preliminary lasing results were shown in Figure 7.7. A 1mM Rh6G dye solution in a mixture of methanol and ethylene glycol with a refractive index 1.406 (equally to that of PDMS) was pressure driven into the microfluidic channel. Very low pressure was needed to push the liquid in due to the large channel dimensions. When a high pressure >40psi was applied at the inlet port, we estimated the average linear flow velocity higher than 10m/s by measuring the total volume of liquid passing through the device in a certain time. This shows the structure indeed support ultra-fast flow rate needed for CW dye

lasers. The laser chip was transversely pumped with 6ns Q-switched frequency doubled Nd:YAG laser pulses of 532nm wavelength. The pump pulses were focused to a ~20μm wide stripe aligned with the SU8 core. A 10X microscope objective was used to collect the emission light from one edge of the chip and deliver it to a fiber coupled CCD-array based spectrometer with 0.1nm resolution (Ocean Optics HR4000). A typical lasing spectrum is shown in Figure 7.7-(b) where the lasing wavelength is 569nm, close to the predicted 17th resonance for the fundamental transverse mode. A minor line was also observed at the peak of the broad fluorescent spectrum. The rather strong fluorescence background is due to the spontaneous emission noises by the excited dyes that do not participate in the evanescent gain. A longitudinal pump geometry can reduce the spontaneous emission noise, in which the pump light is end coupled into the waveguide core and pump the dyes through evanescent tails. In order to rule out the lasing possibilities due to other resonant structures in the system, such as the facet reflections, we also did a control experiment in which a dye solution filled microfluidic channel with the SU8 waveguide core was pumped. In this case, we did not observe laser action as shown in Figure 7.7-(a).

It is a rather surprising result that the lasing wavelength was close to the predicted value for the fundamental transverse mode, since the fundamental mode has the smallest overlapping factor with the gain region. One possible explanation is that it may be a coincidence that a lower order DFB resonance for some higher order transverse modes accidentally matches this wavelength, given the large number of transverse modes supported. More systematic studies based on both simulations and experiments are needed to quantitatively explain the lasing results. Nonetheless, this result clearly demonstrated a liquid-cladding evanescent gain structure can support DFB dye lasing.

7.4 Summary

In this chapter, we have proposed a novel liquid-cladding evanescent gain structure for optofluidic dye lasers. Preliminary experimental results clearly showed laser action with a higher order DFB cavity. The fabrication methods and theoretical design considerations are given. Sub-wavelength scale waveguides and longitudinal pump geometries are suggested

for improving the performances of evanescent gain lasers. The liquid-cladding structures may prove more favorable for applications that requires fast flow rate, larger index tuning range and smaller footprint.

Chapter 8

Towards an LED Pumped On-Chip Dye Laser Using a Surface Emitting Circular-Grating Resonator

The cavity geometries of the distributed feedback (DFB) and microring resonators in the previous chapters do not match well with the emitting area of a light emitting diode (LED). In this chapter, we demonstrate an optically pumped surface emitting polymer dye laser fabricated by nanoimprint lithography. The laser cavity consists of a second order circular grating distributed feedback structure which has a similar emitting area to that of a LED. Our laser is based on an organic dye hosted within a polymethylmethacrylate (PMMA) matrix coated on a transparent glass substrate. The nanoimprinted solid-state dye laser described here offers a low cost (disposable) and compact coherent light source for lab-on-chip spectroscopy systems. The laser also has a low pump threshold as well as a geometry well matched to LED pump sources, which provides an interesting alternative for constructing portable polymer laser devices.

8.1 Dye Doped Solid State Polymer Lasers

Within recent years the development of polymer dye lasers has progressed to higher levels of performance and functionality. The most attractive advantages of polymer dye lasers include low-cost processing, wide choice of emission wavelengths, and easy fabrication on flexible substrates. Several waveguide dye lasers have been studied with emission

wavelengths ranging from ultraviolet to the near infrared [116] [108]. By simply changing the fluorophore doped in the polymer these lasers can be used as the tunable sources for various applications including spectroscopy [108]. The 1-D Distributed feedback (DFB) structure is a widely employed resonator geometry, and has been previously demonstrated for polymer lasers [117]. Operating characteristics can be significantly improved within two dimensional structures. Here, we choose a circular grating distributed feedback structure to obtain low threshold operation, a well defined output beam, and vertical emission perpendicular to the device plane. Although surface emitting circular grating lasers using semiconducting polymers have been previously demonstrated by Bauer et. al [118] and Turnbull et. al [119], their lasers were fabricated by depositing the organic gain material onto a prepatterned dielectric substrates, limiting the depth and the accuracy of the shape of the grating. For better geometric control, we choose nanoimprint lithography15 as a direct patterning method. A hard mold is used to transfer patterns with high fidelity into target polymers, and this technique has become an attractive approach to define nanofabricated optical resonator structures. Conjugated polymer lasers fabricated by hot embossing have been studied by Lawrence et. al [120], and 1-D DFB lasers based on organic oligomers using a room temperature nanoimprint method were reported by Pisignano et. al [121] [122].

In this chapter, we present a circular grating distributed feedback laser fabricated on dye-doped poly(methylmethacrylate) (PMMA) films. The laser was fabricated on a glass substrate using a low-cost and manufacturable nanoimprint method. Lasing with single frequency surface emission at 618.52nm and a linewidth of 0.18nm was measured from the polymer dye laser exhibiting a threshold value of 1.31nJ/mm^2. The laser operation characteristics of circular grating resonator are improved through the high accuracy and aspect ratio nanoimprint pattern transfer. Moreover, the mold can be re-used repeatedly, providing a convenient way of mass production and large scale fabrication of low cost polymer dye laser arrays.

8.2 Circular Grating Resonator Design and Fabrication

8.2.1 Circular Grating Distributed Feedback Resonators

The circular grating structure proposed [123] and demonstrated [124] by Erdogan and Hall provides a natural two-dimensional extension of the basic DFB structure. It allows feedback to be applied in all in-plane directions, and the second order grating couples the emitted radiation perpendicularly out of the surface of the sample. Figure 8.1 shows a general design of a circular grating distributed feedback structure. A theoretical analysis

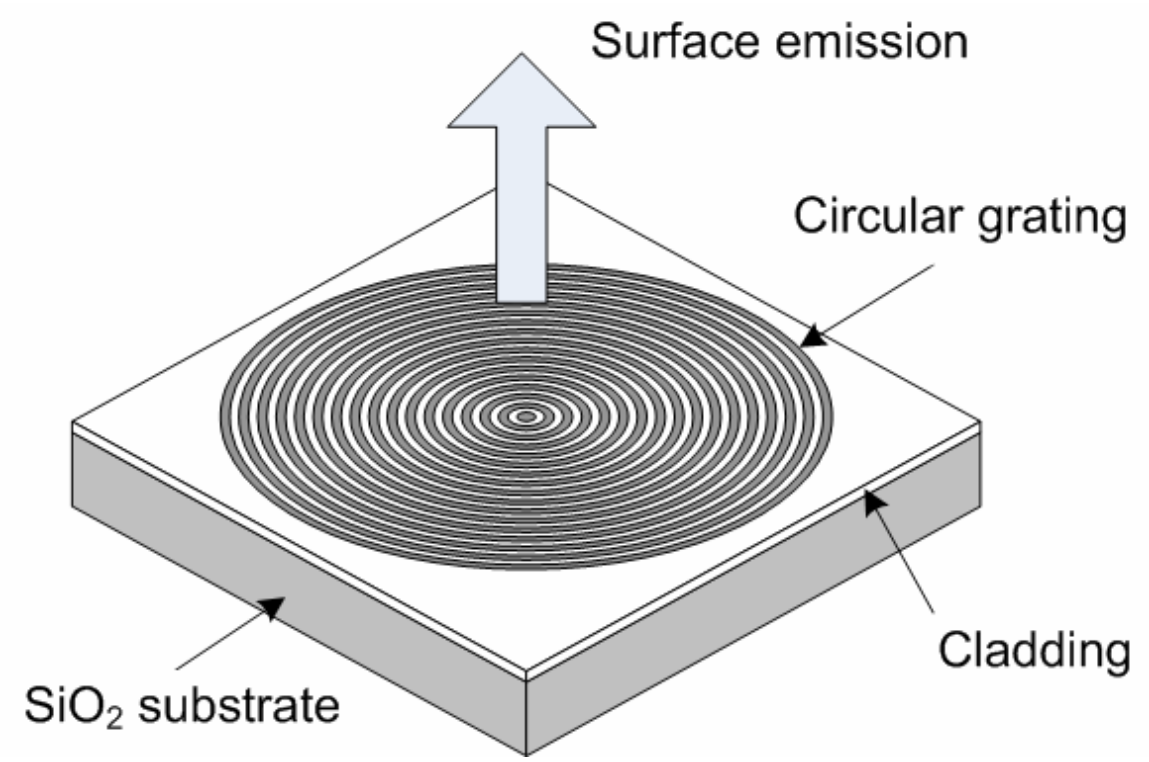

Figure 8.1: General design of a circular grating distributed feedback structure.

of circular grating lasers is described in detail elsewhere [124] [125] [126] [127] [119] predicting that only the radial propagating components define the modes in the circularly symmetric grating. The design parameters of the circular gratings fabricated for this paper are selected based on electromagnetic mode calculations and experimental results. A grating period of 440nm is chosen to match the second order Bragg condition. The cen-

ter defect is a 440nm diameter gain region. The 400nm groove depth is defined to ensure maximum confinement, whereas the 200μm overall diameter of the circular grating and the 50% duty cycle are used to reach the maximum coupling strength [128].

8.2.2 Nanoimprint Lithography

In our experiments, silicon dioxide (SiO_2) was used as the mold material and the grating pattern was defined by electron beam lithography on a LEICA EBPG 5000+ electron beam writer with proximity correction. The pattern was subsequently transferred into a SiO_2 substrate via reactive ion etching using CHF_3 plasma. PMMA was selected as the polymer matrix because of the solubility of the dye in PMMA as well as its low optical absorption within the wavelength range for activating the dye molecules, and its excellent properties for nanoimprint lithography [129].

To construct the dye laser, a glass substrate was spin-coated with 5μm of Cytop, a low refractive index material (n=1.34, Asahi Glass) as the lower cladding. Then, 500nm Dye (Rhodamine 640, Exciton)-doped PMMA (30mM) was spin-coated on top of the Cytop layer as the gain medium. An oxygen plasma treatment (Anatech SP100) of the Cytop was necessary for good adhesion of Cytop to the PMMA.

Nanoimprint lithography exploits the glass transition of polymers to achieve high fidelity pattern transfer. However, degradation of light emission efficiency of the organic materials during air exposure at high temperatures presents a challenge in nanoimprint lithography [130]. To solve this problem, a modified nanoimprint method is used to prevent this degradation of the dye-doped PMMA film by sealing the mold and the PMMA substrate into a curable polymer during the imprinting process. A mold release agent such as 1H,1H,2H,2H-perfluorodecyl-trichlorosilane (Alfa Aesar) was also deposited on the dye from the vapor phase to reduce the resist adhesion to the mold. Then, the mold was pressed into the PMMA film by using an automatic mounting press machine (Buehler SimpliMet 1000) at a temperature of 150^{o}C (above PMMA's glass transition temperature) and a pressure of 1200psi. After sample cooling, the mold could be easily separated from the patterned polymer laser chip. The fabrication process flow is schematized in Figure 8.2.

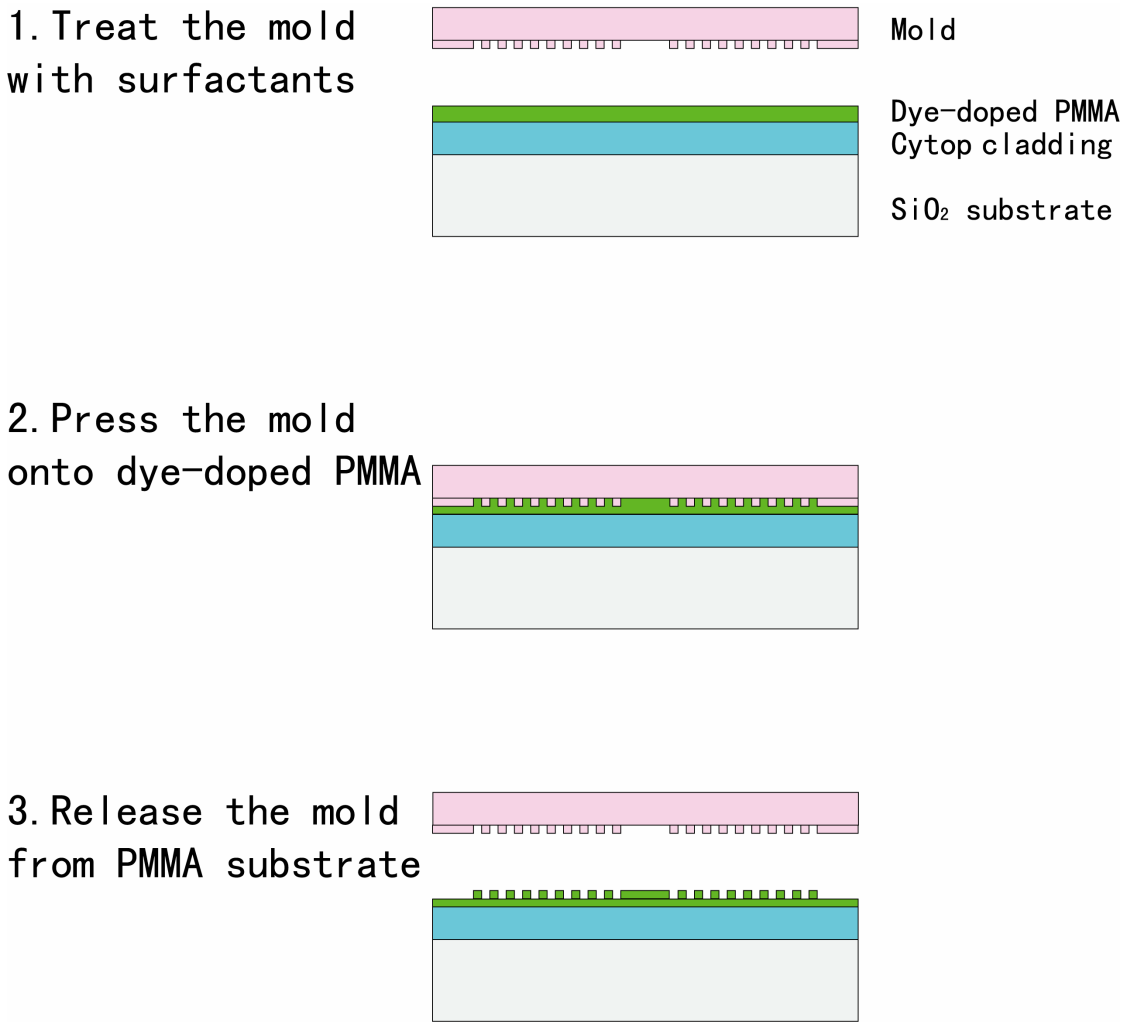

Figure 8.2: Fabrication process flow of circular grating polymer dye lasers.

Figure 8.3 shows SEM images of the mold and the imprinted PMMA. From these pictures, we can observe that the structure on the SiO_2 mold is faithfully replicated on the PMMA substrate surface with high resolution. Photoluminescence spectra confirm that there is no degradation of the luminescence performance of the polymer.

8.3 Lasing Results and Discussion

The polymer laser chip was optically pumped with 6ns Q-switched Nd:YAG laser pulses at 532nm wavelength, focused through a 20X objective to the back side of the chip.

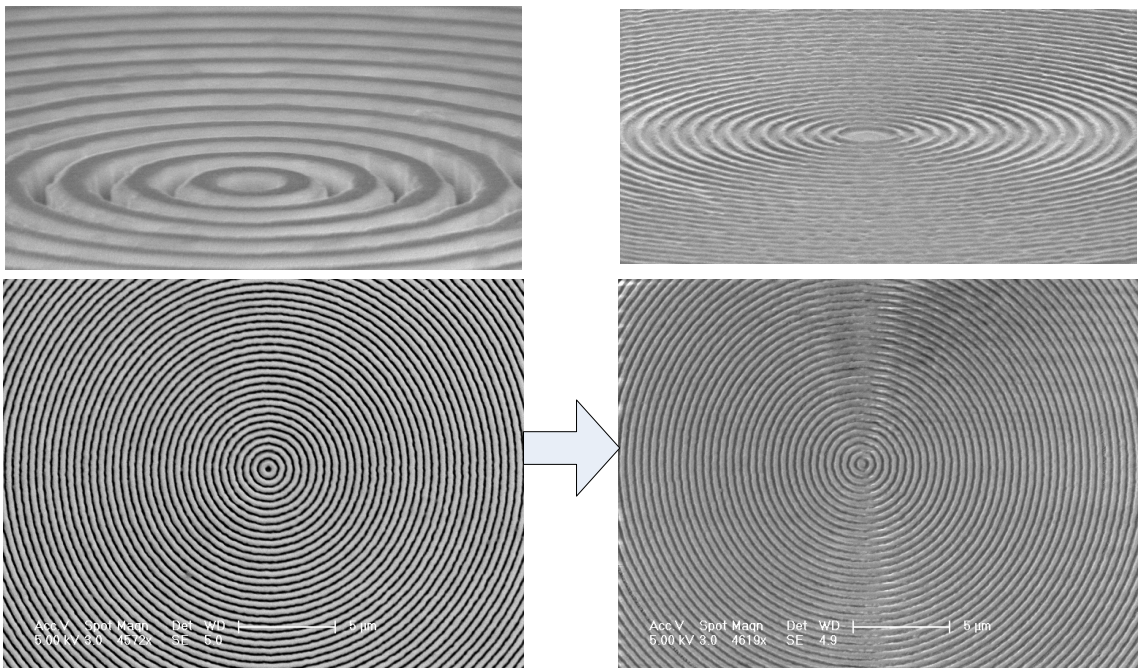

Figure 8.3: SEM images of (a) the SiO2 mold and (b) the imprinted PMMA film.

A 10X microscope objective was used to collect the emission from the top surface of the chip and deliver it to a fiber coupled CCD-array based spectrometer with 0.1nm resolution (Ocean Optics HR4000). A typical single frequency lasing spectrum is shown in Figure 8.4. The lasing wavelength is 618.52nm, and the measured linewidth is 0.18nm. Lasing occurs near the Bragg resonance, determined by the equation

$$m\lambda_{Bragg} = 2n_{\text{eff}}\Lambda \tag{8.1}$$

where $m = 2$ is the order of diffraction, n_{eff} is the effective refractive index of the propagation mode, and $\Lambda$is the grating period. The linewidth near threshold is measured as 0.20nm, which results in a cavity quality factor (Q) of over 3000.

Figure 8.5-(a) represents the far-filed image of the emission pattern recorded by a CCD camera, and Figure 8.5-(b) shows the far-field radiation patterns of the laser passing through a linear polarizer with different orientation angles. The laser is expected to be azimuthally

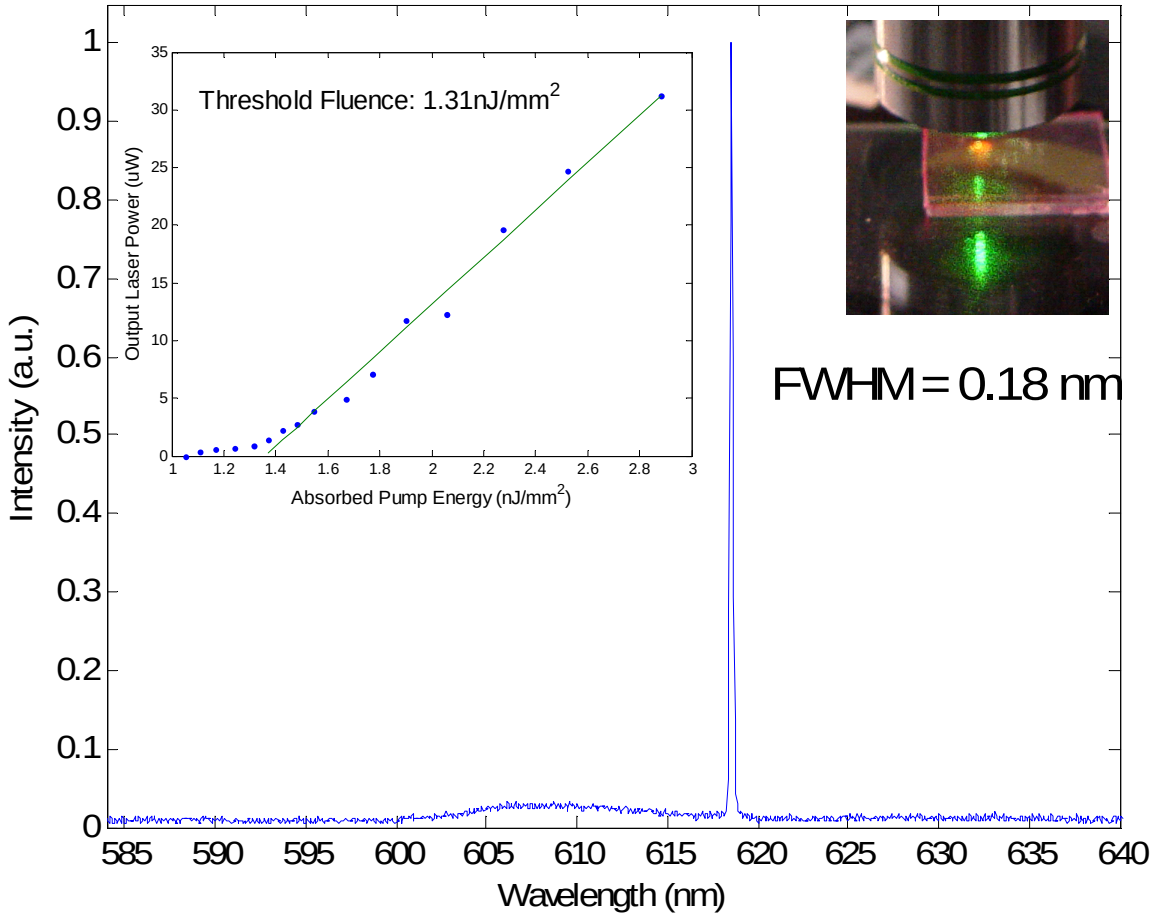

Figure 8.4: Nanoimprinted circular grating DFB dye laser spectrum. The measured linewidth is 0.18nm. Left inset: The output power vs. the absorbed pump energy curve. The threshold fluence is 1.31nJ/mm2. Right inset: Polymer laser chip excited by Nd:YAG 532nm laser pulse.

polarized [131], as illustrated in the polarization patterns. The azimuthal polarization also results in a zero electrical field (a dark spot) at the center of the laser [124]. In the lasing process, many spatial modes can be excited with their mode thresholds very close to each other [132]. The fundamental mode is normally the favored one, because higher order modes do not overlap well with the gain region. The left inset of Figure 8.4 shows the variation of the output laser power as a function of absorbed pump energy. With the absorbed threshold energy of 41.3nJ, the threshold pump fluence is estimated to be 1.31uJ/mm^2. This pump intensity is well within the reach of commercial high power blue laser diodes (LDs), thus enabling the fabrication of a self-contained LD-pumped device. The right inset of Fig-

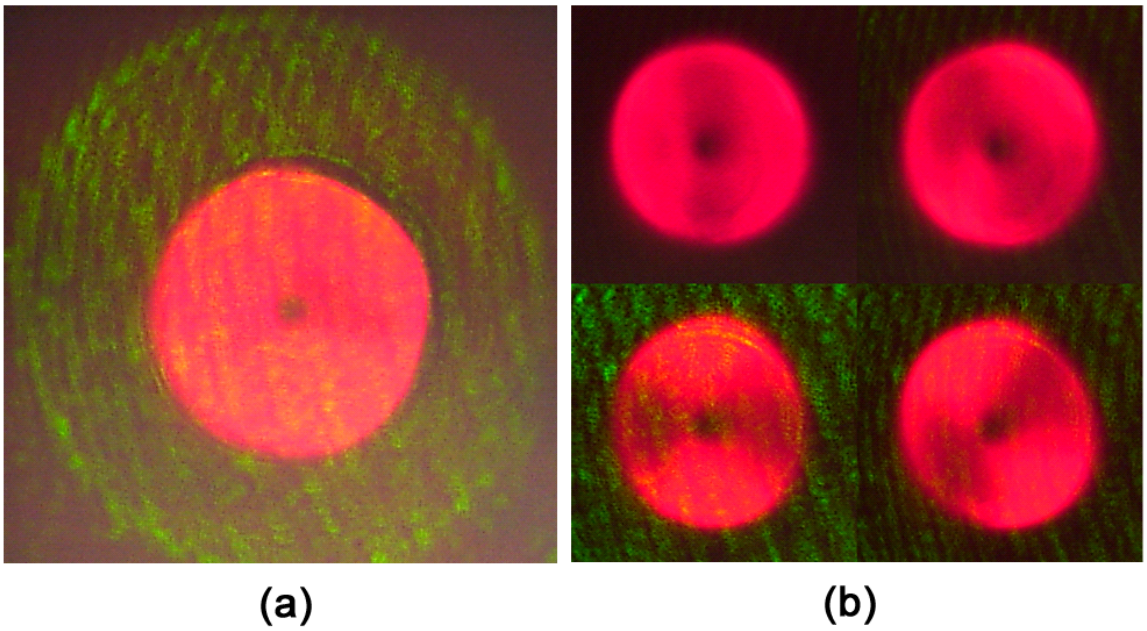

Figure 8.5: (a) Far-field image of the emission pattern recorded by a CCD camera. (b) Circular DFB laser far-field radiation patterns through a linear polarizer with different orientation angles. The laser emits an azimuthally polarized, well-confined circular beam.

ure 8.4 shows that the polymer laser is pumped from the back side and the lasing emission is collected from the surface of the chip. The transparency of the substrate, the size and geometry of the laser cavity and the low threshold match well with the output beams of high power LEDs and LDs. Therefore the replication-molded ring geometry represents a very promising structure for the construction of compact LED or LD pumped portable dye lasers. We observe decreases in the laser emission with increasing exposure time. This result is consistent with previous studies on polymer DFB structures [133]. The lifetime of polymer dye laser can last over 10^6 shots of pump laser pulse, and if the characterization of the device is carried out under vacuum to inhibit photo-oxidation, the lifetime can be further extended [134]. Because of the low cost of materials and fabrication, replication molded devices are disposable and may not require a long lifetime. In the future, we plan to make an optofluidic version using PDMS and replica molding softlithography like the ones demonstrated in the previous chapters, which can allow us to constantly change the dye to increase the device life time and to tune the wavelength.

8.4 Summary

In this chapter, we demonstrate a surface emitting polymer dye laser with a circular grating distributed feedback structure realized by nanoimprint lithography. We achieved excitation thresholds as low as 1.31nJ/mm^2 and FWHM linewidths of 0.18nm. The technique described here enables the fabrication of low cost, high quality and mass producible laser arrays, which may be deployed as compact and inexpensive coherent light sources for lab-on-a-chip applications such as sensing and spectroscopy. Future work will be focused on improving the laser cavity Q values with better electromagnetic design, optimizing the dye concentration, and fabricating smoother surfaces. The ultimate goal is to reduce the lasing threshold to enable the use of pump LEDs as integrated and inexpensive pump sources for on-chip polymer lasers. The circular grating structure can also be implemented on an optofluidic PDMS device using soft lithography.

Chapter 9

Future Directions

Even though some impressive performances, such as single mode operation, narrow linewidth and wide tunability, have been obtained, optofluidic dye laser research is still at its very early stage. In order for this technique to have an impact on the "lab-on-a-chip" systems, we believe the most important next step is to integrate the optical pump source onto the same device. At present, due to the small gain volume, the required pump threshold intensity ($\sim$100kW/cm^2) is within the reach of commercially available high power laser diodes. However, further improvement in pump efficiency can be achieved by introducing resonant structures at the pump wavelength or adapting a dual-core longitudinal pump geometry widely used in fiber lasers [135]. This may eventually lead to high power LED pumped optofluidic dye lasers.

Other more radical on-chip pumping schemes based on effects such as electrochemiluminescence [136] [137] [138] [139] [140] and chemiluminescence [141] are also worth investigation since they can completely eliminate the need for an external optical pump. Indeed, many applications can arise if such schemes can provide high enough optical gain.

One obvious direction for the future studies on optofluidic dye lasers is to follow the historical line of the conventional dye laser development. Compared to the best performances of conventional dye lasers [11], it is clear that optofluidic dye lasers still have a long way to go. Thus far, no continuous wave (CW) operation or ultrashort pulse generation has been demonstrated. These are challenging tasks due to the small fluidic confinement and geometrical limitations in microfluidic devices. It seems the realization of cavity structures compatible with fast liquid flow rate will be a milestone for the future advances along this

line.

In general, the experiences and lessons from the conventional dye laser [11] and semiconductor laser communities [20] provide good guidelines for the future development of optofluidic dye lasers. For example the development of the high speed dye jet enabled stable continuous wave (CW) dye laser operation [142]. A similar device on a microfuidic chip may be needed for CW optofluidic dye lasers. Also we should look at the various Q-switching and mode locking methods used in conventional ultra-short pulse dye lasers and consider their possible implementations on a microfluidic platform. For one, the ring resonator geometry discussed in Chapter 6 is a good candidate for passive mode locking when a suitable saturable absorber dye is mixed with the laser dye or placed at a proper location on the ring.

Another interesting direction is to implement other laser cavity structures beyond the currently demonstrated Fabry-Perot, DFB and microring types onto the microfluidic platform, such as other whispering gallery mode (WGM) resonators including microdisks[143], microtoroids[144] and microspheres[1], circular-grating DFB structures [123], annular Bragg reflector (ABR) cavities [145], and photonic crystal based cavities [146]. In addition to provide novel laser cavity structures, the capability of building such liquid-core optical microcavities has implications in both fundamental study and practical applications. For example such optofluidic microcavities can enable the study of cavity quantum electrodynamics (QED) effects, such as spontaneous emission engineering, thresholdless lasing and single photon generation, in a more controlled and reconfigurable manner which currently is not available through solid state materials [38] [3] [147]. High Q and small volume optofluidic microcavites are also ideal structures for single molecule biological and chemical sensing applications.

In order to show the full potential of optofluidic dye lasers, the demonstration of a complete “lab-on-a-chip” system integrated with an on-chip liquid dye laser is essential. Important examples in this class include fluorescence actuated cell sorters (FACS) [148], fluorescence based automated DNA sequencers [149] and Raman spectrometers. Of course, we believe many other applications and novel devices that never existed before will start to appear due to the powerful optofluidic integration and adaptation[8].

Appendix A

Fabrication Recipes

A.1 Chrome Mask Fabrication

We used DWL 66 direct laser writer (Heidelberg Instruments) to make the high resolution Chrome masks, which were required in the laser cavity mold fabrication. DWL 66 uses a 442nm HeCd laser and can achieve over half a million (500000) dpi (0.5μm feature size) using a 40nm writeable address grid. The writing areas can be as large as 8 by 8 inches. All the patterns were designed using AUTOCAD (AutoDesk) and converted to a LIC format used by DWL. The 3 by 3 inches Chrome photomask blanks were obtained from Nanofilm (www.nanofilm.com). The plates were coated with 5300Å thick AZ1518 positive photoresist. *The calibration of the DWL exposure defocus and energy was essential for obtaining feature sizes below 1.5μm with good quality.*

After the DWL writing, the plate was

1. developed in Microposit MF322 photoresist developer for 1 minutes
2. rinse with DI water and blow dry with N_2 gas
3. etched in CR-7S Cr etch for 50 seconds
4. rinse with DI water and blow dry with N_2 gas
5. cleaned in Nanostrip for 5 minutes
6. rinse with DI water, then IPA and blow dry with N_2 gas.

A.2 Master Mold Fabrication

The photomasks used in this step were either Chrome masks obtained by DWL 66 laser writing for laser cavities, or transparency films by a laser photoplotting service (CAD/Art Services) for microfluidic circuits.

A.2.1 Laser Mold Fabrication

Start with a clean Si wafer.

1. Clean the Si wafer by rinsing in Methanol, IPA, DI water, then bake at 200 degree for 5 minutes
2. Spin coat SU8 2002 (MicroChem) negative photoresist: ramp up to 500rpm at 100rpm/second acceleration, ramp to 3000rpm at 300rpm/second acceleration, and hold for 30 seconds
3. Pre-bake on a hot plate at 65 degree for 2 minutes
4. Soft bake on a hot plate at 95 degree for 5 minutes
5. Slowly cool down the wafer to room temperature
6. Expose the wafer for 15 seconds at 4.5mW/cm^2 (i-line 365nm, exposure energy 60-80mJ/cm^2)
7. Pre-bake on a hot plate at 65 degree for 2 minutes
8. Post-exposure bake (PEB) on a hot plate at 95 degree for 5 minutes
9. Slowly cool down the wafer to room temperature
10. Develope in SU8 nanodeveloper for 1 minutes
11. Rinse with IPA, blow dry with N_2 gas

Then the mold for the liquid input channel was fabricated using SPR220-7 photoresist on the same chip following the steps given in the next section.

For SU8 on glass devices, such as the evanescenct gain dye lasers, slow cooling-down is very crucial during the various soft bake and PEB steps due to the relative poor adhesion between SU8 and glass. Usually, enough slow cooling can be achieved by switching off the hot plate power, and let it cool down naturally. If still not satisfactory, stepped cooling down rate must be empirically determined by manually setting the temperature of the hot plate.

A.2.2 Microfluidic Circuits Mold Fabrication

Obtain two clean Si wafers.

1. Clean the Si wafer by rinsing in Methanol, IPA, DI water, then bake at 200 degree for 5 minutes
2. Treat the wafer with hexamethyldisilazane (HMDS) vapor (Microprime HP-Primer, ShinEtsu MicroSi) for 1 minutes at 1 atmosphere
3. Spin coat SPR2207 positive photoresist: ramp to 2000rpm at 500rpm/second acceleration, and hold for 1 minutes
4. Soft bake on a hot plate at 115 degree for 90 seconds
5. Slowly cool down the wafer to room temperature
6. Expose the wafer for 2.5 minutes at 4.5mW/cm^2 (i-line 365nm, exposure energy 400mJ/cm^2)
7. (optional) Post-exposure bake on a hot plate at 115 degree for 90 seconds
8. Slowly cool down the wafer to room temperature
9. Develope in Microposit MF319 photoresist developer for 2 minutes
10. Rinse with DI water, blow dry with N_2 gas

The molds for the control layer and fluidic layer were fabricated on separate wafers. The laser cavities were also fabricated on the fluidic layer mold. The alignment between the fluidic channels and the laser cavities was done under a mask aligner.

A.3 PDMS Device Fabrication

A.3.1 Two-Layer Devices

Have the master mold ready.

1. Mix 5 parts A:1 parts B PDMS (RTV 615) in the HM501 Hybrid Mixer
2. Treat the mold with trimethylchlorosilane (TMCS) vapor for 5 minutes
3. Pour the PDMS prepolymer onto the mold to ~4mm thick
4. Degas in a vacuum chamber for 30 minutes
5. Bake in a convection oven at 80 degree for 30 minutes
6. Peel the partially cured PDMS from the mold

7. Punch access ports at the inlets by using a 0.055-inch punch (Technical Innovations)

8. Bake the partially cured PDMS in the oven at 80 degree for 2 hours

9. Treat the cured PDMS with Oxygen plasma at 80W for 10 seconds, and bond it to a featureless cured PDMS flat immediately

10. Bake the final device in the oven at 80 degree overnight

The featureless cured PDMS flat can be formed by spinning on or pouring PDMS prepolymer onto a polished Si wafer depending on the thickness needed.

A.3.2 Three-Layer Devices with Push-Up Valves

Have both the fluidic and control layer molds ready.

1. Mix 5 parts A:1 parts B PDMS in the HM501 Hybrid Mixer for the fluidic (laser) layer

2. Treat the fluidic layer mold with TMCS vapor for 5 minutes

3. Pour the 5:1 PDMS prepolymer onto the fluidic layer mold to ~4mm thick

4. Degas the fluidic layer in a vacuum chamber for 30 minutes

5. Bake the fluidic layer in a convection oven at 80 degree for 30 minutes

6. Peel the partially cured PDMS from the fluidic layer mold

7. Bake the partially cured fluidic layer in the oven at 80 degree for 2 hours

8. Mix 20 parts A:1 parts B PDMS in the HM501 Hybrid Mixer for the control layer

9. Treat the control layer mold with TMCS vapor for 5 minutes

10. Spin on the 20:1 PDMS prepolymer onto the control layer mold at 2400rpm (~35μm thick)

11. Bake the control layer in a convection oven at 80 degree for 30 minutes

12. Treat both layers with Oxygen plasma at 80W for 10 seconds, the fluidic layer should have the feature side facing up 13. Align the fluidic layer onto the control layer under a steroscope or a mask aligner

14. Bake the two-layer structure in the oven at 80 degree for 30 minutes

15. Peel the two-layer structure from the control layer mold

16. Punch access ports at the inlets by using a 0.055-inch punch (Technical Innovations)

17. Treat the two-layer structure with Oxygen plasma at 80W for 10 seconds, and bond it

to a featureless cured PDMS flat immediately

18. Bake the final three-layer structure in the oven at 80 degree overnight

Bibliography

[1] S. X. Qian, J. B. Snow, H. M. Tzeng, and R. K. Chang. Lasing droplets - highlighting the liquid-air interface by laser-emission. *Science*, 231(4737):486–488, 1986.

[2] H. J. Moon, Y. T. Chough, and K. An. Cylindrical microcavity laser based on the evanescent-wave-coupled gain. *Physical Review Letters*, 85(15):3161–3164, 2000.

[3] H. Yokoyama. Physics and device applications of optical microcavities. *Science*, 256(5053):66–70, 1992.

[4] Y. N. Xia and G. M. Whitesides. Soft lithography. *Annual Review of Materials Science*, 28:153–184, 1998.

[5] M. A. Unger, H. P. Chou, T. Thorsen, A. Scherer, and S. R. Quake. Monolithic microfabricated valves and pumps by multilayer soft lithography. *Science*, 288(5463):113–116, 2000.

[6] T. Thorsen, S. J. Maerkl, and S. R. Quake. Microfluidic large-scale integration. *Science*, 298(5593):580–584, 2002.

[7] J. W. Hong and S. R. Quake. Integrated nanoliter systems. *Nature Biotechnology*, 21(10):1179–1183, 2003.

[8] D. Psaltis, S. R. Quake, and C. H. Yang. Developing optofluidic technology through the fusion of microfluidics and optics. *Nature*, 442(7101):381–386, 2006.

[9] Z. Y. Li, Z. Y. Zhang, A. Scherer, and D. Psaltis. Mechanically tunable optofluidic distributed feedback dye laser. *Optics Express*, 14(22):10494–10499, 2006.

[10] D. Erickson and D. Q. Li. Integrated microfluidic devices. *Analytica Chimica Acta*, 507(1):11–26, 2004.

[11] F. P. Schafer. *Dye lasers*. Topics in applied physics. Springer-Verlag, Berlin ; New York, 3rd enl. and rev. edition, 1990.

[12] P. P. Sorokin. Flashlamp-pumped organic dye lasers. *IEEE Journal of Quantum Electronics*, 4(5):315–, 1968.

[13] P. P. Sorokin, J. R. Lankard, V. L. Moruzzi, and E. C. Hammond. Flashlamp-pumped organic-dye lasers. *Journal of Chemical Physics*, 48(10):4726–, 1968.

[14] B. B. Snavely. Flashlamp-excited organic dye lasers. *Proceedings of the IEEE*, 57(8):1374–, 1969.

[15] C. V. Shank. Physics of dye lasers. *Reviews of Modern Physics*, 47(3):649–657, 1975.

[16] O. G. Peterson. *Dye lasers, in Quantum electronics, part A, Tang, C. L. eds.* Methods of experimental physics. Academic Press, New York.

[17] T. F. Jr Johnston. *Tunable dye lasers, in Encyclopedia of physical science and technology, Meyers, Robert A. eds*. Academic Press, Orlando, 1987.

[18] F. J. Duarte and Lloyd William Hillman. *Dye laser principles, with applications*. Quantum electronics-principles and applications. Academic Press, Boston, 1990.

[19] F. J. Duarte. *Selected papers on dye lasers*. SPIE milestone series. SPIE Optical Engineering Press, Bellingham, Wash., USA, 1992.

[20] L. A. Coldren and S. W. Corzine. *Diode lasers and photonic integrated circuits*. Wiley series in microwave and optical engineering. Wiley, New York, 1995.

[21] Robert G. Hunsperger. *Integrated optics : theory and technology*. Advanced texts in physics,. Springer, Berlin ; New York, 5th edition, 2002.

[22] Theodor Tamir. *Guided-wave optoelectronics*. Springer series in electronics and photonics. Springer-Verlag, Berlin ; New York, 2nd edition, 1990.

[23] O. G. Peterson, J. P. Webb, W. C. Mccolgin, and J. H. Eberly. Organic dye laser threshold. *Journal of Applied Physics*, 42(5):1917–, 1971.

[24] Orazio Svelto and D. C. Hanna. *Principles of lasers*. Plenum Press, New York, 4th edition, 1998.

[25] Christopher C. Davis. *Lasers and electro-optics : fundamentals and engineering*. Cambridge University Press, Cambridge [England] ; New York, NY, USA, 1996.

[26] William Thomas Silfvast. *Laser fundamentals*. Cambridge University Press, Cambridge ; New York, 2nd edition, 2004.

[27] G. M. Whitesides. The origins and the future of microfluidics. *Nature*, 442(7101):368–373, 2006.

[28] M. L. Chabinyc, D. T. Chiu, J. C. McDonald, A. D. Stroock, J. F. Christian, A. M. Karger, and G. M. Whitesides. An integrated fluorescence detection system in poly(dimethylsiloxane) for microfluidic applications. *Analytical Chemistry*, 73(18):4491–4498, 2001.

[29] E. Verpoorte. Chip vision - optics for microchips. *Lab on a Chip*, 3(3):42n–52n, 2003.

[30] International Human Genome Sequencing Consortium. Initial sequencing and analysis of the human genome. *Nature*, 409(6822):860–921, 2001.

[31] J. C. Venter et al. The sequence of the human genome. *Science*, 291(5507):1304–1351, 2001.

[32] R. G. Blazej, P. Kumaresan, and R. A. Mathies. Microfabricated bioprocessor for integrated nanoliter-scale sanger dna sequencing. *Proceedings of the National Academy of Sciences of the United States of America*, 103(19):7240–7245, 2006.

[33] B. M. Paegel, C. A. Emrich, G. J. Weyemayer, J. R. Scherer, and R. A. Mathies. High throughput DNA sequencing with a microfabricated 96-lane capillary array electrophoresis bioprocessor. *Proceedings of the National Academy of Sciences of the United States of America*, 99(2):574–579, 2002.

[34] C. Monat, P. Domachuk, and B. J. Eggleton. Integrated optofluidics: A new river of light. *Nature Photonics*, 1(2):106–114, 2007.

[35] H. M. Tzeng, K. F. Wall, M. B. Long, and R. K. Chang. Evaporation and condensation rates of liquid droplets deduced from structure resonances in the fluorescence-spectra. *Optics Letters*, 9(7):273–275, 1984.

[36] E. P. Ippen, C. V. Shank, and A. Dienes. Rapid photobleaching of organic laser dyes in continuously operated devices. *IEEE Journal of Quantum Electronics*, Qe 7(4):178–, 1971.

[37] G. Pendock, H. S. Mackenzie, and F. P. Payne. Tapered optical fiber dye-laser. *Electronics Letters*, 28(2):149–150, 1992.

[38] Richard K. Chang and Anthony J. Campillo. *Optical processes in microcavities*. World Scientific, Singapore ; New Jersey, 1996.

[39] K. J. Vahala. Optical microcavities. *Nature*, 424(6950):839–846, 2003.

[40] T. W. Hansen. Edible lasers and other delights of the 1970s. *Optics and Photonics News*, 16(2):14–16, 2005.

[41] M. Tona and M. Kimura. Novel lasing modes observed in a levitated single dye-doped microdroplet. *Journal of the Physical Society of Japan*, 69(11):3533–3535, 2000.

[42] H. Azzouz, L. Alkhafadiji, S. Balslev, J. Johansson, N. A. Mortensen, S. Nilsson, and A. Kristensen. Levitated droplet dye laser. *Optics Express*, 14(10):4374–4379, 2006.

[43] H. B. Lin, J. D. Eversole, and A. J. Campillo. Vibrating orifice droplet generator for precision optical studies. *Review of Scientific Instruments*, 61(3):1018–1023, 1990.

[44] J. D. Eversole, H. B. Lin, A. L. Huston, A. J. Campillo, P. T. Leung, S. Y. Liu, and K. Young. High-precision identification of morphology-dependent resonances in optical processes in microdroplets. *Journal of the Optical Society of America B-Optical Physics*, 10(10):1955–1968, 1993.

[45] H. B. Lin, A. L. Huston, B. L. Justus, and A. J. Campillo. Some characteristics of a droplet whispering-gallery-mode laser. *Optics Letters*, 11(10):614–616, 1986.

[46] H. B. Lin, A. L. Huston, J. D. Eversole, B. L. Justus, and A. J. Campillo. Some characteristics of a droplet whispering gallery mode laser. *Journal of the Optical Society of America B-Optical Physics*, 3(8):P250–251, 1986.

[47] H. B. Lin, J. D. Eversole, and A. J. Campillo. Spectral properties of lasing microdroplets. *Journal of the Optical Society of America B-Optical Physics*, 9(1):43–50, 1992.

[48] A. J. Campillo, J. D. Eversole, and H. B. Lin. Cavity quantum electrodynamic enhancement of stimulated-emission in microdroplets. *Physical Review Letters*, 67(4):437–440, 1991.

[49] H. B. Lin, J. D. Eversole, C. D. Merritt, and A. J. Campillo. Cavity-modified spontaneous-emission rates in liquid microdroplets. *Physical Review A*, 45(9):6756–6760, 1992.

[50] M. D. Barnes, W. B. Whitten, S. Arnold, and J. M. Ramsey. Homogeneous linewidths of Rhodamine-6G at room-remperature from cavity-enhanced spontaneous emission rates. *Journal of Chemical Physics*, 97(10):7842–7845, 1992.

[51] M. D. Barnes, K. C. Ng, W. B. Whitten, and J. M. Ramsey. Detection of single Rhodamine-6G molecules in levitated microdroplets. *Analytical Chemistry*, 65(17):2360–2365, 1993.

[52] M. D. Barnes, C. Y. Kung, W. B. Whitten, J. M. Ramsey, S. Arnold, and S. Holler. Fluorescence of oriented molecules in a microcavity. *Physical Review Letters*, 76(21):3931–3934, 1996.

[53] N. Lermer, M. D. Barnes, C. Y. Kung, W. B. Whitten, and J. M. Ramsey. High efficiency molecular counting in solution: Single-molecule detection in electrodynamically focused microdroplet streams. *Analytical Chemistry*, 69(11):2115–2121, 1997.

[54] T. Thorsen, R. W. Roberts, F. H. Arnold, and S. R. Quake. Dynamic pattern formation in a vesicle-generating microfluidic device. *Physical Review Letters*, 86(18):4163–4166, 2001.

[55] S. L. Anna, N. Bontoux, and H. A. Stone. Formation of dispersions using "flow focusing" in microchannels. *Applied Physics Letters*, 82(3):364–366, 2003.

[56] A. Mekis, J. U. Nockel, G. Chen, A. D. Stone, and R. K. Chang. Ray chaos and Q spoiling in lasing droplets. *Physical Review Letters*, 75(14):2682–2685, 1995.

[57] J. U. Nockel, A. D. Stone, G. Chen, H. L. Grossman, and R. K. Chang. Directional emission from asymmetric resonant cavities. *Optics Letters*, 21(19):1609–1611, 1996.

[58] Z. Y. Li and D. Psaltis. Optofluidic distributed feedback dye lasers. *IEEE Journal of Selected Topics in Quantum Electronics*, 13(2):185–193, 2007.

[59] A. E. Vasdekis, G. Tsiminis, J. C. Ribierre, L. O'Faolain, T. F. Krauss, G. A. Turnbull, and I. D. W. Samuel. Diode pumped distributed bragg reflector lasers based on a dye-to-polymer energy transfer blend. *Optics Express*, 14(20):9211–9216, 2006.

[60] H. Fujiwara and K. Sasaki. Lasing of a microsphere in dye solution. *Japanese Journal of Applied Physics Part 1*, 38(9A):5101–5104, 1999.

[61] Y. S. Choi, H. J. Moon, K. Y. An, S. B. Lee, J. H. Lee, and J. S. Chang. Ultrahigh-Q microsphere dye laser based on evanescent-wave coupling. *Journal of the Korean Physical Society*, 39(5):928–931, 2001.

[62] K. An and H. J. Moon. Laser oscillations with pumping-independent ultrahigh cavity quality factors in evanescent-wave-coupled-gain microsphere dye lasers. *Journal of the Physical Society of Japan*, 72(4):773–776, 2003.

[63] M. Kazes, D. Y. Lewis, Y. Ebenstein, T. Mokari, and U. Banin. Lasing from semiconductor quantum rods in a cylindrical microcavity. *Advanced Materials*, 14(4):317–, 2002.

[64] H. J. Moon, Y. T. Chough, J. B. Kim, K. W. An, J. H. Yi, and J. Lee. Cavity-Q-driven spectral shift in a cylindrical whispering-gallery-mode microcavity laser. *Applied Physics Letters*, 76(25):3679–3681, 2000.

[65] J. Yang and L. J. Guo. Optical sensors based on active microcavities. *IEEE Journal of Selected Topics in Quantum Electronics*, 12(1):143–147, 2006.

[66] F. Demartini and G. R. Jacobovitz. Anomalous spontaneous stimulated-decay phase-transition and zero-threshold laser action in a microscopic cavity. *Physical Review Letters*, 60(17):1711–1714, 1988.

[67] M. Suzuki, H. Yokoyama, S. D. Brorson, and E. P. Ippen. Observation of spontaneous emission lifetime change of dye-containing langmuir-blodgett-films in optical microcavities. *Applied Physics Letters*, 58(10):998–1000, 1991.

[68] H. Yokoyama, M. Suzuki, and Y. Nambu. Spontaneous emission and laser oscillation properties of microcavities containing a dye solution. *Applied Physics Letters*, 58(23):2598–2600, 1991.

[69] H. Yokoyama and S. D. Brorson. Rate-equation analysis of microcavity lasers. *Journal of Applied Physics*, 66(10):4801–4805, 1989.

[70] E. P. Ippen and C. V. Shank. Evanescent field-pumped dye laser. *Applied Physics Letters*, 21(7):301–303, 1972.

[71] G. Zeidler. Optical waveguide technique with organic dye lasers. *Journal of Applied Physics*, 42(2):884–886, 1971.

[72] P. Russell. Photonic crystal fibers. *Science*, 299(5605):358–362, 2003.

[73] A. E. Vasdekis, G. E. Town, G. A. Turnbull, and I. D. W. Samuel. Fluidic fibre dye lasers. *Optics Express*, 15(7):3962–3967, 2007.

[74] G. J. Pendock, H. S. Mackenzie, and F. P. Payne. Dye-lasers using tapered optical fibers. *Applied Optics*, 32(27):5236–5242, 1993.

[75] N. Periasamy and Z. Bor. Distributed feedback laser action in an optical fiber by evanescent field coupling. *Optics Communications*, 39(5):298–302, 1981.

[76] N. Periasamy and F. P. Schafer. Laser amplification in an optical fiber by evanescent field coupling. *Applied Physics*, 24(3):201–203, 1981.

[77] D. V. Vezenov, B. T. Mayers, R. S. Conroy, G. M. Whitesides, P. T. Snee, Y. Chan, D. G. Nocera, and M. G. Bawendi. A low-threshold, high-efficiency microfluidic waveguide laser. *Journal of the American Chemical Society*, 127(25):8952–8953, 2005.

[78] Z. Y. Li, Z. Y. Zhang, T. Emery, A. Scherer, and D. Psaltis. Single mode optofluidic distributed feedback dye laser. *Optics Express*, 14(2):696–701, 2006.

[79] B. Helbo, A. Kristensen, and A. Menon. A micro-cavity fluidic dye laser. *Journal of Micromechanics and Microengineering*, 13(2):307–311, 2003.

[80] D. B. Wolfe, R. S. Conroy, P. Garstecki, B. T. Mayers, M. A. Fischbach, K. E. Paul, M. Prentiss, and G. M. Whitesides. Dynamic control of liquid-core/liquid-cladding optical waveguides. *Proceedings of the National Academy of Sciences of the United States of America*, 101(34):12434–12438, 2004.

[81] Y. Cheng, K. Sugioka, and K. Midorikawa. Microfluidic laser embedded in glass by three-dimensional femtosecond laser microprocessing. *Optics Letters*, 29(17):2007–2009, 2004.

[82] S. Balslev and A. Kristensen. Microfluidic single-mode laser using high-order bragg grating and antiguiding segments. *Optics Express*, 13(1):344–351, 2005.

[83] Kutter JP Kristensen A Bilenberg B, Helbo B. Tunable microfluidic dye laser. *Proc 12th Int Conf on Solid-State Sensors, Actuators and Microsystems, Transducers*, pages 206–209, 2003.

[84] J. C. Galas, J. Torres, M. Belotti, Q. Kou, and Y. Chen. Microfluidic tunable dye laser with integrated mixer and ring resonator. *Applied Physics Letters*, 86(26):264101, 2005.

[85] M. Gersborg-Hansen and A. Kristensen. Tunability of optofluidic distributed feedback dye lasers. *Optics Express*, 15(1):137–142, 2007.

[86] Q. Kou, I. Yesilyurt, and Y. Chen. Collinear dual-color laser emission from a microfluidic dye laser. *Applied Physics Letters*, 88(9):–, 2006.

[87] J. C. Galas, C. Peroz, Q. Kou, and Y. Chen. Microfluidic dye laser intracavity absorption. *Applied Physics Letters*, 89(22):224101, 2006.

[88] S. Balslev, A. M. Jorgensen, B. Bilenberg, K. B. Mogensen, D. Snakenborg, O. Geschke, J. P. Kutter, and A. Kristensen. Lab-on-a-chip with integrated optical transducers. *Lab on a Chip*, 6(2):213–217, 2006.

[89] M. Nakamura, A. Yariv, H. W. Yen, S. Somekh, and H. L. Garvin. Optically pumped GaAs surface laser with corrugation feedback. *Applied Physics Letters*, 22(10):515–516, 1973.

[90] H. Kogelnik and C. V. Shank. Stimulated emission in a periodic structure. *Applied Physics Letters*, 18(4):152–, 1971.

[91] H. Kogelnik and C. V. Shank. Coupled-wave theory of distributed feedback lasers. *Journal of Applied Physics*, 43(5):2327–2335, 1972.

[92] Amnon Yariv and Pochi Yeh. *Photonics : optical electronics in modern communications*. The Oxford series in electrical and computer engineering. Oxford University Press, New York, 6th edition, 2007.

[93] L. A. Wellerbrophy and D. G. Hall. Analysis of wave-guide gratings - application of rouard method. *Journal of the Optical Society of America a-Optics Image Science and Vision*, 2(6):863–871, 1985.

[94] Pochi Yeh. *Optical waves in layered media*. Wiley series in pure and applied optics. Wiley, New York, 1988.

[95] Kerry Vahala. *Optical microcavities*. Advanced series in applied physics. World Scientific, Singapore ; Hackensack, N.J., 2004.

[96] W. Streifer, D. R. Scifres, and R. D. Burnham. Coupling coefficients for distributed feedback single-heterostructure and double-heterostructure diode lasers. *IEEE Journal of Quantum Electronics*, 11(11):867–873, 1975.

[97] D. R. Scifres, R. D. Burnham, and W. Streifer. Highly collimated laser-beams from electrically pumped SH GaAs-GaAlAs distributed-feedback lasers. *Applied Physics Letters*, 26(2):48–50, 1975.

[98] J. C. McDonald, D. C. Duffy, J. R. Anderson, D. T. Chiu, H. K. Wu, O. J. A. Schueller, and G. M. Whitesides. Fabrication of microfluidic systems in poly(dimethylsiloxane). *Electrophoresis*, 21(1):27–40, 2000.

[99] S. R. Quake and A. Scherer. From micro- to nanofabrication with soft materials. *Science*, 290(5496):1536–1540, 2000.

[100] J. C. McDonald and G. M. Whitesides. Poly(dimethylsiloxane) as a material for fabricating microfluidic devices. *Accounts of Chemical Research*, 35(7):491–499, 2002.

[101] J. N. Lee, C. Park, and G. M. Whitesides. Solvent compatibility of poly(dimethylsiloxane)-based microfluidic devices. *Analytical Chemistry*, 75(23):6544–6554, 2003.

[102] S. C. De Rosa, L. A. Herzenberg, L. A. Herzenberg, and M. Roederer. 11-color, 13-parameter flow cytometry: identification of human naive T cells by phenotype, function, and T-cell receptor diversity. *Nature Medicine*, 7(2):245–248, 2001.

[103] C. L. Hansen, M. O. A. Sommer, and S. R. Quake. Systematic investigation of protein phase behavior with a microfluidic formulator. *Proceedings of the National Academy of Sciences of the United States of America*, 101(40):14431–14436, 2004.

[104] C. V. Shank, Bjorkhol.Je, and H. Kogelnik. Tunable distributed-feedback dye laser. *Applied Physics Letters*, 18(9):395–, 1971.

[105] J. L. Wilbur, R. J. Jackman, G. M. Whitesides, E. L. Cheung, L. K. Lee, and M. G. Prentiss. Elastomeric optics. *Chemistry of Materials*, 8(7):1380–1385, 1996.

[106] *RTV 615 Data Sheet*. GE Advanced Materials Silicones, Wilton; CT, 1998.

[107] http://www.exciton.com.

[108] Y. Oki, S. Miyamoto, M. Maeda, and N. J. Vasa. Multiwavelength distributed-feedback dye laser array and its application to spectroscopy. *Optics Letters*, 27(14):1220–1222, 2002.

[109] V. Studer, G. Hang, A. Pandolfi, M. Ortiz, W. F. Anderson, and S. R. Quake. Scaling properties of a low-actuation pressure microfluidic valve. *Journal of Applied Physics*, 95(1):393–398, 2004.

[110] V. Jayaraman, Z. M. Chuang, and L. A. Coldren. Theory, design, and performance of extended tuning range semiconductor-lasers with sampled gratings. *IEEE Journal of Quantum Electronics*, 29(6):1824–1834, 1993.

[111] A. Yariv, Y. Xu, R. K. Lee, and A. Scherer. Coupled-resonator optical waveguide: a proposal and analysis. *Optics Letters*, 24(11):711–713, 1999.

[112] J. E. Heebner, P. Chak, S. Pereira, J. E. Sipe, and R. W. Boyd. Distributed and localized feedback in microresonator sequences for linear and nonlinear optics. *Journal of the Optical Society of America B-Optical Physics*, 21(10):1818–1832, 2004.

[113] Y. M. Landobasa and M. K. Chin. Defect modes in micro-ring resonator arrays. *Optics Express*, 13(20):7800–7815, 2005.

[114] B. B. Snavely and F. P. Schafer. Feasibility of CW operation of dye - lasers. *Physics Letters A*, A 28(11):728–, 1969.

[115] O. G. Peterson, S. A. Tuccio, and B. B. Snavely. CW operation of an organic dye solution laser. *Applied Physics Letters*, 17(6):245–. H5271 Year = 1970.

[116] Y. Oki, K. Aso, D. Zuo, N. J. Vasa, and M. Maeda. Wide-wavelength-range operation of a distributed-feedback dye laser with a plastic waveguide. *Japanese Journal of Applied Physics Part 1*, 41(11A):6370–6374, 2002.

[117] Y. Oki, T. Yoshiura, Y. Chisaki, and M. Maeda. Fabrication of a distributed-feedback dye laser with a grating structure in its plastic waveguide. *Applied Optics*, 41(24):5030–5035, 2002.

[118] C. Bauer, H. Giessen, B. Schnabel, E. B. Kley, C. Schmitt, U. Scherf, and R. F. Mahrt. A surface-emitting circular grating polymer laser. *Advanced Materials*, 13(15):1161–, 2001.

[119] G. A. Turnbull, A. Carleton, G. F. Barlow, A. Tahraouhi, T. F. Krauss, K. A. Shore, and I. D. W. Samuel. Influence of grating characteristics on the operation of circular-grating distributed-feedback polymer lasers. *Journal of Applied Physics*, 98(2):023105, 2005.

[120] J. R. Lawrence, P. Andrew, W. L. Barnes, M. Buck, G. A. Turnbull, and I. D. W. Samuel. Optical properties of a light-emitting polymer directly patterned by soft lithography. *Applied Physics Letters*, 81(11):1955–1957, 2002.

[121] D. Pisignano, L. Persano, P. Visconti, R. Cingolani, G. Gigli, G. Barbarella, and L. Favaretto. Oligomer-based organic distributed feedback lasers by room-temperature nanoimprint lithography. *Applied Physics Letters*, 83(13):2545–2547, 2003.

[122] D. Pisignano, L. Persano, G. Gigli, P. Visconti, T. Stomeo, M. De Vittorio, G. Barbarella, L. Favaretto, and R. Cingolani. Planar organic photonic crystals fabricated by soft lithography. *Nanotechnology*, 15(7):766–770, 2004.

[123] Erdogan T. and Hall D. G. Circularly symmetric distributed feedback semiconductor laser: An analysis. *Journal of Applied Physics*, 68(4):1435–1444, 1990.

[124] T. Erdogan and D. G. Hall. "circularly symmetrical distributed feedback laser - coupled mode treatment of TE vector-fields". *Ieee Journal of Quantum Electronics*, 28(3):612–623, 1992.

[125] P. L. Greene and D. G. Hall. Effects of radiation on circular-grating DFB lasers - part I: coupled-mode equations". *Ieee Journal of Quantum Electronics*, 37(3):353–364, 2001.

[126] P. L. Greene and D. G. Hall. Effects of radiation on circular-grating DFB lasers - part II: device and pump-beam parameters. *Ieee Journal of Quantum Electronics*, 37(3):365–371, 2001.

[127] G. F. Barlow, A. Shore, G. A. Turnbull, and I. D. W. Samuel. Design and analysis of a low-threshold polymer circular-grating distributed-feedback laser. *Journal of the Optical Society of America B-Optical Physics*, 21(12):2142–2150, 2004.

[128] A. Jebali, R. F. Mahrt, N. Moll, D. Erni, C. Bauer, G. L. Bona, and W. Bachtold. Lasing in organic circular grating structures. *Journal of Applied Physics*, 96(6):3043–3049, 2004.

[129] S. Y. Chou, P. R. Krauss, and P. J. Renstrom. Imprint of sub-25 nm vias and trenches in polymers. *Applied Physics Letters*, 67(21):3114–3116, 1995.

[130] S. Y. Chou, P. R. Krauss, and P. J. Renstrom. Nanoimprint lithography. *Journal of Vacuum Science and Technology B*, 14(6):4129–4133, 1996.

[131] R. H. Jordan, D. G. Hall, O. King, G. Wicks, and S. Rishton. Lasing behavior of circular grating surface-emitting semiconductor lasers. *Journal of the Optical Society of America B-Optical Physics*, 14(2):449–453, 1997.

[132] T. Erdogan, O. King, G. W. Wicks, D. G. Hall, E. H. Anderson, and M. J. Rooks. Circularly symmetrical operation of a concentric-circle-grating, surface-emitting, AlGaAs/GaAs quantum-well semiconductor-laser. *Applied Physics Letters*, 60(16):1921–1923, 1992.

[133] G. Heliotis, R. Xia, D. D. C. Bradley, G. A. Turnbull, I. D. W. Samuel, P. Andrew, and W. L. Barnes. Two-dimensional distributed feedback lasers using a broadband, red polyfluorene gain medium. *Journal of Applied Physics*, 96(12):6959–6965, 2004.

[134] P. Del Carro, A. Camposeo, R. Stabile, E. Mele, L. Persano, R. Cingolani, and D. Pisignano. Near-infrared imprinted distributed feedback lasers. *Applied Physics Letters*, 89(20):201105, 2006.

[135] H. Po, J. D. Cao, B. M. Laliberte, R. A. Minns, R. F. Robinson, B. H. Rockney, R. R. Tricca, and Y. H. Zhang. High-power neodymium-doped single transverse-mode fiber laser. *Electronics Letters*, 29(17):1500–1501, 1993.

[136] R. M. Measures. Prospects for developing a laser based on electrochemiluminescence. *Applied Optics*, 13(5):1121–1133, 1974.

[137] R. M. Measures. Physical constraints associated with development of a laser based on electrochemiluminescence. *Applied Optics*, 14(4):909–916, 1975.

[138] C. P. Keszthelyi. Laser based on electrochemiluminescence. *Applied Optics*, 14(7):1710–1712, 1975.

[139] C. A. Heller and J. L. Jernigan. Electrochemical pumping of laser-dyes. *Applied Optics*, 16(1):61–66, 1977.

[140] T. Horiuchi, O. Niwa, and N. Hatakenaka. Evidence for laser action driven by electrochemiluminscence. *Nature*, 394(6694):659–661, 1998.

[141] S. S. Chang, N. B. Rex, and R. K. Chang. Chemical lasing in pendant droplets: lasing-spectra, emission-pattern, and cavity-lifetime measurements. *Journal of the Optical Society of America B-Optical Physics*, 16(8):1224–1235, 1999.

[142] P. K. Runge and Rosenber.R. Unconfined flowing-dye films for CW dye lasers. *IEEE Journal of Quantum Electronics*, Qe 8(12):910–, 1972.

[143] S. L. Mccall, A. F. J. Levi, R. E. Slusher, S. J. Pearton, and R. A. Logan. Whispering-gallery mode microdisk lasers. *Applied Physics Letters*, 60(3):289–291, 1992.

[144] D. K. Armani, T. J. Kippenberg, S. M. Spillane, and K. J. Vahala. Ultra-high-Q toroid microcavity on a chip. *Nature*, 421(6926):925–928, 2003.

[145] J. Scheuer, W. M. J. Green, G. A. DeRose, and A. Yariv. Ingaasp annular bragg lasers: Theory, applications, and modal properties. *IEEE Journal of Selected Topics in Quantum Electronics*, 11(2):476–484, 2005.

[146] O. Painter, R. K. Lee, A. Scherer, A. Yariv, J. D. O'Brien, P. D. Dapkus, and I. Kim. Two-dimensional photonic band-gap defect mode laser. *Science*, 284(5421):1819–1821, 1999.

[147] Y. Yamamoto and R. E. Slusher. Optical processes in microcavities. *Physics Today*, 46(6):66–73, 1993.

[148] A. Y. Fu, H. P. Chou, C. Spence, F. H. Arnold, and S. R. Quake. An integrated microfabricated cell sorter. *Analytical Chemistry*, 74(11):2451–2457, 2002.

[149] L. M. Smith, J. Z. Sanders, R. J. Kaiser, P. Hughes, C. Dodd, C. R. Connell, C. Heiner, S. B. H. Kent, and L. E. Hood. Fluorescence detection in automated DNA-sequence analysis. *Nature*, 321(6071):674–679, 1986.